DEVELOPING GEOCHEMICAL EVIDENCE FOR HOLOCENE HYDROCLIMATE VARIABILITY IN THE SUBTROPICAL WESTERN NORTH ATLANTIC

A Dissertation

by

ANNE E. TAMALAVAGE

Submitted to the Graduate and Professional School of
Texas A&M University
in partial fulfillment of the requirements for the degree of

DOCTOR OF PHILOSOPHY

Chair of Committee,	Peter van Hengstum
Co-Chair of Committee,	Patrick Louchouarn
Committee Members,	Sarah Feakins
	Karl Kaiser
Head of Department,	Shari Yvon Lewis

August 2021

Major Subject: Oceanography

ABSTRACT

Caribbean hydroclimate is regulated by large scale ocean-atmospheric factors (e.g., the North Atlantic Subtropical High - NASH), and increased aridity is predicted into the 21st century. Understanding past changes in precipitation can inform future variability and fill in gaps created by temporal limitations of the satellite record, and uncertainty in the scaling of global climate models in the region. Well-preserved sedimentary records in coastal sinkholes and blue holes across the Caribbean archive proxies that can reconstruct precipitation and environmental variability on Holocene timescales. This dissertation comprises two past hydroclimate records, and one modern sinkhole biogeochemistry study from Great Abaco Island, The Bahamas. The first study uses leaf waxes to reconstruct the isotopic composition of rainfall (δ^2H) over the last 3000 years, finding more enriched values from ~3000 to 2100 cal yrs BP and ~1700 to 1000 cal yrs BP that could be associated with drier conditions and an expanded NASH. However, within the last ~1000 cal yr BP, the isotopic signatures were influenced by inputs from the adjacent mangrove. The next study presents a record of sea level position, limnology, and hydroclimate variability from ~8300 to 1300 cal yr BP. Sedimentological and leaf wax proxies provide evidence for i) a basal peat deposit as a sea level maximum, ii) consistent accumulation of lacustrine marl within the basin from ~8300 to 1700 cal yr BP, and iii) a wetter mid-Holocene from reconstructed δ^2H. The last study explores geochemical signatures of particulate organic matter (POM) in the water column of two stratified coastal sinkholes. The findings provide evidence for biogeochemical processes

occurring along physicochemical gradients, which impact POM and the subsequent archived organic matter. The best proxy target candidates for paleo reconstructions include algal-derived biomarker signals produced within the sinkhole that could reflect regional-scale hydroclimate variability.

DEDICATION

I dedicate this dissertation to my parents, Rita M. Tamalavage and the late John J. Tamalavage, without whom none of this could be possible. Thank you for wiping my tears, smiling back, researching opportunity, and providing financial and emotional support. No words could fully describe my gratitude to you both. May the joy of learning science, and discovering the Earth continue in our family for generations to come.

ACKNOWLEDGEMENTS

There are so many people who have contributed invaluably to the completion of this dissertation. Firstly, I would like to acknowledge my colleague, friend, and husband, Andrew McGuffin (M.S., Oceanography, TAMU ’17), who continues to support, inspire, and motivate me to achieve and follow through on my ambitions. I would also like to thank my family and friends near and far who have been there as strong pillars lifting me as long as I can remember.

I would like to thank my committee members. Dr. Pete van Hengstum, your tenacity and love for sinkholes has inspired me to always keep working and wondering on the quest for great science. Dr. Patrick Louchouarn, your ability to balance deep scientific thought with your commitment in creating a diverse and equitable higher education community is unmatched and has been monumental in building my professional path. Dr. Karl Kaiser, your accessibility and analytical abilities have taught me so much about fixing instruments, pouring a perfect espresso, managing a productive lab, and being a great colleague. Dr. Sarah Feakins, your contributions to the paleo community are legendary, and your continued service to the pursuit of innovative, academic science has taught me how to be a careful, motivated, and thoughtful researcher.

I would like to thank faculty and staff at within the Texas A&M College of Geosciences, and Department of Oceanography for their financial and analytical support, plus the professional networking opportunities. I would specifically like to thank the

Texas A&M University at Galveston Research and Graduate Studies Office (RGSO) for their continued commitment to graduate students, especially during the Global Pandemic (even those displaced College Station in Galveston students). Your support and recognition of our professional status as students will never be forgotten. To the staff filling all of the roles at Texas A&M Galveston, from the counseling center, library, recreation center, facilities services, thank you for providing logistics support throughout my entire career, making it possible to succeed. I would also like to thank the faculty and staff of the Department of Earth Sciences at the University of Southern California, for their hospitality and full support and usage of facilities during my time as a visiting scholar, I truly felt like part of the department.

I am so grateful to my van Hengstum and Louchouarn lab mates, especially those within my PhD cohort: Shawna Little, Richard Sullivan, Tyler Winkler, Dr. Jacque Emmert, Dr. Allison Myers-Pigg, and Dr. Matt Norwood. I truly believe that few are as lucky as I am to have such incredible humans and scientists as colleagues. Thank you for every beer, late night cry, shoulder to lift an extremely heavy piece of equipment, carrying of a 10L water jug on needle karst, home depot trip, chat about the NASH, and more. You are incredible, I truthfully couldn't have done this without you. Thank you also to the graduate students within the Department of Oceanography, and Texas A&M at Galveston Marine and Coastal Environmental Science/Marine biology departments, I have met lifelong friends and colleagues. Thank you also to the graduate students at the University of Southern California for accepting me as a friend and colleague, especially Dr. Joyce Yager and my second set of lab mates: Dr. Hyejung Lee, Dr. Hannah Liddy,

Dr. Christine Wu, Mark Peaple and Emily Tibbett. Your support has meant so much. I'd also like to thank my tertiary lab group, the Woods Hole Oceanographic Institution Coastal Geosystems Group, especially Nicole D'Entremont, Dr. Elizabeth Wallace, Kelly McKeon, and Dr. Jimmy Bramante. Can anyone really stop being your friend after you were stranded in the sea together? Additionally, I would like to thank some stellar undergraduates at both TAMUG and USC who were critical to success in the field and lab: Oscar Cavazos (TAMUG), Olivia Shipley (TAMUG), Laura Myers-Hurt (TAMUG), Efrain Vidal (USC), Hyo Sun (Sunny) Lee (USC).

Importantly, many thanks to Nancy Albury, and all of the staff at Friends of the Environment and the AMMC/National Museum of The Bahamas and permits granted by The Bahamas Environment, Science and Technology (BEST) Commission for logistics support in the Bahamas, including accessibility to my field sites.

CONTRIBUTORS AND FUNDING SOURCES

Contributors

This work was supervised by a dissertation committee that are members of my home department (Oceanography) and all have additional departmental associations. The committee consisted of Dr. Pete van Hengstum (chair, Department of Oceanography/TAMUG Marine and Coastal Environmental Sciences), Dr. Patrick Louchouarn (co-chair, Department of Oceanography/TAMUG Marine and Coastal Environmental Sciences), Dr. Karl Kaiser (Department of Oceanography/TAMUG Marine and Coastal Environmental Sciences), and Dr. Sarah Feakins (Department of Oceanography TAMU/University of Southern California Department of Earth Sciences).

Climate model outputs within Chapter II were run and analyzed by Dr. Sloan Coats, University of Hawaii at Manoa. Biomarker (GDGT) results from Chapter IV were analyzed by Dr. Jessica Tierney and Patrick Murphy at University of Arizona. All other work conducted for this dissertation was completed by the student independently with supervision of the committee.

Technical field, laboratory space, and lab assistance for parts of this work were additionally provided by: Richard Sullivan, Shawna Little, Tyler Winkler, Dr. Jeff Donnelly, Nancy Albury, Dr. David Brankovits, Dr. Pat Fall, Dr. Chris Maupin, Dr. Rainer Amon, Lisa Lavold-Foote, Dana MacDonald, S. Madsen, Y. Wang, Nicole D'Entremont, Kelly McKeon, Dr. Elizabeth Wallace, Oscar Cavazos, Olivia Shipley, Efrain Vidal and Hyo Sun (Sunny) Lee. Additional comments from Dr. John Pohlman,

Dr. Patricia Beddows, Dr. Nemiah Ladd, and Dr. Daolai Zhang have also improved this work.

Funding

This work was partially funded by four summer fellowships (one from the Texas Institute of Oceanography, and three from the TAMUG Office of Research of Graduate Studies Office). Additionally, I have received the Donald and Melba Ross, Susanne ’77 and Steve Leninger, Scherck Louis and Elizabeth Scherck, and Michael T. Halbouty ‘30/AAPGF Foundation Endowed Fellowship as scholarships through the Department of Oceanography/College of Geosciences. Finally, I have received funding during regular semesters for salary and some analyses from the Office of the Chief Academic Officer from TAMUG. Geochemical analyses were funded by US National Science Foundation EAR-1703141 to Dr. Sarah Feakins, EAR-1703087 to Dr. Pete van Hengstum. Sample collection was supported by OCE-1519578, OCE-1356708 to Dr. Pete van Hengstum, and Dr. Jeff Donnelly (WHOI) and BCS-1118340 to Dr. Pat Fall (University of North Carolina).

Field, lab and travel for work related to this dissertation was supplemented by external graduate student research grants: 2016 and 2019 Grants-In-Aid of Graduate Research Grants from Texas Sea Grant, and a 2019 Geological Society of America Graduate Research Grant (NSF Award #1712071). Additionally, multiple funding cycles of internal research grants including: the Mary Mooney Travel Grant, Galveston Graduate Student Research Mini Grant, and the Oceanography Graduate Council

Research Mini Grant. The contents are solely the responsibility of the author and do not necessarily represent the official views of the National Science Foundation, Texas Sea Grant, the Geological Society of America, or the graduate associations at Texas A&M.

TABLE OF CONTENTS

Page

LIST OF FIGURES

Page

LIST OF TABLES

Page

1. INTRODUCTION

1.1. Motivation

The Caribbean Sea and Gulf of Mexico fall within the Intra-American Seas of the subtropical North Atlantic. The centroid pressure and lateral extent of the North Atlantic Subtropical High (NASH), situated west of the Azores, is important regulator of climate in the region, and it's positioning can drive variability in extreme rainfall (Li et al., 2012; Li et al., 2019; Zorzetto and Li, 2021). The work of this dissertation is based on Abaco island in the northern Bahamas, and due to its sensitivity to the NASH, it remains an ideal locale to resolve larger scale ocean-atmospheric factors that can result in regional climate variability. And, although the work of this dissertation is focused within of the 13 Small Island Development States (SIDS) of the Caribbean, defined by the United Nations (UN) to be more vulnerable to environmental challenges (e.g., climate change), there are implications to rainfall patterns including extremes (e.g., floods, droughts) in the Southeastern United States, with potential to impact the livelihood of the ~100 million citizens who live there, and economic and agricultural sustainability in the region.

The United Nations (UN) estimates that ~42 million people reside in the SIDS of the Caribbean. Satellite-era measurements have documented that Caribbean climate is changing (Peterson et al., 2002), and the region has the capacity to experience drought (Herrera et al., 2018). Resultant variations in climate due to warming temperatures (up to 2°C) could place Caribbean SIDS under future freshwater stress (Karnauskas et al.,

2018; Spellman et al., 2021) as increased aridity is projected for the Caribbean region in the 21st century (Lin et al., 2015; Karnauskas et al., 2016). Yet, regional response remains uncertain, in part due to global-scale models not fully capturing aridity changes on SIDS-scale (Karmalkar et al., 2013; Karnauskas et al., 2016). The UN predicts that by 2080, drought in the region could cause $3.8B^{USD} of economic loss (Toba, 2009; Farrell, 2010).

Many SIDS of the Caribbean depend on tourism for economic development, while the remaining economy is comprised of agriculture, fishing, and exports from the shipping industry. For these nations to thrive, it is essential that regular rainfall provides sufficient freshwater to support the tourism industry, agriculture, and local human needs. Much of the freshwater in the Caribbean is supported by shallow coastal aquifers. Dissolution and resultant permeability of the carbonate geology control the supply of freshwater available within the aquifer. Variations in local rainfall feed the freshwater meteoric lens that sits on top of denser, anoxic, saline groundwater below (Whitaker and Smart, 1997). Irregular rainfall, intense storms, and variable aridity can put these freshwater reserves at risk. In 2019, Abaco was devastated by Hurricane Dorian, bringing massive destruction to the islands and their people, emphasizing the need to study this climate-vulnerable area.

1.2. Climate of the Intra-American Seas

Many large-scale ocean-atmospheric factors impact regional rainfall in the northern IAS (Gamble and Curtis, 2008), including: the North Atlantic Subtropical High (NASH) (Li et al., 2012; Martinez et al., 2019), the Intertropical Convergence Zone

(ITCZ) (Hastenrath, 1976), sea-surface temperature (SST) anomalies in the Atlantic warm pool (Wang et al., 2006), and the El Niño Southern Oscillation (ENSO) (Giannini et al., 2000). Thirty years of meteorological data in the Northern Caribbean has documented that precipitation throughout the IAS is varied across short geographic gradients (Jury et al., 2007). Broadly, throughout the northern IAS, there is a dry season from November to April, and a wet season from May-October. However, there is a subtle, spatially variable seasonal drought within the wet season that is termed the 'Mid-Summer Drought', caused by seasonal intensification and displacement of the NASH (Hastenrath, 1976; Gamble et al., 2008).

More moisture can be held in the atmosphere in a warming climate, and it is projected that regions receiving more moisture will become wetter, while current dry zones will be drier into the 21st century (Burls and Fedorov, 2017). Tracking the geographic migration of the descending limb of the Hadley Cell (the NASH), which is a subtropical dry zone, can help inform models and understanding of modern rainfall patterns throughout the Caribbean basin (Li et al., 2012). However, the intensification and lateral extent of the NASH and its effects on regional rainfall patterns is not fully understood, likely due to combined impacts from additional climate factors forcing regional climate variability in the region. Model projections of a southwestern extended NASH suggest increased rainfall in the northern IAS (Campbell et al., 2011), which is in contrast to the compiled reanalysis data within (Li et al., 2012) that suggest decreased precipitation. More drastic seasonal variations of subtropical high (dry zone) mean positions due to variations of latent energy within a warming hemisphere can cause

seasonal delays in precipitation, essentially making precipitation patterns even more difficult to predict into the 21st century (Song et al., 2018).

1.3. Coastal Sinkholes and Blue Holes

Coastal sinkholes are unique, lake-like basins on karst platforms, and their archived sedimentary records can help to resolve past shifts in climate. They are in high density on coasts of the Caribbean, Yucatan, South Pacific, and Florida. These karst basins develop from the collapse and dissolution of the antecedent carbonate, influenced by Quaternary sea-level oscillations promoting carbonate dissolution on the karst platform (Mylroie et al., 1995). They are hydrologically connected to the coastal aquifer, and a layer of dysoxic to anoxic bottom water within the holes can provide ideal conditions for excellent preservation of trapped fossils and sedimentary organic matter, recording often varved (e.g., seasonally laminated) sedimentary archives available for reconstructing hydroclimate and environmental change on Holocene timescales (**Fig. 1:1**). Accumulated sediment is sourced primarily from carbonate particles and organic matter fragments from the adjacent karst landscape, autogenic calcium carbonate generation, and *in situ* production of organic matter.

In a transgressive sea level cycle, internal sedimentary dynamics of coastal sinkholes are driven by variability in local coastal aquifer dynamics (Beddows et al., 2007), often forced by regional sea-level change (van Hengstum et al., 2010). Broadly, depositional processes and the preservation of sediment, are sequentially influenced first by terrestrial conditions, then mixed (aquatic and terrestrial), and eventually marine, if sea level rise completely inundates (floods) a karst basin (coastal blue hole) (Surić et al.,

2005; Gabriel et al., 2009; van Hengstum et al., 2011; Gregory, 2016; van Hengstum et al., 2020). Site specific conditions (e.g., variations in primary productivity, water level, proximity to shoreline) can impact sediment source, input, and preservation (van Hengstum et al., 2020). Through archived sinkhole records, coastal sinkhole and blue hole reconstructions have revealed regional changes in surrounding flora and fauna (Grimm et al., 1993; Kjellmark, 1996; Steadman et al., 2007; Slayton, 2010; Fall et al., 2021), groundwater salinity (Teeter, 1989; Zarikian et al., 2005; van Hengstum et al., 2010; Kovacs et al., 2017), and hurricane activity (Donnelly and Woodruff, 2007; Lane et al., 2011; Denommee et al., 2014; van Hengstum et al., 2016; Wallace et al., 2019; Winkler et al., 2020).

Although coastal sinkholes and blue holes are tidally influenced and hydrographically open (Beddows et al., 2007), they can be relatively quiescent in terms of physical water flow (Yao et al., 2020), and are generally salinity-stratified into three water layers: an upper meteoric lens (fresh to slightly oligohaline), a transitional mixing zone, and a basal saline groundwater layer (Beddows et al., 2007; van Hengstum et al., 2016; van Hengstum et al., 2018; van Hengstum et al., 2020). Previous studies (focusing on dissolved constituents and/or the microbial community) within hydrographically stratified coastal sinkholes have directly addressed biogeochemical processes along their physicochemical gradients, finding sharp changes of redox potential, evidence for chemosynthesis, and complex microbial assemblages that vary relative to water layer mixing and stratification (Humphreys, 1999; Socki et al., 2002; Seymour et al., 2007; Gonzalez et al., 2011; Haas et al., 2018; Ritter et al., 2019; Björnerås et al., 2020; Yao et

al., 2020). Within similar systems on karst platforms that are not aerially exposed (e.g., caves), methane dynamics (Brankovits et al., 2017; Brankovits and Pohlman, 2020), trace metal cycling (Gonneea et al., 2014; McNeill-Jewer et al., 2019; Chen et al., 2020), and organic carbon/phosphorous inputs (Pain et al., 2020), have been found to impact submarine groundwater discharge and coastal biogeochemical cycling on a global scale. For example, high resolution sampling within a Yucatan cave found that 98% of methane was consumed within the subterranean karst aquifer before discharge to the coastal ocean, suggesting that these systems play a role in the global carbon cycle as a methane sink (Brankovits and Pohlman, 2020). The physical, biological and chemical dynamics along the density stratified layers of coastal sinkholes have implications for providing an accessible analogue to modern (e.g., Black sea) or perhaps event ancient oceans (Degens and Stoffers, 1976), coastal carbon cycling (Pohlman, 2011), submarine groundwater discharge, and improvement of paleoenvironmental reconstructions.

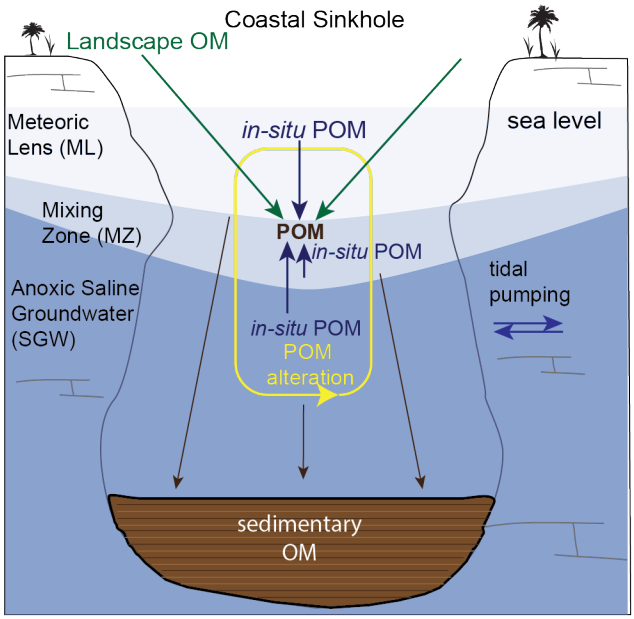

Figure 1:1: Conceptual figure of organic matter inputs to a typical coastal sinkhole.

1.4. Archived geochemical proxies

Proxies for bulk organic matter source (%OM, $\delta^{13}C$, $\delta^{15}N$, C:N) are often used for environmental reconstructions (Lamb et al., 2006; Lone et al., 2018; Van Hardenbroek et al., 2018), and they have been successfully employed on OM accumulating in coastal sinkholes resolving OM source and environmental changes through time (Tamalavage et al., 2018; van Hengstum et al., 2018). However, as bulk properties are a mixed signal of combined biomass, there is interest in using geochemical biomarkers, to isolate individual compounds to further elucidate specific type of OM being produced and accumulating (Freeman and Pancost, 2014). Further, isotopic signatures measured on individual compound classes of specific geochemical markers are useful in yielding quantification of the precursor biochemical processes, which allows for detailed reconstruction of past environments (Hayes et al., 1990).

Specific classes of terrestrially-based lipids (e.g., *n*-alkanes, *n*-alkanoic acids) can be isolated chemically based on their structures (see Figure 1 within (Freeman and Pancost, 2014)), used to reconstruct either past hydroclimate changes or aquatic conditions through time. These biomarkers have been successfully used to reconstruct paleo-environmental change in both tropical and sub-tropical climates on Holocene timescales (Douglas et al., 2012; Dingemans et al., 2014; Lane et al., 2014; Ponton et al., 2014; Hoffmann et al., 2016). The hydrogen isotopic composition of δ^2H measured on terrestrial plant waxes can be used to reconstruct past precipitation δ^2H (Estep and Hoering, 1980; Sternberg, 1988), as it has been found that the hydrogen isotopic composition preserved in geochemical biomarkers (such as plant derived leaf wax lipids) is correlated to the source water that the organism used during photosynthesis (Sessions et al., 1999; Sachse et al., 2012).

Another class of lipids, glycerol diakyl glycerol tetraethers (GDGTs), are sourced from microbial membranes, to reconstruct a variety of environmental conditions (both terrestrial and aquatic) through time (Jenkyns et al., 2004; Schouten et al., 2013). GDGT moieties, including crenarchaeol (Cren) and its regisomer (Cren$'$) are quantified via chromatography, and numbers on peak chromatographs correspond to the molecular structure of the GDGT (Figure 1 within Tierney and Tingley (2015)). The number of cyclopentane and cyclohexane ring moieties within the lipid membranes of marine archaea (isoprenoidal GDGTs) are responsive to sea water temperature (Schouten et al., 2002) and can be calibrated to reconstruct SST through time. Marine (isoprenoidal) GDGTs are primarily sourced from nitrifying *Thaumarchaetoa* (Damsté et al., 2002;

Pester et al., 2011), but GDGTs from *Thaumarchaeota* have also been used within lakes (Powers et al., 2004). Additional GDGTs ratios and indices can support reconstructions of OM sourcing and biogeochemical cycling including : methanogenic *Euryarchaeota* (Zhang et al., 2011), terrigenous inputs as branched GDGTS (brGDGTs) (Damsté et al., 2000; Hopmans et al., 2004; Weijers et al., 2006; Tierney and Russell, 2009), and halophilic archea (archeaol) (Turich and Freeman, 2011).

1.5. Statement of Problem/Dissertation Objective

The Caribbean has been susceptible to severe droughts throughout the Holocene (Horn and Sanford Jr, 1992; Lane et al., 2009; Fritz et al., 2011; Malaizé et al., 2011; Lane et al., 2014). However, like modern spatial variability in Caribbean climate, the effects and impacts of these droughts throughout the late Holocene may not have been uniform basin-wide. For example, the evidence for drying from ~3300 to 2500 years ago, that is documented within archives of the Yucatan, Dominican Republic and northern Bahamas (Higuera-Gundy et al., 1999; Kennedy et al., 2006; van Hengstum et al., 2018), is contrary to evidence for lake level rise in the Lesser Antilles (Fritz et al., 2011). Records from the northeast Caribbean (e.g. the Bahamas and Cuba) suggest drying in the Caribbean over the last millennia (Kjellmark, 1996; Slayton, 2010; Gregory et al., 2015), while proxies from a speleothem in northwestern Cuba (Fensterer et al., 2012), and expansion of pines in Florida (Grimm et al., 2006) suggest an increase in regional moisture during that time period.

The central research objective of this dissertation is thus to use geochemical tracers from two sinkhole basins in the Northern Caribbean to reconstruct hydroclimate in the

northern IAS over the Holocene, with the broader goal of understanding how climate factors (like the NASH) impact regional rainfall. An additional goal of this dissertation is to test and suggest proxy options for reconstructing hydroclimate within sinkhole basins based on what is known about the surrounding ecology, biogeochemistry, and geomorphology. The geochemical evidence produced within this project can be used to constrain model predictions of future changes of hydroclimate in the IAS, and inform coring targets for future paleoenvironmental reconstructions. Individual chapters have associated, specific research questions (see Dissertation Structure), however, this project aims to answer the following overarching questions:

- Can δ^2H signatures of leaf wax biomarkers (*n*-alkanoic acids) be reliably used to reconstruct late Holocene rainfall patterns on a near shoreline sinkhole lake, or a mid-Holocene inland sinkhole lake from the tropics?
    - What technical, geomorphologic, or ecologic limitations are there to the approach (e.g., changes in sedimentation rate and source, local terrestrial vegetation shifts and the presence of salt tolerant mangrove communities)?
- How do current water column conditions impact the suspended particulate organic matter (POM), and bulk/biomarker organic matter (OM) preservation in coastal sinkholes?

1.6. Dissertation structure

This dissertation is organized into chapters to investigate the following specific research questions and themes across three sinkhole basins that vary in coastal position,

diameter, depth, and surrounding vegetation (**Fig. 1:2**):

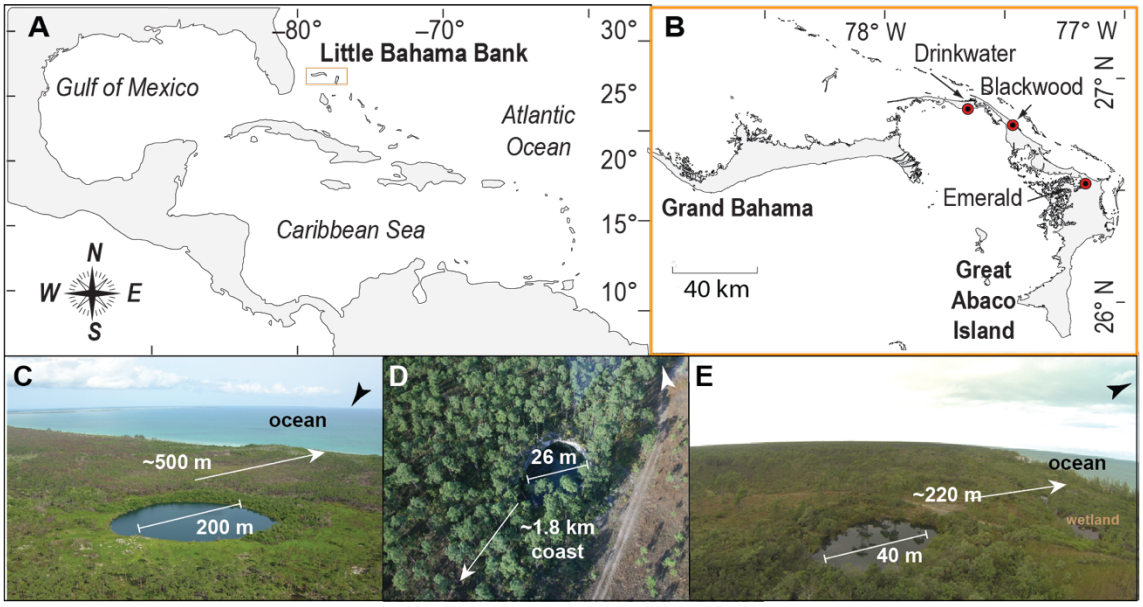

Figure 1:2: Map of sinkhole sites explored within this dissertation.
A) Regional map of the northern Intra-American sea, B), inset map of the Little Bahama Bank, showing Great Abaco Island and sinkholes as red points, C) coastal Drinkwater Sinkhole, Great Abaco, D) inland Emerald Pond, Great Abaco, and E) coastal Blackwood sinkhole.

Chapter II: Plant wax evidence for precipitation and vegetation change from a coastal sinkhole lake in the Bahamas spanning the last 3000 years.

Research Question: How has rainfall on the Bahamas changed over the last 3000 years?

Hypothesis: The composition of δ^2H and $\delta^{13}C$ measured on long-chained terrestrial leaf waxes within the sedimentary organic matter of Blackwood sinkhole will document an increase in rainfall on Abaco during the last millennia, reflected through $\delta^2H_{precipitation}$ through time.

To test this hypothesis: a biomarker record was developed from Blackwood Sinkhole including plant wax *n*-alkanoic acid hydrogen and carbon isotopic evidence for precipitation and ecological change over the last ~3,000 years. Multi-proxy evidence from *n*-alkanoic acid, plant wax *n*-alkanes and mangrove-specific biomarkers were compared to previously published data on bulk organic signatures (Tamalavage et al., 2018) and pollen evidence for vegetation change to account for changes in the plant community and sediment deposition within the sinkhole.

Results: i) When pollen indicates a stable terrestrial plant community (~3000 to 850 cal yrs BP), variations of δ^2H values measured on the plant wax C_{28} *n*-alkanoic acid are interpreted in terms of precipitation isotope (δ^2H_{precip}) changes, with ^2H-enrichment from ~3000 to ~2100 cal yrs BP and ~1700 to 1000 cal yrs BP, ii) interpretation of past hydroclimate is complicated at 850 cal yrs BP, when δ^2H values decrease (−50‰) concurrent with increased *Laguncularia racemosa* (white mangrove) and *Conocarpus erectus* (buttonwood mangrove), and the mangrove-derived biomarker, taraxerol, iii) after correcting for mangrove inputs, estimates of $\delta^2H_{precip\text{-}corr}$ range from –33 to +25‰ throughout the last 3000 years, with uncertainties on the order of 10-20‰, and iv) low $\delta^2H_{precip\text{-}corr}$ values are synchronous with increased abundance of pine pollen, both of which may indicate wetter conditions from 850 cal yrs BP to present.

Chapter III: Paleolimnological evidence of middle Holocene sea-level position and hydroclimate variability from a sinkhole lake in the northern Bahamas.

Research Question: How did rainfall vary during the middle to late Holocene on Abaco Island, as evidenced by δ^2H archived within terrestrial leaf waxes preserved in Emerald Pond?

Hypothesis: The organic matter preserved within the inland sinkhole of Emerald Pond will record variation in mid-late Holocene hydroclimate, and calculated δ^2H net fractionation effects will be less than resultant values measured within Blackwood sinkhole, providing a more coherent $\delta^2H_{precipitation}$ reconstruction of Abaco Island through time.

To test this hypothesis: A multiproxy approach of sedimentology (coarse-grained particle density, bulk organic matter content), and geochemistry ($\delta^{13}C$ and δ^2H on *n*-alkanoic leaf wax) on cores retrieved from Emerald Pond was used to reconstruct hydroclimate and environmental change.

Results: i) a basal peat deposit is accumulating ~8350 cal yr BP and is a terrestrial-limiting sea level indicator, fitting into regional estimates for Holocene sea level, ii) homogeneous deposition of laminated, lacustrine marl from ~8290 to 1700 cal yr BP provides evidence for stabilized water level and aquatic conditions (e.g., high pH) in Emerald Pond that may be insensitive to regional hydrodynamic changes that are impacting other basins on Abaco, and iii) depleted δ^2H values reconstructed from archived terrestrial leaf waxes may indicate wetter conditions in the northern-intra American sea during the mid-Holocene, impacted by NASH dynamics.

Chapter IV: Biomarker and stable isotopic variability of particulate organic matter in two stratified coastal sinkholes in the northern Bahamas.

Research Question: What are the geochemical signatures of suspended POM within the water column of two density stratified sinkholes, and are they maintained/changed during OM transport and preservation in the sediments?

Hypothesis: There will be distinctive geochemical signatures ($\delta^{13}C$, $\delta^{15}N$, C:N, and GDGT ratios) of POM that align with physicochemical gradients within two stratified coastal basins, and are preserved in archived sedimentary OM.

To test this hypothesis: The carbon isotopic composition ($\delta^{13}C$), the nitrogen isotopic composition ($\delta^{15}N$), C:N, and the molecular abundances of GDGTs on filtered POM from depth profiles within two coastal sinkholes on Abaco (Blackwood and Drinkwater) were analyzed. Additionally, the hydrogen ($\delta^{2}H$) and oxygen ($\delta^{18}O$) isotopic composition of water samples along the depth profile were measured. Finally, modern water column POM geochemical measurements were compared to the preserved OM geochemical signatures within Blackwood Sinkhole (van Hengstum et al., 2016; Tamalavage et al., 2018; Tamalavage et al., 2020; Fall et al., 2021).

Results: i) The geochemical signatures ($\delta^{13}C_{POM}$, $\delta^{15}N_{POM}$, and C:N) from suspended particulate matter (SPM) collected during the winter season across physicochemical gradients point to an *in situ* productivity source in the meteoric lens and POM degradation in the mixing zone and saline groundwater, ii) compound specific GDGTs provide biomarker evidence for mixed terrestrial and aquatic (produced *in situ*) throughout the water column, with higher aquatic inputs in the upper meteoric lens, and methanotrophic *Euryarchaeota* and brGDGTs (from terrestrial or bacterial sources) in the mixing zone and saline groundwater, and iii) GDGT biomarkers archived within

Blackwood sinkhole provide evidence that POM produced *in situ* within the upper meteoric lens is indeed being incorporated into the sedimentary OM matrix, recording past sinkhole surface temperature.

1.7. References

Beddows, P.A., Smart, P.L., Whitaker, F.F., Smith, S.L., 2007. Decoupled fresh–saline groundwater circulation of a coastal carbonate aquifer: spatial patterns of temperature and specific electrical conductivity. Journal of Hydrology 346, 18-32.

Björnerås, C., Škerlep, M., Gollnisch, R., Herzog, S.D., Ugge, G.E., Hegg, A., Hu, N., Johansson, E., Lee, M., Pärssinen, V., 2020. Inland blue holes of The Bahamas–chemistry and biology in a unique aquatic environment. Fundamental and Applied Limnology 194, 95-106.

Brankovits, D., Pohlman, J., Niemann, H., Leigh, M., Leewis, M., Becker, K., Iliffe, T., Alvarez, F., Lehmann, M., Phillips, B., 2017. Methane-and dissolved organic carbon-fueled microbial loop supports a tropical subterranean estuary ecosystem. Nature communications 8, 1-12.

Brankovits, D., Pohlman, J.W., 2020. Methane oxidation dynamics in a karst subterranean estuary. Geochimica et Cosmochimica Acta 277, 320-333.

Burls, N.J., Fedorov, A.V., 2017. Wetter subtropics in a warmer world: Contrasting past and future hydrological cycles. Proceedings of the National Academy of Sciences 114, 12888-12893.

Campbell, J.D., Taylor, M.A., Stephenson, T.S., Watson, R.A., Whyte, F.S., 2011. Future climate of the Caribbean from a regional climate model. International Journal of Climatology 31, 1866-1878.

Chen, X., Cukrov, N., Santos, I.R., Rodellas, V., Cukrov, N., Du, J., 2020. Karstic submarine groundwater discharge into the Mediterranean: Radon-based nutrient fluxes in an anchialine cave and a basin-wide upscaling. Geochimica et Cosmochimica Acta 268, 467-484.

Damsté, J.S.S., Hopmans, E.C., Pancost, R.D., Schouten, S., Geenevasen, J.A., 2000. Newly discovered non-isoprenoid glycerol dialkyl glycerol tetraether lipids in sediments. Chemical Communications, 1683-1684.

Damsté, J.S.S., Schouten, S., Hopmans, E.C., Van Duin, A.C., Geenevasen, J.A., 2002. Crenarchaeol. Journal of lipid research 43, 1641-1651.

Degens, E.T., Stoffers, P., 1976. Stratified waters as a key to the past. Nature 263, 22-27.

Denommee, K., Bentley, S., Droxler, A., 2014. Climatic controls on hurricane patterns: a 1200-y near-annual record from Lighthouse Reef, Belize. Scientific reports 4, 3876.

Dingemans, T., Mensing, S.A., Feakins, S.J., Kirby, M.E., Zimmerman, S.R.H., 2014. 3000 years of environmental change at Zaca Lake, California, USA. Frontiers in Ecology and Evolution 2.

Donnelly, J.P., Woodruff, J.D., 2007. Intense hurricane activity over the past 5,000 years controlled by El Niño and the West African monsoon. Nature 447, 465.

Douglas, P.M., Pagani, M., Brenner, M., Hodell, D.A., Curtis, J.H., 2012. Aridity and vegetation composition are important determinants of leaf-wax δD values in southeastern Mexico and Central America. Geochimica et Cosmochimica Acta 97, 24-45.

Estep, M.F., Hoering, T.C., 1980. Biogeochemistry of the stable hydrogen isotopes. Geochimica et Cosmochimica Acta 44, 1197-1206.

Fall, P.L., van Hengstum, P.J., Lavold-Foote, L., Donnelly, J.P., Albury, N.A., Tamalavage, A.E., 2021. Human arrival and landscape dynamics in the northern Bahamas. Proceedings of the National Academy of Sciences 118.

Farrell, D., Trotman, A., Cox, C.S., 2010. Drought Early Warning and Risk Reduction: A Case Study of the Caribbean Drought of 2009–2010. Report.

Fensterer, C., Scholz, D., Hoffmann, D., Spotl, C., Pajon, J.M., Mangini, A., 2012. Cuban stalagmite suggests relationship between Caribbean precipitation and the Atlantic Multidecadal Oscillation during the past 1.3 ka. The Holocene 22, 1405-1412.

Freeman, K.H., Pancost, R., 2014. Biomarkers for Terrestrial Plants and Climate. ElSevier. Report.

Fritz, S.C., Björck, S., Rigsby, C.A., Baker, P.A., Calder-Church, A., Conley, D.J., 2011. Caribbean hydrological variability during the Holocene as reconstructed from crater lakes on the island of Grenada. Journal of Quaternary Science 26, 829-838.

Gabriel, J.J., Reinhardt, E.G., Peros, M.C., Davidson, D.E., van Hengstum, P.J., Beddows, P.A., 2009. Palaeoenvironmental evolution of Cenote Aktun Ha (Carwash) on the Yucatan Peninsula, Mexico and its response to Holocene sea-level rise. Journal of Paleolimnology 42, 199-213.

Gamble, D.W., Curtis, S., 2008. Caribbean precipitation: review, model and prospect. Progress in Physical Geography 32, 265-276.

Gamble, D.W., Parnell, D.B., Curtis, S., 2008. Spatial variability of the Caribbean mid-summer drought and relation to north Atlantic high circulation. International Journal of Climatology 28, 343-350.

Giannini, A., Kushnir, Y., Cane, M.A., 2000. Interannual variability of Caribbean rainfall, ENSO, and the Atlantic Ocean. Journal of Climate 13, 297-311.

Gonneea, M.E., Charette, M.A., Liu, Q., Herrera-Silveira, J.A., Morales-Ojeda, S.M., 2014. Trace element geochemistry of groundwater in a karst subterranean estuary (Yucatan Peninsula, Mexico). Geochimica et Cosmochimica Acta 132, 31-49.

Gonzalez, B.C., Iliffe, T.M., Macalady, J.L., Schaperdoth, I., Kakuk, B., 2011. Microbial hotspots in anchialine blue holes: initial discoveries from the Bahamas. Hydrobiologia 677, 149-156.

Gregory, 2016. The Influence of Morphology on Sinkhole Sedimentation at Little Salt Spring, Florida. Journal of Coastal Research.

Gregory, B.R.B., Peros, M., Reinhardt, E.G., Donnelly, J.P., 2015. Middle-late Holocene Caribbean aridity inferred from foraminifera and elemental data in sediment cores from two Cuban lagoons. Palaeogeography, Palaeoclimatology, Palaeoecology 426, 229-241.

Grimm, E.C., Jacobson, G.L., Watts, W.A., Hansen, B.C., Maasch, K.A., 1993. A 50,000-year record of climate oscillations from Florida and its temporal correlation with the Heinrich events. Science 261, 198-200.

Grimm, E.C., Watts, W.A., Jacobson, G.L., Hansen, B.C.S., Almquist, H.R., Dieffenbacher-Krall, A.C., 2006. Evidence for warm wet Heinrich events in Florida. Quaternary Science Reviews 25, 2197-2211.

Haas, S., De Beer, D., Klatt, J.M., Fink, A., Rench, R.M., Hamilton, T.L., Meyer, V., Kakuk, B., Macalady, J.L., 2018. Low-light anoxygenic photosynthesis and Fe-S-biogeochemistry in a microbial mat. Frontiers in Microbiology 9, 858.

Hastenrath, S., 1976. Variations in low-latitude circulation and extreme climatic events in the tropical Americas. Journal of Atmospheric Sciences 33, 202-215.

Hayes, J., Freeman, K.H., Popp, B.N., Hoham, C.H., 1990. Compound-specific isotopic analyses: a novel tool for reconstruction of ancient biogeochemical processes. Organic Geochemistry 16, 1115-1128.

Herrera, D.A., Ault, T.R., Fasullo, J.T., Coats, S.J., Carrillo, C.M., Cook, B.I., Williams, A.P., 2018. Exacerbation of the 2013–2016 Pan-Caribbean Drought by Anthropogenic Warming. Geophysical research letters 45, 10,619-610,626.

Higuera-Gundy, A., Brenner, M., Hodell, D.A., Curtis, J.H., Leyden, B.W., Binford, M.W., 1999. A 10,300 14 C yr record of climate and vegetation change from Haiti. Quaternary Research 52, 159-170.

Hoffmann, B., Feakins, S.J., Bookhagen, B., Olen, S.M., Adhikari, D.P., Mainali, J., Sachse, D., 2016. Climatic and geomorphic drivers of plant organic matter transport in the Arun River, E Nepal. Earth and Planetary Science Letters 452, 104-114.

Hopmans, E.C., Weijers, J.W., Schefuß, E., Herfort, L., Damsté, J.S.S., Schouten, S., 2004. A novel proxy for terrestrial organic matter in sediments based on branched and isoprenoid tetraether lipids. Earth and Planetary Science Letters 224, 107-116.

Horn, S.P., Sanford Jr, R.L., 1992. Holocene fires in costa rica. Biotropica, 354-361.

Humphreys, W., 1999. Physico-chemical profile and energy fixation in Bundera Sinkhole, an anchialine remiped habitat in north-western Australia. Journal of the Royal Society of Western Australia 82, 89.

Jenkyns, H.C., Forster, A., Schouten, S., Damsté, J.S.S., 2004. High temperatures in the late Cretaceous Arctic Ocean. Nature 432, 888-892.

Jury, M., Malmgren, B.A., Winter, A., 2007. Subregional precipitation climate of the Caribbean and relationships with ENSO and NAO. Journal of Geophysical Research: Atmospheres 112.

Karmalkar, A.V., Taylor, M.A., Campbell, J., Stephenson, T., New, M., Centella, A., Benzanilla, A., Charlery, J., 2013. A review of observed and projected changes in climate for the islands in the Caribbean. Atmósfera 26, 283-309.

Karnauskas, K.B., Donnelly, J.P., Anchukaitis, K.J., 2016. Future freshwater stress for island populations. Nature Climate Change.

Karnauskas, K.B., Schleussner, C.-F., Donnelly, J.P., Anchukaitis, K.J., 2018. Freshwater stress on small island developing states: population projections and aridity changes at 1.5 and 2 C. Regional environmental change 18, 2273-2282.

Kennedy, L.M., Horn, S.P., Orvis, K.H., 2006. A 4000-year record of fire and forest history from Valle de Bao, Cordillera Central, Dominican Republic. Palaeogeography, Palaeoclimatology, Palaeoecology 231, 279-290.

Kjellmark, E., 1996. Late Holocene climate change and human disturbance on Andros Island, Bahamas. Journal of Paleolimnology 15, 133-145.

Kovacs, S.E., Reinhardt, E.G., Chatters, J.C., Rissolo, D., Schwarcz, H.P., Collins, S.V., Kim, S.-T., Nava Blank, A., Luna Erreguerena, P., 2017. Calcite raft geochemistry as a hydrological proxy for Holocene aquifer conditions in Hoyo Negro and Ich Balam (Sac Actun Cave System), Quintana Roo, Mexico. Quaternary Science Reviews 175, 97-111.

Lamb, A.L., Wilson, G.P., Leng, M.J., 2006. A review of coastal palaeoclimate and relative sea-level reconstructions using δ13C and C/N ratios in organic material. Earth-Science Reviews 75, 29-57.

Lane, C.S., Horn, S.P., Kerr, M.T., 2014. Beyond the Mayan lowlands: impacts of the terminal classic drought in the Caribbean Antilles. Quaternary Science Reviews 86, 89-98.

Lane, C.S., Horn, S.P., Mora, C.I., Orvis, K.H., 2009. Late-Holocene paleoenvironmental change at mid-elevation on the Caribbean slope of the Cordillera Central, Dominican Republic: a multi-site, multi-proxy analysis. Quaternary Science Reviews 28, 2239-2260.

Lane, P., Donnelly, J.P., Woodruff, J.D., Hawkes, A.D., 2011. A decadally-resolved paleohurricane record archived in the late Holocene sediments of a Florida sinkhole. Marine Geology 287, 14-30.

Li, L., Li, W., Kushnir, Y., 2012. Variation of the North Atlantic subtropical high western ridge and its implication to Southeastern US summer precipitation. Climate Dynamics 39, 1401-1412.

Li, W., Zou, T., Li, L., Deng, Y., Sun, V.T., Zhang, Q., Layton, J.B., Setoguchi, S., 2019. Impacts of the North Atlantic subtropical high on interannual variation of summertime heat stress over the conterminous United States. Climate Dynamics 53, 3345-3359.

Lin, L., Gettelman, A., Feng, S., Fu, Q., 2015. Simulated climatology and evolution of aridity in the 21st century. Journal of Geophysical Research: Atmospheres 120, 5795-5815.

Lone, A., Fousiya, A., Shah, R., Achyuthan, H., 2018. Reconstruction of paleoclimate and environmental fluctuations since the early Holocene period using organic matter and C: N proxy records: A review. Journal of the Geological Society of India 91, 209-214.

Malaizé, B., Bertran, P., Carbonel, P., Bonnissent, D., Charlier, K., Galop, D., Imbert, D., Serrand, N., Stouvenot, C., Pujol, C., 2011. Hurricanes and climate in the Caribbean during the past 3700 years BP. The Holocene 21, 911-924.

Martinez, C., Goddard, L., Kushnir, Y., Ting, M., 2019. Seasonal climatology and dynamical mechanisms of rainfall in the Caribbean. Climate dynamics 53, 825-846.

McNeill-Jewer, C.A., Reinhardt, E.G., Collins, S., Kovacs, S., Chan, W.M., Devos, F., LeMaillot, C., 2019. The effect of seasonal rainfall on nutrient input and biological productivity in the Yax Chen cave system (Ox Bel Ha), Mexico, and implications for μXRF core studies of paleohydrology. Palaeogeography, Palaeoclimatology, Palaeoecology 534, 109289.

Mylroie, J.E., Carew, J.L., Vacher, H., 1995. Karst development in the Bahamas and Bermuda. Geological Society of America Special Papers 300, 251-267.

Pain, A.J., Martin, J.B., Young, C.R., Valle-Levinson, A., Mariño-Tapia, I., 2020. Carbon and phosphorus processing in a carbonate karst aquifer and delivery to the coastal ocean. Geochimica et Cosmochimica Acta 269, 484-495.

Pester, M., Schleper, C., Wagner, M., 2011. The Thaumarchaeota: an emerging view of their phylogeny and ecophysiology. Current opinion in microbiology 14, 300-306.

Peterson, T.C., Taylor, M.A., Demeritte, R., Duncombe, D.L., Burton, S., Thompson, F., Porter, A., Mercedes, M., Villegas, E., Fils, R.S., 2002. Recent changes in climate extremes in the Caribbean region. Journal of Geophysical Research: Atmospheres 107, ACL 16-11-ACL 16-19.

Pohlman, J.W., 2011. The biogeochemistry of anchialine caves: progress and possibilities. Hydrobiologia 677, 33-51.

Ponton, C., West, A.J., Feakins, S.J., Galy, V., 2014. Leaf wax biomarkers in transit record river catchment composition. Geophysical Research Letters 41, 6420-6427.

Powers, L.A., Werne, J.P., Johnson, T.C., Hopmans, E.C., Damsté, J.S.S., Schouten, S., 2004. Crenarchaeotal membrane lipids in lake sediments: a new paleotemperature proxy for continental paleoclimate reconstruction? Geology 32, 613-616.

Ritter, S.M., Isenbeck-Schröter, M., Scholz, C., Keppler, F., Gescher, J., Klose, L., Schorndorf, N., Avilés Olguín, J., González-González, A., Stinnesbeck, W., 2019. Subaqueous speleothems (Hells Bells) formed by the interplay of pelagic redoxcline biogeochemistry and specific hydraulic conditions in the El Zapote sinkhole, Yucatán Peninsula, Mexico. Biogeosciences 16, 2285-2305.

Sachse, D., Billault, I., Bowen, G.J., Chikaraishi, Y., Dawson, T.E., Feakins, S.J., Freeman, K.H., Magill, C.R., McInerney, F.A., Van Der Meer, M.T., 2012. Molecular paleohydrology: interpreting the hydrogen-isotopic composition of lipid biomarkers from photosynthesizing organisms. Annual Review of Earth and Planetary Sciences 40, 221-249.

Schouten, S., Hopmans, E.C., Damsté, J.S.S., 2013. The organic geochemistry of glycerol dialkyl glycerol tetraether lipids: A review. Organic geochemistry 54, 19-61.

Schouten, S., Hopmans, E.C., Schefuß, E., Damste, J.S.S., 2002. Distributional variations in marine crenarchaeotal membrane lipids: a new tool for reconstructing ancient sea water temperatures? Earth and Planetary Science Letters 204, 265-274.

Sessions, A., TW, B., A, S., Hayes, J., 1999. Fractionation of hydrogen isotopes in lipid biosynthesis. Organic Geochemistry 30, 1193-1200.

Seymour, J., Humphreys, W., Mitchell, J., 2007. Stratification of the microbial community inhabiting an anchialine sinkhole. Aquatic Microbial Ecology 50, 11-24.

Slayton, I.A., 2010. A vegetation history from Emerald Pond, Great Abaco Island, the Bahamas, based on pollen analysis.

Socki, R.A., Perry, E.J.C., Romanek, C.S., 2002. Stable isotope systematics of two cenotes from the northern Yucatan Peninsula, Mexico. Limnology and Oceanography 47, 1808-1818.

Song, F., Leung, L.R., Lu, J., Dong, L., 2018. Future Changes in Seasonality of the North Pacific and North Atlantic Subtropical Highs. Geophysical Research Letters 45, 11,959-911,968.

Spellman, P., Pritt, A., Salazar, N., 2021. Tracking changing water budgets across the bahamian archipelago. Journal of Hydrology, 126178.

Steadman, D.W., Franz, R., Morgan, G., Albury, N.A., Kakuk, B., Broad, K., Franz, S.E., Tinker, K., Pateman, M.P., Lott, T.A., Jarzen, D.M., Dilcher, D.L., 2007. Exceptionally well preserved late Quaternary plant and vertebrate fossils from a blue hole on Abaco, The Bahamas. Proceedings of the National Academy of the Sciences 104, 19897-19902.

Sternberg, L.d.S.L., 1988. D/H ratios of environmental water recorded by D/H ratios of plant lipids. Nature 333.

Surić, M., Juračić, M., Horvatinčić, N., Bronić, I.K., 2005. Late Pleistocene–Holocene sea-level rise and the pattern of coastal karst inundation: records from submerged speleothems along the Eastern Adriatic Coast (Croatia). Marine Geology 214, 163-175.

Tamalavage, A.E., van Hengstum, P.J., Louchouarn, P., Fall, P.L., Donnelly, J.P., Albury, N.A., Coats, S., Feakins, S.J., 2020. Plant wax evidence for precipitation and vegetation change from a coastal sinkhole lake in the Bahamas spanning the last 3000 years. Organic Geochemistry 150, 104120.

Tamalavage, A.E., van Hengstum, P.J., Louchouarn, P., Molodtsov, S., Kaiser, K., Donnelly, J.P., Albury, N.A., Fall, P.L., 2018. Organic matter sources and lateral sedimentation in a Bahamian karst basin (sinkhole) over the late Holocene: Influence of local vegetation and climate. Palaeogeography, Palaeoclimatology, Palaeoecology 506, 70-83.

Teeter, J.W., Year. Proceedings of Pleistocene and Holocene carbonate environments on San Salvador Island, Bahamas: International Geological Congress, 28th, Washington, Field Trip Guidebook T 175, pp. 35-40.

Tierney, J.E., Russell, J.M., 2009. Distributions of branched GDGTs in a tropical lake system: implications for lacustrine application of the MBT/CBT paleoproxy. Organic Geochemistry 40, 1032-1036.

Tierney, J.E., Tingley, M.P., 2015. A TEX 86 surface sediment database and extended Bayesian calibration. Scientific data 2, 1-10.

Toba, N., 2009. Potential economic impacts of climate change in the Caribbean Community. Assessing the potential consequences of climate destabilization in Latin America.

Turich, C., Freeman, K.H., 2011. Archaeal lipids record paleosalinity in hypersaline systems. Organic Geochemistry 42, 1147-1157.

Van Hardenbroek, M., Chakraborty, A., Davies, K., Harding, P., Heiri, O., Henderson, A., Holmes, J., Lasher, G., Leng, M., Panizzo, V., 2018. The stable isotope composition of organic and inorganic fossils in lake sediment records: Current understanding, challenges, and future directions. Quaternary Science Reviews 196, 154-176.

van Hengstum, P.J., Donnelly, J.P., Fall, P.L., Toomey, M.R., Albury, N.A., Kakuk, B., 2016. The intertropical convergence zone modulates intense hurricane strikes on the western North Atlantic margin. Scientific Reports 6, 1-10.

van Hengstum, P.J., Maale, G., Donnelly, J.P., Albury, N.A., Onac, B.P., Sullivan, R.M., Winkler, T.S., Tamalavage, A.E., MacDonald, D., 2018. Drought in the northern Bahamas from 3300 to 2500 years ago. Quaternary Science Reviews 186, 169-185.

van Hengstum, P.J., Reinhardt, E.G., Beddows, P.A., Gabriel, J.J., 2010. Linkages between Holocene paleoclimate and paleohydrogeology preserved in a Yucatan underwater cave. Quaternary Science Reviews 29, 2788-2798.

van Hengstum, P.J., Scott, D.B., Gröcke, D.R., Charette, M.A., 2011. Sea level controls sedimentation and environments in coastal caves and sinkholes. Marine Geology 286, 35-50.

van Hengstum, P.J., Winkler, T.S., Tamalavage, A.E., Sullivan, R.M., Little, S.N., MacDonald, D., Donnelly, J.P., Albury, N.A., 2020. Holocene sedimentation in a blue hole surrounded by carbonate tidal flats in The Bahamas: Autogenic versus allogenic processes. Marine Geology 419, 106051.

Wallace, E., Donnelly, J., van Hengstum, P., Wiman, C., Sullivan, R., Winkler, T., d'Entremont, N., Toomey, M., Albury, N., 2019. Intense hurricane activity over the past 1500 years at South Andros Island, The Bahamas. Paleoceanography and Paleoclimatology.

Wang, C., Enfield, D.B., Lee, S.-k., Landsea, C.W., 2006. Influences of the Atlantic warm pool on Western Hemisphere summer rainfall and Atlantic hurricanes. Journal of climate 19, 3011-3028.

Weijers, J.W., Schouten, S., Spaargaren, O.C., Damsté, J.S.S., 2006. Occurrence and distribution of tetraether membrane lipids in soils: Implications for the use of the TEX86 proxy and the BIT index. Organic Geochemistry 37, 1680-1693.

Whitaker, F.F., Smart, P.L., 1997. Hydrogeology of Bahamian archipelago, in: Vacher, H.L., Quinn, T.M. (Eds.), Geology and hydrogeology of carbonate islands: Developments in Sedimentology 54. Elsevier Science Publishers, pp. 183-216.

Winkler, T.S., van Hengstum, P.J., Donnelly, J.P., Wallace, E.J., Sullivan, R.M., MacDonald, D., Albury, N.A., 2020. Revising evidence of hurricane strikes on Abaco Island (The Bahamas) over the last 700 years. Scientific reports 10, 1-17.

Yao, P., Wang, X., Bianchi, T., Yang, Z., Fu, L., Zhang, X., Chen, L., Zhao, B., Morrison, E., Shields, M., 2020. Carbon cycling in the world's deepest blue hole. Journal of Geophysical Research: Biogeosciences 125, e2019JG005307.

Zarikian, C.A.A., Swart, P.K., Gifford, J.A., Blackwelder, P.L., 2005. Holocene paleohydrology of Little Salt Spring, Florida, based on ostracod assemblages and stable isotopes. Palaeogeography, Palaeoclimatology, Palaeoecology 225, 134-156.

Zhang, Y.G., Zhang, C.L., Liu, X.-L., Li, L., Hinrichs, K.-U., Noakes, J.E., 2011. Methane Index: A tetraether archaeal lipid biomarker indicator for detecting the instability of marine gas hydrates. Earth and Planetary Science Letters 307, 525-534.

Zorzetto, E., Li, L., 2021. Impacts of the North Atlantic Subtropical High on Daily Summer Precipitation over the Conterminous United States. Journal of Hydrometeorology.

2. PLANT WAX EVIDENCE FOR PRECPITATION AND VEGETATION CHANGE FROM A COASTAL SINKHOLE LAKE IN THE BAHAMAS SPANNING THE LAST 3,000 YEARS*

2.1. Introduction

Many small island nations in the Caribbean with limited water storage capacity are at risk of extreme freshwater stress in the 21st century (Lin et al., 2015; Karnauskas et al., 2016; Karnauskas et al., 2018). The Caribbean region has been susceptible to drought throughout the historical and satellite intervals, including a severe drought in 2013-2016 (Herrera et al., 2018). Although there is evidence for an overall drying pattern from the middle Holocene to the present associated with Holocene insolation patterns (Hodell et al., 1991; Haug et al., 2001b), there also have been multiple severe droughts on centennial timescales (Horn and Sanford Jr, 1992; Lane et al., 2009; Fritz et al., 2011; Malaizé et al., 2011). Such variations in regional climate have been proposed to cause ecological change in The Bahamas (Kjellmark, 1996; Slayton, 2010), and have been linked to socioeconomic transitions among the Mayans in the Yucatan (Hodell et al., 1991; Haug et al., 2003) and smaller populations in the Dominican Republic (Lane et al., 2014). Yet there may be opposing signs of hydroclimate change across the Caribbean

*Reprinted with permission from "Plant wax evidence for precipitation and vegetation change from a coastal sinkhole lake in the Bahamas spanning the last 3000 years." by Tamalavage, A.E., van Hengstum, P.J., Louchouarn, P., Fall, P.L., Donnelly, J.P., Albury, N.A., Coats, S., Feakins, S.J., 2020. Organic Geochemistry 150, 104120.

(Bhattacharya and Coats, 2020). Additional drought records are needed, and here we test plant waxes for their potential to reconstruct hydroclimate in the Caribbean.

Plant wax hydrogen isotopic applications in tropical and sub-tropical climates include evidence for changes in Holocene hydroclimate in India based on *n*-alkanes (Sarkar et al., 2015), and changes in *n*-alkanoic acids across the last glacial into the Holocene driven by the South American Southern Monsoon (Fornace et al., 2014) and the North American Monsoon (Bhattacharya et al., 2017). Central American and Caribbean plant wax *n*-alkane records include those from the highlands of Costa Rica (Lane and Horn, 2013), and lakes in the lesser Antilles (Lane et al., 2014). However, there are a limited number of plant wax reconstructions derived from sinkhole or blue hole basins, including sinkhole sedimentary records studied in the Yucatan (Douglas et al., 2012).

In general, the hydrogen isotopic composition of biomarkers is correlated to source water modified by a large fractionation associated with a series of biosynthetic steps (Sessions et al., 1999). The relationship between source water and the isotopic composition of precipitation has been documented on large scale transect surveys of living plants, soils or lake sediments (Sachse et al., 2012), direct studies of plant waters in sub-tropical, dry climates (Feakins and Sessions, 2010a) and tropical, wet climates (Feakins et al., 2016a). In the tropics, precipitation isotopic composition may respond to the "amount effect" with ^{2}H-enrichment (^{2}H-depletion) associated with drier (wetter) conditions (Lee et al., 2009). This effect can be amplified as leaf water ^{2}H-enrichment in dry climates can lead to smaller net fractionations (Feakins and Sessions, 2010a),

resulting in further ^{2}H-enrichment of the plant wax. Terrestrial plant wax biomarkers preserved in geological records have thus been used to infer past wet/dry shifts, commonly using *n*-alkanes (Schefuß et al., 2005) and *n*-alkanoic acids (Tierney, 2008). Landscape vegetation dynamics can complicate the paleohydrological evidence that is recorded by plant waxes in some lake sediment archives (Douglas et al., 2012; Fornace et al., 2014). There are documented differences in biological factors between plant life form (e.g. trees, shrubs, graminoids) (Liu and Yang, 2008) and species (Sachse et al., 2012) due to leaf physiology (Smith and Freeman, 2006; Kahmen et al., 2013; Gao et al., 2015), phenology (Tipple et al., 2013) and biogeochemical pathway (Feakins and Sessions, 2010b). Therefore, plant wax reconstructions are ideally paired with evidence of plant communities in order to monitor vegetation change. This can be achieved by pairing carbon isotopic measurements on the same molecules (Nelson et al., 2013; Feakins et al., 2019), analyzing chain length distributions of particular compound classes (Fornace et al., 2014) and/or incorporating fossil pollen evidence of variations in taxa (Feakins, 2013; Sarkar et al., 2015; Lane et al., 2016; Nelson and Sachs, 2016; Freimuth et al., 2017).

In coastal environments, the source water accessed by mangroves may be a mixture of seawater and meteoric water, each of which has distinct $\delta^{2}H$ values. Salinity variations further complicate the recorded signal by altering the hydrogen isotopic fractionation between source water and plant lipids (Ladd and Sachs, 2012; Sachse et al., 2012). One approach to detect salinity changes in estuarine or lagoonal environments (Ladd and Sachs, 2015a; Ladd and Sachs, 2015b), has been to study the $\delta^{2}H$ values of

taraxerol, the dominant sterol in *Rhizophora mangle* (red mangrove) leaves (Killops and Frewin, 1994; Koch et al., 2003). Field-based studies indicate that the net fractionation ($\varepsilon_{wax/w}$) between source water δ^2H and taraxerol δ^2H values increased 0.9 ± 0.2 ‰/ppt in salinity for *R. mangle* leaves in Micronesia (Ladd et al., 2015), and 0.5–1.0 ‰/ppt for *n*-alkanes extracted from three mangrove species growing across a salinity gradient within an Australian estuary (Ladd et al., 2015). In contrast, a laboratory-based cultivation study found a decrease in net fractionation with increased salinity (Park et al., 2019). Although uncertainties are large, some studies have attempted to deconvolve the changes in source water isotopic composition and salinity-dependent fractionations across salinity gradients by combining the signals from aquatic and mangrove biomarkers (Nelson and Sachs, 2016). More generally, mangrove inputs to sediments can be monitored through the use of both pollen and biomarker compounds (Versteegh et al., 2004). We thus propose to use the presence of pollen or mangrove biomarkers (e.g., taraxerol) as a diagnostic tool for inferring when mangrove inputs may modulate the signal recorded by *n*-alkyl plant wax biomarkers.

In pursuing this objective, we reconstruct regional hydroclimate variability from a 3,000-year sediment record from Blackwood Sinkhole on Great Abaco Island in The Bahamas. Prior work on the bulk organic matter preserved within Blackwood Sinkhole has indicated shifts in the proportional inputs from both allochthonous material from the surrounding landscape (tropical, wet forest and mangrove marsh) and autochthonous productivity in the upper water column (Tamalavage et al., 2018). We develop a biomarker record from Blackwood Sinkhole including plant wax *n*-alkanoic acid

hydrogen and carbon isotopic evidence for precipitation and ecological change over the last ~3,000 years. We compare multi-proxy evidence from *n*-alkanoic acid, plant wax *n*-alkanes and mangrove-specific biomarkers, to previously published data on bulk organic signatures (Tamalavage et al., 2018) and preliminary pollen evidence for vegetation change (van Hengstum et al. 2016) to account for changes in the plant community and sediment deposition associated with the sinkhole. A paired pollen and plant wax approach provides solutions when working in small catchments with large ecological shifts (Fornace et al., 2016). In this case, the paired approach is used to screen, and attempt to correct for, mangrove biases and to develop a late Holocene precipitation isotope record for the northeastern Bahamas.

2.2. Study Site

2.2.1. Blackwood Sinkhole

Blackwood Sinkhole is located 220 m inland from the northeastern coast of Great Abaco Island on the Little Bahama Bank (26.79°N, 77.42°W; **Fig. 2:1**). This 32 m diameter, steep-sided sinkhole lake has a water depth of 33–38 m below sea level (mbsl), and a tidal range of ~1 m. A secondary, cylindrical karst feature (water depth ~46–61 mbsl) is connected to Blackwood Sinkhole through a cave tunnel at 32 mbsl. The sinkhole is bordered by significant mangrove wetland development on its eastern periphery (**Fig. 2:1c**), and is a groundwater-fed basin (proximal connection to the ocean) that receives no stream discharge. The sinkhole is hydrographically stratified, with surface salinity in the low oligohaline range (1.4 psu, most recent cast July 2019) and anoxic, saline groundwater from 15 to 40 mbsl.

We identified and analyzed biomarkers from a 1.22 m sediment core (BLWD-C2) previously collected in 2011 from Blackwood Sinkhole (van Hengstum et al., 2016). Radiocarbon dating of terrestrial plant macrofossils indicated a nearly constant sedimentation rate in the sinkhole over the last 3,000 calibrated years before present (cal yrs BP, where present is 1950 CE; 0.3 to 0.6 mm/yr based on a Bayesian statistical approach, simple least squares linear regression: $r^2 = 0.99$, n = 11 dates) (van Hengstum et al., 2016; Tamalavage et al., 2018). Sediments are comprised of calcium carbonate and organic matter, with organic matter contributions from aquatic productivity and inputs from adjacent terrestrial and mangrove environments (Tamalavage et al., 2018).

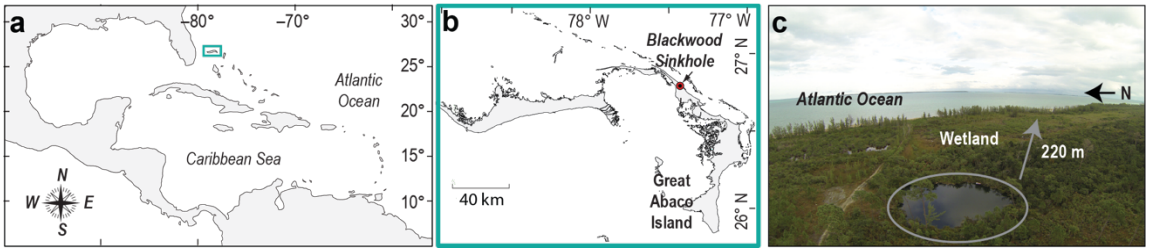

Figure 2:1: Map of Blackwood Sinkhole on Great Abaco Island.
a) Caribbean region, green box expanded, b) inset showing location of Blackwood Sinkhole, c) photo of Blackwood Sinkhole (photo credit: Pete van Hengstum).

2.2.2. Climate

The nearest meteorological station with rainfall isotopic data is Havana, Cuba (600 km southwest of Abaco Island), where Mean Annual Precipitation (MAP) is 1470 mm. Abaco Island has similar precipitation seasonality, with MAP of 1400 mm between 1951 and 1981 (Jury et al., 2007). Abaco has no record of isotopic data, therefore isotopic compositions from Havana will be used to infer likely δ^2H seasonality at Abaco.

At the Havana station, the weighted MAP δ^2H is –11.8‰ (1σ = 8.0‰, 14 years, 2002–2016, IAEA/WMO, 2019; **Fig. 2:2**), and temperature seasonality is minimal (20.7–26.6˚C monthly mean). The wet season lasts from May to October (~195 mm/month, mean δ^2H –15.2‰), and the dry season from November to April (~50 mm/month, mean δ^2H –3.5‰).

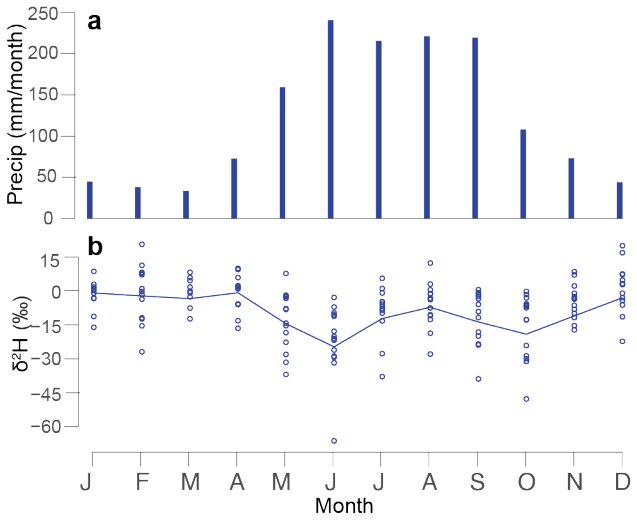

Figure 2:2: Precipitation amount and hydrogen isotopic composition.
Showing a) monthly mean precipitation amount, and b) monthly measurements and weighted climatological mean δ^2H precipitation, from Havana, Cuba (Centro de Proteccion e Higiene de la Radiacion; CPHR) based on 154 measurements taken from 2002–2016 (IAEA/WMO, 2019). The rainy season (May-October; mean δ^2H –15.2‰) is ~12‰ ^2H-depleted relative to the dry season (mean –3.5‰).

Latitudinal migration of the Intertropical Convergence Zone (ITCZ), pressure and geographic changes to the variability in the intensity and extent of the North Atlantic Subtropical High (NASH), and variability in the strength of the Caribbean Low Level Jet (CLLJ) all contribute to seasonal rainfall variability across the tropical North Atlantic

region (Jury et al., 2007; Gamble and Curtis, 2008; Martin and Schumacher, 2011; Li et al., 2012; Martinez et al., 2019). In the modern climate, rainfall across the Bahamian archipelago is highly sensitive to seasonal variability in the intensity (i.e. stronger being higher central pressure), and geographic position of the NASH. For example, (Hasanean, 2004) determined that NASH intensity was greatest (weakest) during boreal summer (winter) from 1960 to 1990 CE using NCEP-NCAR reanalysis data gridded at 2.5° x 2.5°. It has been further determined that the geographic position of the westward margin of the NASH regulates rainfall on the Caribbean and SE United States (Li et al., 2011; Li et al., 2012).

In order to understand the linkages between precipitation isotopes and atmospheric conditions, we identify the 2.5% of years (75 total years) with the most ^{2}H-enriched and ^{2}H-depleted rainfall in three forced transient simulations of the time period 850–1849 C.E. (including all external forcing factors—volcanic, greenhouse gas, solar) with the isotope enabled Community Earth System Model (iCESM) (Brady et al., 2019). While the iCESM struggles to reproduce the observed seasonal cycle of δ^{2}H (**Appendix A, Fig. 1**) and precipitation (**Appendix A, Fig. 1h**) at Havana, Cuba, with an exaggerated midsummer drought and a mean offset, the difference between wet and dry years appear to be well captured by the model (**Appendix A Fig. 1a-c versus Fig. 1d-f**). Ideally, forced transient simulations covering the same time period as the reconstruction would be available for this analysis. While such simulations do not exist, the boundary conditions are largely stable (except on longer than centennial timescales) in the late Holocene and thus interannual variability should be similar for sub samples of the

reconstructed time period. Together these results suggest that iCESM simulations will be useful for interpreting the regional-to-large scale climate dynamics underlying local variability in δ^2H.

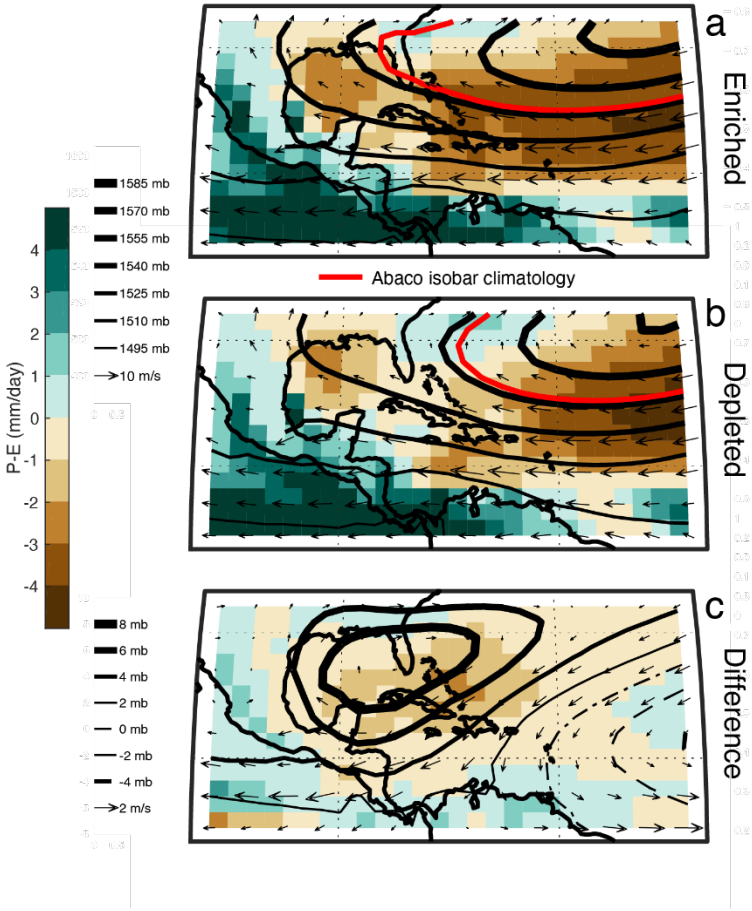

Figure 2:3: Comparison of May-October precipitation minus evaporation. With (P-E, color), 850 mb wind (vectors), and 850 mb geopotential height (contours) highlighting the climatological isobar that sits over Abaco (red line) for the 2.5% most a) ^2H-enriched and b) ^2H-depleted rainfall years, and the c) difference, near Abaco (average of 40 years total) from four isotope enabled Community Earth System Model last millennium simulations (iCESM—forced transient between 850–1850 C.E.). The most ^2H-enriched and ^2H-depleted years were calculated for the average of all spatial grid points within 300km of Abaco (26.79°N, 282.58°E). ^2H-enriched rainfall over Abaco corresponds to an expanded NASH (see red line) and stronger CLLJ, which lead to greater local atmospheric stability and greater moisture export out of the Carribean,

respectively, and ^{2}H-depleted rainfall corresponds to a contracted NASH and weaker CLLJ.

In the composite of the 1% of most ^{2}H-enriched years, we find the NASH intensifies and expands (**Fig. 2:3a**), suppressing convection over the Caribbean. At the same time a stronger Caribbean Low Level Jet (CLLJ) increases moisture export (divergence) away from the Caribbean. Together these conditions bring drier conditions across a large area of the Caribbean (**Fig. 2:3c**). Conversely, in the most ^{2}H-depleted years, the NASH is weak (i.e. lower central pressure) and contracted (i.e. western boundary as defined by the 850 mbar is displaced further to the East) (**Fig. 2:3b**), the CLLJ is weak, and there are wetter conditions across the Caribbean. Filtering to isolate multidecadal (the nominal resolution of the reconstructions—see Methods) and longer timescale variability produces similar, though expectedly muted differences between ^{2}H-depleted and enriched periods. The same dynamics that are associated with isotopic variability over The Bahamas have been shown to also control the large scale patterns of hydroclimate variability across the Mesoamerican-Caribbean region (Bhattacharya and Coats, 2020).

2.3. Methods

2.3.1. Lipid extraction

Previously analyzed pollen samples were collected every 10 mm, with each sample integrating 5 mm of core and up to ~12 years of inputs (Fall unpublished data; van Hengstum et al. 2016; Tamalavage et al., 2018). Sediment sub-samples were collected for biomarker analysis every 30 mm (~every 72 years) with each sample integrating 10 mm of core, or ~24 years of inputs, while 17 biomarker samples were

screened downcore for sterol compounds (Supplemental Information, Figure S2). Samples for biomarker analysis were freeze dried and homogenized with a mortar and pestle. Dry, powdered sediment samples (about 1–2 gdw) were extracted with an Accelerated Solvent Extraction system (ASE 350®, DIONEX) with 9:1 ratio of dichloromethane (DCM):methanol (MeOH) at 100˚C and 1500 psi (2 x 15-min). The extract was separated using column chromatography (5 cm x 40 mm Pasteur pipette, NH_2 Sepra brand bulk packing, 60 Å), eluting with 2:1 DCM:isopropanol, followed by 4% HCO_2H in diethyl ether, yielding neutral and acid fractions respectively. The neutral fraction was separated by column chromatography (5 cm x 40 mm Pasteur pipette, 5% water-deactivated silica gel, 100–200 mesh) by eluting with hexanes to separate n-alkanes from the rest of the neutral fraction (eluted with DCM and methanol, including sterols, hence "sterol fraction"). Sulfur was removed from the *n*-alkane fraction by eluting over activated copper filings. The acid fraction containing *n*-alkanoic acids was methylated with 5% HCl and 95% MeOH (with methyl group of known isotopic composition: δ^2H −186.9‰ ± 3.7; 1σ; $\delta^{13}C$ −24.7‰ ± 0.2) at 70°C for 12 hours to yield corresponding fatty acid methyl esters (FAMEs). Measured FAME isotopic compositions were corrected for the added methyl group to yield the isotopic composition of the original fatty acid by mass balance. Excess milliQ water was added to the hydrolyzed products, and the lipids were partitioned into hexane and dried by passing through anhydrous Na_2SO_4. Lipids were further purified using column chromatography (5 cm x 40 mm Pasteur pipette, 5% water-deactivated silica gel, 100–200 mesh), eluting with hexane first and then with DCM to isolate the FAME fraction.

2.3.2. Biomarker identification and quantification

We identified the *n*-alkanes and *n*-alkanoic acids (the latter as fatty acid methyl esters, FAME) by gas chromatography (GC) mass spectrometry (MS) and quantified these compounds by a flame ionization detector (FID), using an Agilent GC-MSD/FID. *n*-Alkanes and FAME fractions were dissolved in hexane and injected via a split/splitless inlet in splitless mode, to a capillary column (Rxi®-5ms 30 m x 0.25 mm, film thickness 0.25 μm). Quantification was achieved using an in-house standard comprised of a mixture of 4 *n*-alkanes and 3 *n*-alkanoic acids of varied and known concentration, with the linear calibrations determined separately for the two compound classes. The *n*-alkanoic acid fractions are reported relative to the dry weight of the sediment used in lipid extraction, with *n*-alkanes determined for a subset.

For the *n*-alkanoic acids, we calculated the carbon preference index (CPI) or even over odd carbon chain length preference as:

$$CPI = 2\,\Sigma C_n / (\Sigma C_{n-1} + \Sigma C_{n+1}) \quad (1)$$

where $n = C_{24}, C_{26}, C_{28}, C_{30}$.

We calculate the average chain length (ACL), the weighted average accounting for concentration (C_n) of each compound (n) as:

$$ACL = \Sigma\,(C_n \cdot n) / \Sigma C_n \quad (2)$$

The *n*-alkanoic acid concentrations were summed as:

$$\Sigma_{acids} = \Sigma_i^n\,[C_n] \quad (3)$$

We similarly calculate the same ratios for the *n*-alkanes except for the CPI, the odd to even preference, and the n = C_{27}-C_{33} range. In addition, we report the modal chain lengths of each compound class and the ratio of Σ_{acids}:$\Sigma_{alkanes}$.

We studied the sterol fraction of a subset of the samples (n = 17) to identify biomarkers for mangroves, specifically taraxerol. Samples were derivatized using 25 µl of N,O-Bis(trimethylsilyl)trifluoroacetamide (BSTFA) with trimethylchlorosilane trimethylsilyl chloride (TMCS; 99:1 v/v) and 100 µl of pyridine, reacting at 70˚C for 20 mins. Samples were dissolved in DCM (375 µl) and analysed by GC-MS/FID. Compound identification was made by comparison of MS m/z spectra to those in the literature (Killops and Frewin, 1994). Sterols were quantified by comparison of FID peak area for the analyte relative to that of a 4-point in-house linear calibration of cholestane. In addition, we calculated taraxerol/$\Sigma_{alkanes}$ to account for concentration changes such as clastic dilution of both plant components to the sedimentary matrix and to reveal relative changes in mangrove inputs.

2.3.3. Compound-specific hydrogen and carbon isotopic analysis

Compound-specific hydrogen isotopic values were obtained using gas chromatography isotope ratio mass spectrometry (GC-IRMS). We used a Thermo Scientific Trace gas chromatograph equipped with a Rxi-5ms column (30 m x 0.25 mm, film thickness 0.25 µm) and a programmable temperature vaporizing (PTV) injector. Injections were performed via the PTV inlet operated in solvent split mode, whereby the solvent was evaporated at 60°C in split mode, then the temperature raised to 280°C for

transfer of analytes to the GC column in splitless mode. The GC was connected via a GC Isolink with pyrolysis furnace (at 1400°C) via a Conflo IV interface to a DeltaVPlus isotope ratio mass spectrometer. To check for linearity, the H_3^+ factor was measured daily and remained close to 4 ppm mV^{-1} (across 1−8 V); for CO_2 the standard deviation of reference pulses was better than 0.9‰. Reference peaks of H_2 or CO_2 were co-injected during the course of a GC-IRMS run; two were used for standardization. Samples were interspersed with standard compound mixtures of known isotopic composition, with several standards run per day. The results are reported using conventional delta notation (δ^2H and $\delta^{13}C$ in permil: ‰),

$$\delta=(R_{sample}-R_{standard})/R_{standard} \quad (4)$$

in which R is $^2H/^1H$ or $^{13}C/^{12}C$, respectively.

Data were normalized to the VSMOW/SLAP hydrogen isotopic scale by comparing with an external standard (A3 mix for samples run before August 2017; A6 mix for samples run after late July 2017) obtained from A. Schimmelmann (Indiana University) containing 15 n-alkane compounds (C_{16} to C_{30}), with δ^2H values spanning −227 to −46‰ for A3 mix and −256 to −17‰ for A6 mix; and $\delta^{13}C$ values spanning −33.37 to −28.61‰ for A3 mix and −33.97 to −26.15‰ for A6 mix. The RMS error determined by replicate measurements of the standard across the course of analyses was 3.7‰ for δ^2H and 0.21‰ $\delta^{13}C$. FAMEs were corrected for H or C of the methyl group added in

methylation by mass balance to yield the δ^2H and $\delta^{13}C$ of the corresponding fatty acid (following the methods of (Lee et al., 2017)).

Isotopic fractionations between δ_a and δ_b, as ^2H-depletion factors ($\varepsilon_{a/b}$), were calculated with the following equation:

$$\varepsilon_{a/b} = \alpha_{a/b} - 1 = [(\delta_a+1)/(\delta_b+1)] - 1 \quad (7)$$

2.4. Results

2.4.1. Plant wax abundance

We quantify *n*-alkanoic acids with carbon chain lengths of 24 (0.7 to 14.6 µg/g), 26 (1.9 to 45.7 µg/g), 28 (1.7 to 102.7 µg/g) and 30 (0.4 to 19 µg/g). Overall, the modal chain length is 28, with an ACL (average chain length) of 27 ± 0.4 (1σ, n = 67). The average CPI (carbon preference index) was 10 ± 5, indicating input from terrestrial higher plants (Pancost and Freeman, 2014). We find two main patterns in chain length abundance throughout the ~3,000-year record (**Fig. 2:4a, 2:4c**): C_{28} is the modal homolog overall, and it has a higher relative abundance ($C_{28}/\Sigma C_{24}:C_{30}$) between 2,950 to 850 cal yrs BP (mean 45%), compared to 28% in the last 850 years **(Fig. 2:4b)**.

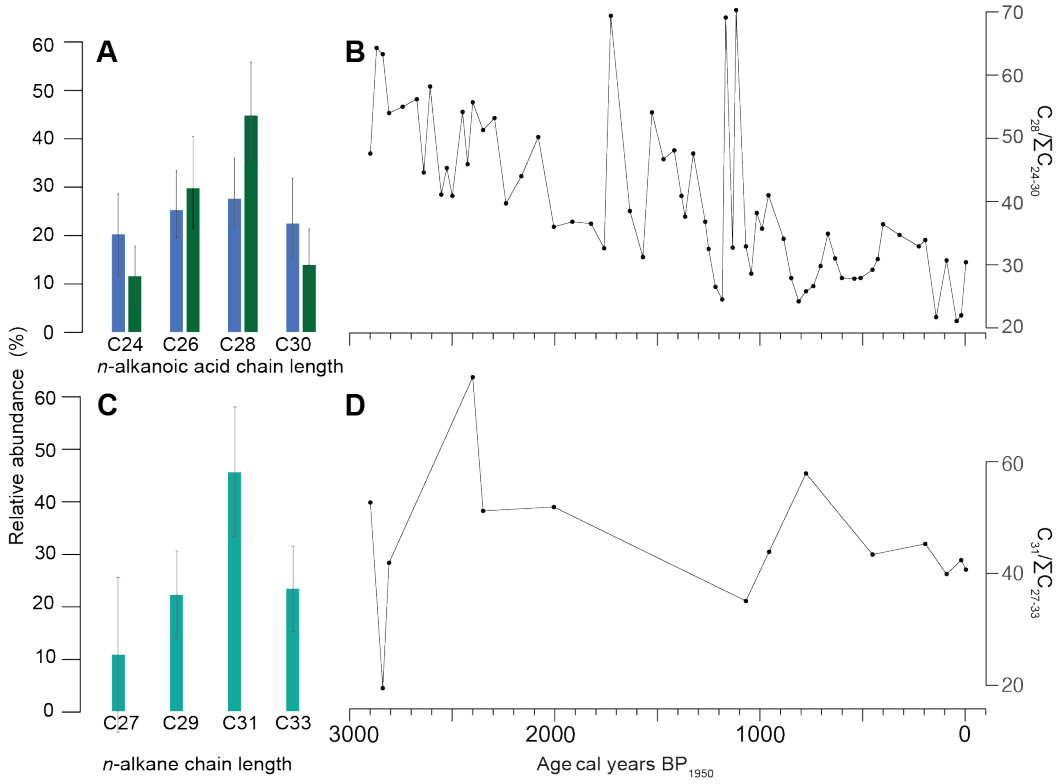

Figure 2:4: Blackwood sinkhole chain length abundance.
a) Chain length abundance of *n*-alkanoic acids, separated into two groupings (850 cal yrs BP to present, and 850–3,000 cal yrs BP, green), b) relative abundance of C_{28} n-alkanoic acid with time, c) abundance distribution of n-alkanes, and d) relative abundance of C_{31} n-alkane with time.

We quantified the C_{26} to C_{33} *n*-alkane concentrations in 14 samples at low resolution through the core. The abundance of C_{27} *n*-alkanes were 0.2 to 12 µg/g, C_{29} *n*-alkanes were 0.7 to 7.8 µg/g, C_{31} *n*-alkanes were 1.2 to 18.6 µg/g, and C_{33} *n*-alkanes were 0.5 to 8.2 µg/g (**Fig. 2:4d**). The mean ACL was 30.6 ± 0.6 (1σ, n = 14) and mean CPI was 13 ± 5 (1σ, n = 14). C_{31} is the modal chain length and abundance distributions do not differ significantly in the comparison before and after 850 cal yrs BP (**Fig. 2:4c**), but note the small sample size in the *n*-alkane dataset relative to the *n*-alkanoic acid analyses.

We found detectable taraxerol in 11 of the 17 samples screened for mangrove-derived triterpenol biomarkers (n = 17). Taraxerol concentrations range from 0.4 to 11.2 µg/g (mean = 4.1 µg/g, σ=3.8 µg/g, n =11). The proportion of mangrove biomarkers to *n*-alkanes, taraxerol/$\Sigma_{alkanes}$ (calculated for 11 samples) ranged from 0.04 to 3.08, with high values (>0.5) only after 850 cal yrs BP (**Fig. 2:6d**).

2.4.2. Hydrogen isotopes

We measured the δ^2H values of *n*-alkanoic acids, which ranged from –157 to –110‰ (mean = –136‰, 1σ=14‰, n = 29) for C_{24}, –160 to –103‰ (mean = –124‰, 1σ = 13‰, n = 55) for C_{26}, –158 to –99‰ (mean = –121‰, 1σ =16‰, n = 57) for C_{28}, and –149 to –99‰ (mean = –129‰, 1σ = 15‰, n = 28) for C_{30} through the core (**Fig. 2:5a**). The C_{28} *n*-alkanoic acid is selected to describe downcore variations as it is considered representative of inputs from long-chained terrestrial plants (Freeman and Pancost, 2014), and is abundant in tropical forests (Feakins et al., 2016a). Values of δ^2H_{28} span ~50‰ throughout the record. There is a trend from higher δ^2H_{28} values (mean = –112‰, 1σ = 9‰, maximum value = –99‰) from 2,950 to 850 cal yrs BP to lower δ^2H_{28} values starting at approximately 850 cal yrs BP (mean = –143‰, 1σ=8‰, minimum value = –158‰) (**Fig. 2:5b)**.

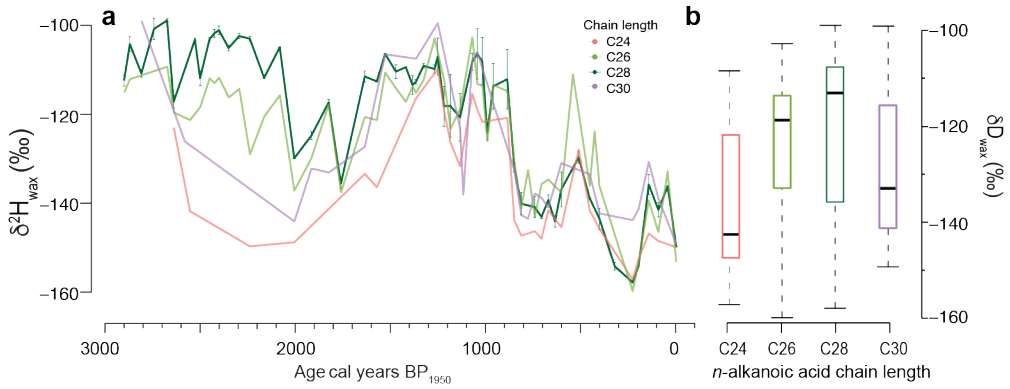

Figure 2:5: Hydrogen isotopic measurements for n-alkanoic acids. Showing a) downcore δ^2H values for the late Holocene and b) δ^2H values by chain length for the even chain length C_{24} to C_{28} n-alkanoic acids, showing median (thick line), interquartile range (box) and range (whiskers).

2.4.3. Carbon isotopes

For a subset of samples analyzed for hydrogen isotopes (**Fig. 2:6a**), $\delta^{13}C_{28}$ values were determined for 18 samples downcore (**Fig. 2:6b)**. Values of $\delta^{13}C$ for each chain length ranged from –42 to –28‰ (mean = –36‰, 1σ = 4‰) for C_{24}, –43 to –29‰ (mean = –38‰, 1σ = 4‰) for C_{26}, –45 to –30‰ (mean = –38‰, 1σ = 5‰) for C_{28}, and –45 to –30‰ (mean = –34‰, 1σ = 4‰) for C_{30}. These values are-within the expected range for C_3 angiosperms (Chikaraishi and Naraoka, 2007; Freimuth et al., 2017; Wu et al., 2017). $\delta^{13}C_{28}$ reveals little variability from 2,150 to 850 cal yrs BP (mean = –41‰, 1σ = 2‰), but $\delta^{13}C_{28}$ values are variable and more enriched from 850 cal yrs BP (mean = –35‰, 1σ = 5‰) to the present. There are two shifts to more ^{13}C-enriched values after 850 and 370 cal yrs BP, at the same time as shifts in δD_{28} (**Fig. 2:6**).

2.5. Discussion

2.5.1. Vegetation community and plant wax inputs to the sinkhole

Before interpreting the downcore variations in plant wax hydrogen isotopic composition, we must consider evidence for changing vegetation (**Fig. 2:6e-h**). Pollen spectra indicate a major change in the vegetation community after 850 cal yrs BP, as tropical hardwoods and palms (*Myrtaceae* and *Arecaceae*) are replaced by pines (*Pinus*) and mangrove taxa (*Laguncularia racemosa* and *Conocarpus erectus*) (Fall unpublished data; van Hengstum et al. 2016; Tamalavage et al., 2018). *C. erectus* and *L. racemosa* are the dominant mangrove taxa represented in the pollen record, whereas pollen from both *Rhizophora mangle* (prolific pollen producer) and *Avicennia* (poor pollen producer) (Urrego et al., 2009) is very low throughout the record. The presence of taraxerol identified within this study at low resolution might seem to suggest that *R. mangle* is present on the landscape, as taraxerol dominates the lipid composition of *R. mangle* leaves (Killops and Frewin, 1994; Versteegh et al., 2004), but pollen abundance for *R. mangle* is low and modern distributions are mostly found on muddy shores and brackish environments on the leeward sides of the islands. Alternatively, the identified sterols may derive from other mangrove species, consistent with studies of *Avicennia* and *Lagucularia* by Koch et al. (2003). Thus, the presence of triterpenols (taraxerol) corroborate pollen evidence indicating an increase in mangrove plants on the adjacent landscape after 850 cal yrs BP (**Fig. 2:6d**). $\delta^{13}C$ and C:N ratios measured on bulk organic matter deposited within the basin confirm an expansion of wetland on the adjacent karst landscape (Tamalavage et al., 2018). Within the plant wax biomarkers, we find that the C_{28} *n*-alkanoic acid relative abundance decreases from 45% to 28% at 850

cal yrs BP (**Fig. 5a**). This could indicate a change in plant wax community inputs, or a change in degradation or microbial activity (Li et al., 2018). Within this time period, plant wax $\delta^{13}C$ values increase with the appearance of pines and mangroves (**Fig. 2:6c**), which is consistent with fractionations in conifers as well as in more open habitats (Diefendorf and Freimuth, 2017).

Plant wax hydrogen isotopic compositions become more ^{2}H-depleted after 850 cal yrs BP, specifically from 850 to 600 cal yrs BP (**Fig. 2:6b**), which coincides with an increase in mangrove pollen from 890 to 680 cal yrs BP (**Fig. 2:6e**) and lower proportions of pine (**Fig. 2:6f**), with a second phase of ^{2}H-depletion from 450 to 150 cal yrs BP. The shifts to more ^{2}H-depleted values are likely dominated by the greater fractionations associated with increased salinity and mangrove plant inputs (Ladd and Sachs, 2012). The simultaneous increase in $\delta^{13}C$ values and depleted $\delta^{2}H$ values could be due to discrimination associated with decreasing stomatal conductance under increasingly saline or water-stressed conditions (Farquhar et al., 1982; Lin and Sternberg, 1992). There will be less discrimination against ^{13}C under these conditions, and resultant carbon with be enriched as the CO_2 pool within the leaf is increased in $\delta^{13}C$ (Ladd and Sachs, 2012).

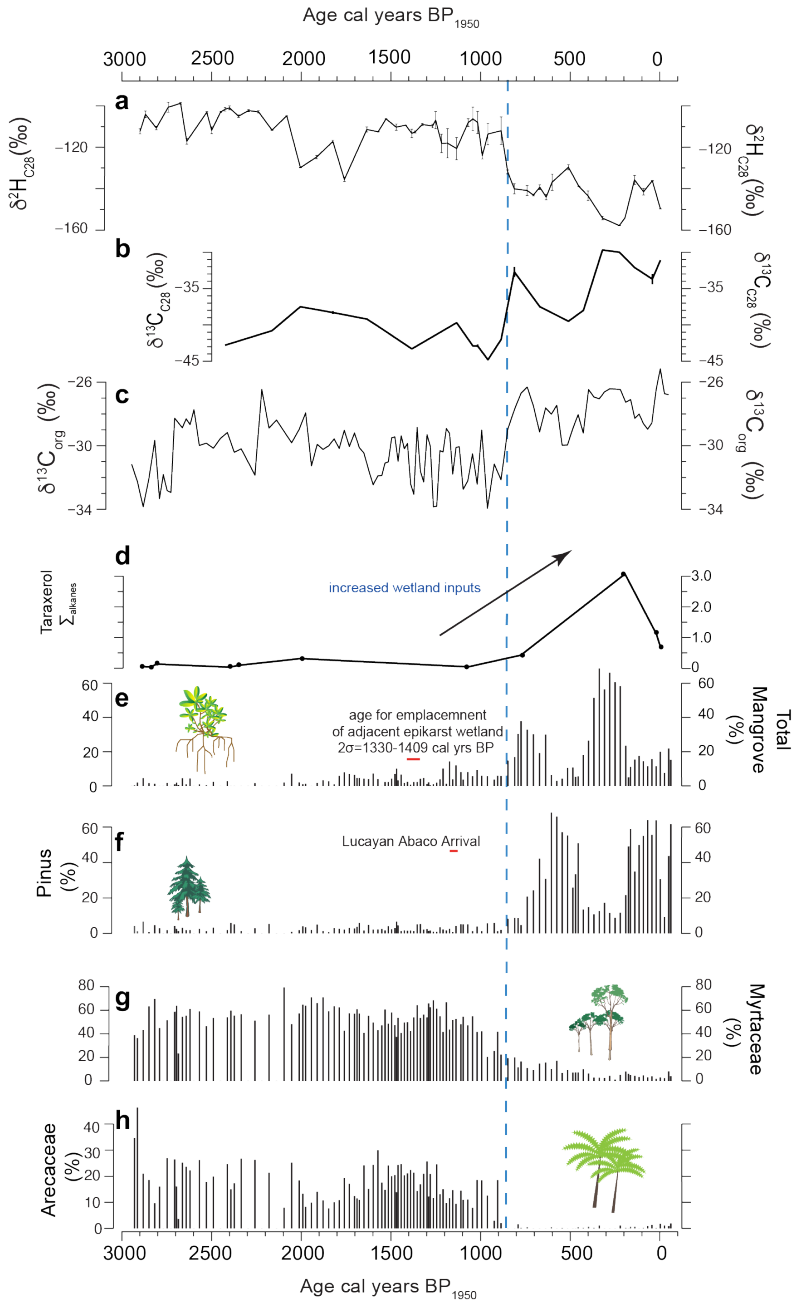

Figure 2:6: Comparison of geochemical results from BLWD-C2.
0 is 1950 CE, a) downcore δ^2H_{28} values, b) downcore $\delta^{13}C_{28}$ values, c) $\delta^{13}C_{org}$ for BLWD-C2 (Tamalavage et al., 2018) d) downcore taraxerol/$\Sigma_{alkanes}$ (e-h) Pollen results from BLWD-C2 (van Hengstum et al., 2016; Tamalavage et al., 2018; van Hengstum et al., 2018), and direct evidence of human occupation on Abaco (Steadman et al., 2007; Sullivan et al., 2020). The change in the vegetation community as detected by pollen

also marks a major transition in the plant biomarker signals at about 850 cal yrs BP (blue dashed line).

2.5.2. Correcting for mangrove inputs

Prior work has shown that the emplacement of the adjacent wetland occurred after ~1350 cal yrs BP, based on the basal age of a wetland peat core (van Hengstum et al., 2016). However, changes in the organic matter in sinkhole sediments are indicated by $\delta^{13}C$ values in the bulk organic matter only after ~1000 cal yrs BP (Tamalavage et al., 2018). Mangrove pollen first appears in abundance after 850 cal yr BP (**Fig. 2:6**), suggesting the start of the mangrove influence on plant wax records in the core.

Given the covariation between mangrove pollen and plant wax δ^2H, we attempt to correct for the influence of mangroves to extract the signal of terrestrial vegetation and thus precipitation δ^2H. Due to uneven sampling between pollen and biomarker sampling and analysis (**Appendix A, Fig. 2**), mangrove pollen and plant wax δ^2H were interpolated to evenly spaced intervals (1 cm). As triterpenols were studied at low resolution, they are used as a cross check on the pollen findings and therefore not used for the mangrove correction.

We determined an empirical relationship between δ^2H_{28} and total mangrove pollen (**Fig. 2:7a**), during the presence of mangrove (mostly >10% mangrove pollen) from 850 cal yrs BP to the present (**Fig. 2:7b**). In that interval, we found a significant negative correlation ($r = -0.77$, $p < 0.05$) (**Fig. 2:7a**), using non-parametric methods that account for serial correlation (Ebisuzaki, 1997). This correlation implies that mangrove inputs explain about 56% of the variance. If we assume the linear fit describes the

mangrove influence and that the remainder of the variance (residual) is due to terrestrial plant wax inputs primarily responding to hydrological variability (δ^2H_{precip}), then we can use the empirical regression of the linear fit to remove the mangrove influence. As measured plant waxes from 850 cal years BP to the present are comprised by both mangrove and terrestrial plant inputs, this offers a pragmatic approach to mangrove correction based on the empirical relationship over time, which incorporates the strong negative correlation and mechanistic basis for that relationship (Ladd et al., 2012). Principal uncertainties are related to inter-plant and inter-species variations in hydrogen isotope fractionations such as likely occur with species and salinity effects that are too challenging to quantify without additional data; unconstrained connections between pollen abundance and the amount of plant wax inputs from mangroves; as well as minor uncertainties related to uncertainties on analytical determinations of δ^2H values and pollen counts.

We used the mangrove pollen abundances to predict the mangrove contributed plant wax δ^2H ($\delta^2H_{m\text{-}pred}$):

$$\delta^2H_{m\text{-}pred} = \text{mangrove pollen (\%)} * (-0.3053) + (-134.77) \quad (8)$$

and we corrected the measured δ^2H_{28} values to yield the mangrove-corrected value δ^2H_{corr} (**Fig. 2:7b**), which is approximated by:

$$\delta^2H_{corr} = \delta^2H_{measured} - \text{mangrove pollen (\%)} * (-0.3053) \quad (9)$$

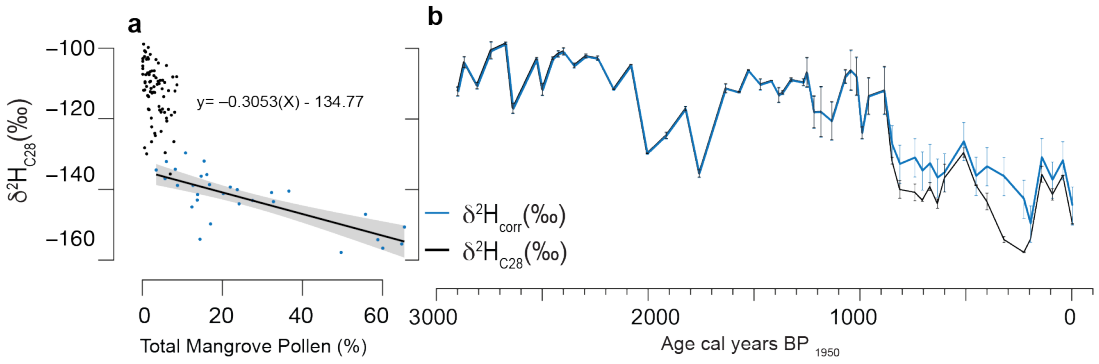

Figure 2:7: a) Mangrove pollen (*Laguncularia, Avicennia, Rhizophora, Conocarpus erectus*) versus δ^2H_{28} values downcore.
Data interpolated at 1 cm increments, b) Downcore δ^2H_{28} values measured (black line) and mangrove-corrected (blue line).

Mangrove corrected values are more enriched than measured values, especially during intervals of increased mangrove pollen (~850–680 cal yrs BP; 520–280 cal yrs BP). During those intervals, δ^2H_{corr} ranges from –136 to –126‰, compared to δ^2H_{28} of –154 to –130‰. The correction reduces the variance, with δ^2H_{corr} values for the last 850 cal yrs BP falling more closely within the measured range of δ^2H_{28} from ~3000 to 2000 cal yrs BP, when mangrove inputs were minimal. This pollen-based mangrove correction does not explicitly account for salinity, but the approach implicitly assumes that an increase in mangrove inputs corresponds to an increase in source water salinity, and uses the regression between mangrove pollen (%) and δ^2H to remove that combined mangrove and salinity effect. However, this relationship may be confounded by changes in precipitation δ^2H or changes in salinity independent of mangrove pollen flux. If we consider the increasing fractionation with increasing salinity reported in field studies elsewhere ~ –1‰/psu (Ladd and Sachs, 2012; Ladd and Sachs, 2015a; Ladd and Sachs, 2015b; He et al., 2017), the observed decline in δ^2H values is on the order of –30‰

associated with the mangrove pollen increase. This could be explained by a shift from freshwater to seawater salinities, and would suggest very little change in precipitation δ^2H as the mangroves expanded.

2.5.3. Estimating precipitation isotopic composition

Net fractionations ($\varepsilon_{28/precip}$) were calculated between the δ^2H_{28} value for the sediment closest to the core top (at 2.5 cm or +50 yrs BP, or 2000 AD) and weighted mean annual δ^2H_{precip} from the closest GNIP station in Havana, Cuba (2002-2016), in sediments that have ~20% mangrove pollen. Calculated $\varepsilon_{28/precip}$ is −139‰, which is slightly higher than global estimates of fractionation, as expected given the partial mangrove influence in this horizon. In comparison, global estimates for C_{29} n-alkanes for angiosperms are −113‰ ± 30‰ (Sachse et al., 2012), and dual compound class studies of tropical forests reporting fractionations are −129‰ ± 2‰ for C_{29} n-alkanes and −121‰ ± 3‰ for C_{28} n-alkanoic acids (Feakins et al., 2016). We use the tropical forest fractionation for C_{28} *n*-alkanoic acids for predictions of $\delta^2H_{precip\text{-}raw}$, which is thought to be appropriate for the majority of the record that is not mangrove-influenced. For the mangrove-influenced horizons, we apply the pollen-corrected approach, which results in a varying fractionation that encompasses the coretop calculated fractionation ($\varepsilon_{28/precip}$ = −134‰), and also predicts a larger fractionation for the sediments with up to 60% mangrove pollen. After correcting for mangrove inputs, we obtain estimates of $\delta^2H_{precip\text{-}corr}$ from −18.2 to +25‰ throughout the last 2,950 years (**Fig. 2:8a**).

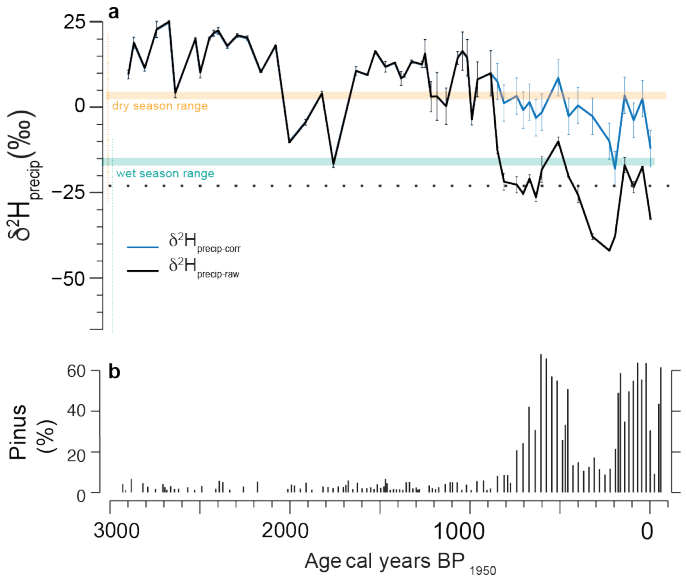

Figure 2:8: Corrected and uncorrected reconstructed δ^2H_{precip}.
a) Precipitation isotopic reconstructions based on measured plant wax ($\delta^2H_{precip\text{-}raw}$ black line) and after mangrove-correction ($\delta^2H_{precip\text{-}corr}$, blue line). Horizontal lines represent mean dry (orange) and wet (teal) season values recorded at the nearby Havana, Cuba GNIP station, b) pine pollen (van Hengstum et al., 2016).

As intended, the isotopic range of the $\delta^2H_{precip\text{-}corr}$ (58‰) is smaller than the range of the $\delta^2H_{precip\text{-}raw}$ without mangrove correction (67‰). In comparison, the Havana CPHR GNIP station has a recorded range of monthly totals from –66.3 to +20.6‰ (**Fig. 2:2**), although the mean climatological seasonality is much smaller at –15.2 to +3.5‰. Although all values in the non-mangrove corrected record are theoretically possible within a rainfall event, it would be surprising to obtain such a depleted signal in the sediments which represent multidecadal (~60 yr) averages (**Fig. 2:2b**). Therefore, the mangrove-corrected $\delta^2H_{precip\text{-}corr}$ likely better represents past rainfall variations, when mangroves are present. Although calculated values of $\delta^2H_{precip\text{-}corr}$ are plausible, the

magnitude of the variation is large and corrected values should be interpreted cautiously given the imperfect nature of the mangrove correction attempted here.

Uncertainties of measured δ^2H_{28} values include <2‰ instrument precision (1σ, sample replicates), 4‰ calibration accuracy, and uncertainties on the pollen- δ^2H_{28} regression are 5‰. Many additional uncertainties in this application cannot be readily quantified. One uncertainty derives from the different depths of pollen and biomarker samples, and resulting uncertainty in the correlation exercise. In terms of ecosystem processes, perhaps the largest of the uncertainties on $\delta^2H_{precip\text{-}corr}$ derives from the likely differences between the proportional production of pollen among the different plant species and that of their wax productivity. Another concern is additional salinity-induced fractionations within the mangroves. Our method assumes that on multi-decadal timescales, higher salinities would correspond to higher proportions of mangroves, but salinity can vary on shorter timescales, which is presently unconstrained. Uncertainty on the mean tropical forest fractionation is 3‰ (s.e.m) (Feakins et al., 2016a), however, the epsilon for this Caribbean ecosystem has not yet been determined rigorously. While it is not possible to quantify unknown uncertainties, a 10-20‰ uncertainty on the mangrove-corrected estimate is plausible.

Another concern is that the reconstructed values are more enriched than would be expected, given the observed to the seasonal cycle of rainfall and the multi-decadal averaging in sediments. This further suggests a bias and that the epsilon should likely be smaller than the coretop or tropical forest value. Fractionations as small as –93‰ have

been noted in sub-humid and semi-arid southern California (Feakins et al., 2014) and if this also applied in dry times in the Caribbean, it could shift precipitation reconstructions by up to –30‰. Alternatively, plants could have a strong growth seasonality or be accessing a lens of evaporatively-enriched water stored in the karst. Elsewhere, a similar issue of enriched reconstructions was noted by Taylor et al., (2020) in Costa Rica, where their reconstructed δ^2H_{precip} values based on n-alkanes are more enriched than the seasonal GNIP cycle, suggesting that plants were using more isotopically heavy water throughout the year, rather than summertime rainfall. These questions suggest that local calibrations of plant water isotope systematics will represent an important future development

2.5.4. Regional hydroclimate

At Blackwood Sinkhole on Abaco, the vegetation is relatively stable from 2950 to 850 cal yrs BP (**Fig. 2:6e-h)**, providing confidence in precipitation isotopic reconstructions. Generally, high δ^2H values from 2,950 to 850 cal yrs BP would imply an expanded NASH and increased local subsidence, likely accompanied by dry conditions on Abaco island (with $\delta^2H_{precip\text{-}corr}$ values similar to the dry season within the instrumental record; **Fig. 2:8a**). If we set this record in context with other reconstructions from across the Caribbean region (**Fig. 2:9**), we see some shared patterns. The dry period from 2,950 to 2,100 cal yrs BP (**Fig. 2:9a**, yellow shading) corresponds to evidence for aridity across the Caribbean between ~3,300 and 2,500 cal yrs BP (Berman and Pearsall, 2000; Fensterer et al., 2013; Gregory et al., 2015), including a speleothem record from Cuba (**Fig. 2:9b**) and low runoff from Venezuela to

the Cariaco Basin (**Fig. 2:9d**). On Abaco, a marine sapropel within No Man's Land Sinkhole similarly suggests low rainfall amounts from ~3,300 to 2,500 cal yrs BP, with increased rainfall after 2,500 cal yrs BP (van Hengstum et al., 2018), although a pollen record from nearby Andros island (Kjellmark, 1996) found drought resistant plant taxa persisting until 1,500 cal yrs BP. On Abaco, we find a shift to more depleted δ^2H_{precip} from ~2,100 to ~1,700 cal yrs BP (**Fig. 2:9a**), perhaps linked to a contracted NASH and more rainfall on Abaco (Fig. 2), which is consistent with the No Man's Land Sinkhole record (van Hengstum et al., 2018). From 1700 to 900 cal yrs BP, generally high $\delta^2H_{precip\text{-}corr}$ values (**Fig. 2:9a**, yellow shading) suggest a period of increased aridity in the Northern Caribbean. Arid conditions around 1,230 cal yrs BP may relate to onset of the "Terminal Classic Drought" documented within the Yucatan Peninsula, Mexico (Curtis et al., 1998; Hodell et al., 2005; Douglas et al., 2015) that affected Mayan city and social structures, caused agricultural abandonment in Costa Rica (Taylor et al., 2020), and disrupted smaller populations in Hispaniola (Lane et al., 2014). There are shifts in available proxy records at ~1,000 cal yrs BP documented throughout in the Caribbean, including the Cariaco Basin runoff record (**Fig. 2:9d**) linked to ITCZ migration (**Fig. 2:9e**). Yet the hydroclimate response may not be uniform across the Caribbean and thus we wish to contrast the conditions in the northern Caribbean here. Speleothem records from Northwestern Cuba suggest a sharp increase in precipitation at 1,000 cal yrs BP (Fensterer et al., 2013) (**Fig. 2:9b**) or a more gradual increase throughout the last millennium as indicated by another speleothem (Fensterer et al., 2012). In contrast, there is less rainfall-promoted runoff (Ti) recorded in a lagoon in northwestern Cuba (Gregory

et al., 2015) at this time. On Abaco, we find shifts in $\delta^2H_{precip\text{-}corr}$ after 1,100 and 900 cal yrs BP (**Fig. 2:9a**), which would suggest a contracted NASH and increased rainfall.

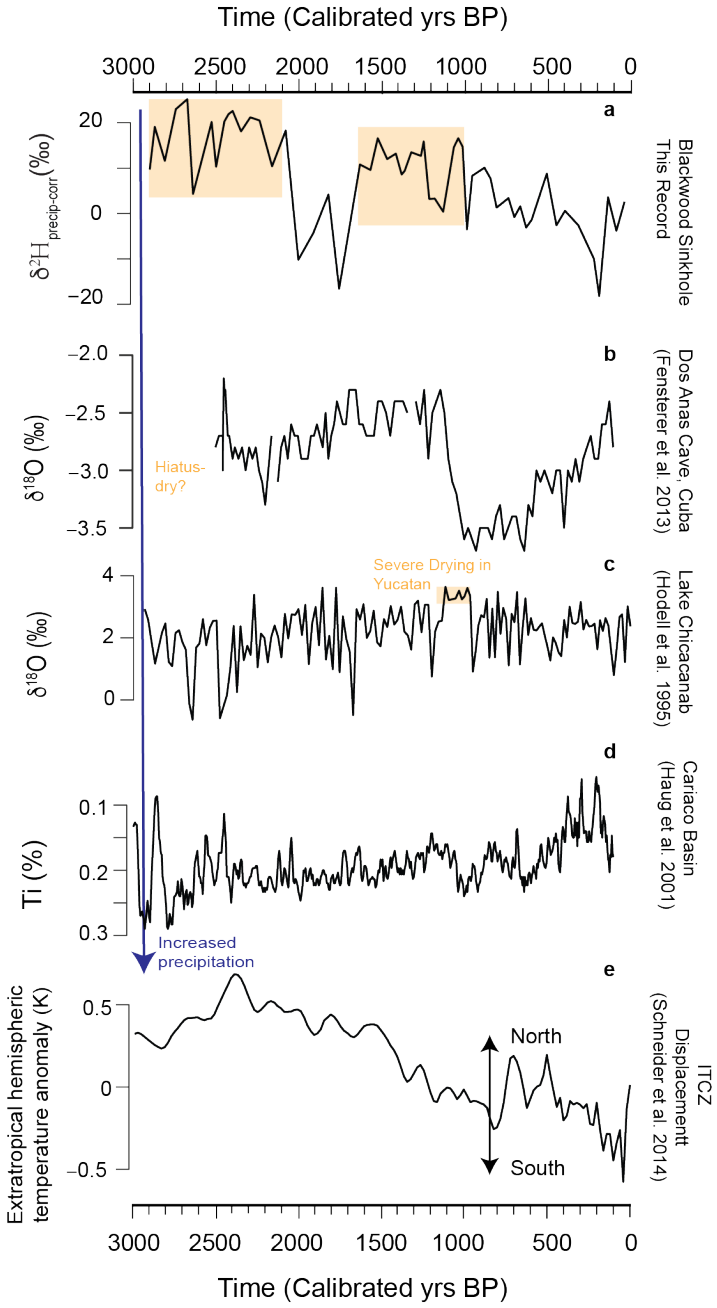

Figure 2:9: Regional paleoclimate comparison to BLWD C2.

a) reconstructed $\delta^2H_{precip\text{-}corr}$ from this study, (yellow shading denotes inferred aridity); b) $\delta^{18}O$ values from a nearby speleothem in Dos Anas Cave, Cuba (Fensterer et al., 2013), yellow bar indicates a hiatus likely due to drought; c) $\delta^{18}O$ values from the gastropod *Pyrgophorus coronatus* recorded within Lake Chichancanab, Mexico; d) Ti record of terrestrial runoff from the Cariaco Basin (Haug et al., 2001a); and e) the Northern-to Southern Hemisphere Temperature anomaly (Schneider et al., 2014) interpreted as a measure of ITCZ displacement as indicated by the arrow.

It is challenging to resolve the disagreement in the archives from the northern Caribbean at present. As the δ^2H_{28} was modified by mangrove expansion in the last 850 cal yrs BP, and potentially as early as ~1350 cal yrs BP when wetlands first colonized depressions and deposited peat on the adjacent epikarst surface, caution must be used in interpreting δ^2H_{28} from a hydroclimate perspective. At ~700 cal yrs BP, lower $\delta^2H_{precip\text{-}corr}$ values are found to be synchronous with increased pine on the landscape, which perhaps indicates a contracted NASH during the Little Ice Age and broadly wetter climate (**Fig. 8**). However, even after accounting for the mangrove bias, $\delta^2H_{precip\text{-}corr}$ show ^2H-depleted values that may indicate an under-correction of the mangrove influence rather than hydroclimate shifts.

2.6. Conclusions

Plant wax hydrogen isotopic evidence for past precipitation is modulated by mangrove inputs in a 3,000-year sedimentary record from Blackwood Sinkhole, Abaco Island, Bahamas. A prominent increase in mangroves in the last 850 years (van Hengstum et al. 2016; Tamalavage et al., 2018) appears to contribute plant wax *n*-alkyl lipids that are ^2H-depleted, consistent with studies on the effects of salinity on hydrogen

isotopic fractionation (Ladd et al., 2012). Mangrove presence is readily detected by mangrove specific proxies (pollen, and the mangrove biomarker taraxerol), and changing inputs also modulate the plant wax proxies (plant wax *n*-alkanoic acid and *n*-alkane abundance, as well as $\delta^{13}C_{28}$ and $\delta^{2}H_{28}$). Using the pollen record, we accounted for the vegetation changes and generated a mangrove-corrected plant wax record that can be interpreted cautiously as a reconstruction of past precipitation isotopes. Mangrove-corrected precipitation $\delta^{2}H$ reconstructions from Blackwood sinkhole suggest centennial-scale variability in hydroclimate in the Caribbean. Periods of more ^{2}H-enriched values from 2,950 to 2,100 cal yrs BP and 1,700 to 1,000 cal yrs BP suggest an expanded NASH and likely more arid conditions over much of the Caribbean. Depletion of ^{2}H from 2,100 to 1,800 cal yrs BP, and from 850 cal yrs BP to the present may correspond to a contracted NASH, with more local convection and thus wetter conditions on Abaco, consistent with interpretations from another record on Abaco from No Man's Sinkhole. In the last 850 years pollen assemblages indicate that mangroves compromise the plant wax proxy in Blackwood Sinkhole, modulating the record with ^{2}H-depletion that corresponds to increased mangrove inputs. In this mangrove-influenced interval, the plant wax hydrogen isotopic evidence for precipitation is compromised. Our pollen correction allows for the removal of this bias and suggests a range of precipitation isotopic composition and variability that is consistent with expected atmospheric dynamics and distillation patterns. We suggest that pollen and plant wax provide an invaluable pairing to identify, evaluate and address mangrove

influence on the plant wax hydrogen isotope proxy in similar tropical, coastal sinkhole settings

2.7. References

Berman, M.J., Pearsall, D.M., 2000. Plants, people, and culture in the prehistoric central Bahamas: A view from the Three Dog Site, an early Lucayan settlement on San Salvador Island, Bahamas. Latin American Antiquity 11, 219-239.

Bhattacharya, T., Coats, S., 2020. Atlantic-Pacific gradients drive Last Millennium hydroclimate variability in Mesoamerica. Geophysical Research Letters, e2020GL088061.

Bhattacharya, T., Tierney, J.E., DiNezio, P., 2017. Glacial reduction of the North American Monsoon via surface cooling and atmospheric ventilation. Geophysical Research Letters 44, 5113-5122.

Brady, E., Stevenson, S., Bailey, D., Liu, Z., Noone, D., Nusbaumer, J., Otto-Bliesner, B.L., Tabor, C., Tomas, R., Wong, T., 2019. The connected isotopic water cycle in the Community Earth System Model version 1. Journal of Advances in Modeling Earth Systems 11, 2547-2566.

Chikaraishi, Y., Naraoka, H., 2007. δ13C and δD relationships among three n-alkyl compound classes (n-alkanoic acid, n-alkane and n-alkanol) of terrestrial higher plants. Organic Geochemistry 38, 198-215.

Curtis, J.H., Brenner, M., Hodell, D.A., Balser, R.A., Islebe, G.A., Hooghiemstra, H., 1998. A multi-proxy study of Holocene environmental change in the Maya Lowlands of Peten, Guatemala. Journal of Paleolimnology 19, 139-159.

Diefendorf, A.F., Freimuth, E.J., 2017. Extracting the most from terrestrial plant-derived n-alkyl lipids and their carbon isotopes from the sedimentary record: A review. Organic Geochemistry 103, 1-21.

Douglas, P.M., Pagani, M., Brenner, M., Hodell, D.A., Curtis, J.H., 2012. Aridity and vegetation composition are important determinants of leaf-wax δD values in

southeastern Mexico and Central America. Geochimica et Cosmochimica Acta 97, 24-45.

Douglas, P.M., Pagani, M., Canuto, M.A., Brenner, M., Hodell, D.A., Eglinton, T.I., Curtis, J.H., 2015. Drought, agricultural adaptation, and sociopolitical collapse in the Maya Lowlands. Proceedings of the National Academy of Sciences 112, 5607-5612.

Ebisuzaki, W., 1997. A method to estimate the statistical significance of a correlation when the data are serially correlated. Journal of Climate 10, 2147-2153.

Feakins, S.J., 2013. Pollen-corrected leaf wax D/H reconstructions of northeast African hydrological changes during the late Miocene. Palaeogeography, Palaeoclimatology, Palaeoecology 374, 62-71.

Feakins, S.J., Bentley, L.P., Salinas, N., Shenkin, A., Blonder, B., Goldsmith, G.R., Ponton, C., Arvin, L.J., Wu, M.S., Peters, T., West, A.J., Martin, R.E., Enquist, B.J., Asner, G.P., Malhi, Y., 2016. Plant leaf wax biomarkers capture gradients in hydrogen isotopes of precipitation from the Andes and Amazon. Geochimica et Cosmochimica Acta 182, 155-172.

Feakins, S.J., Bentley, L.P., Salinas, N., Shenkin, A., Blonder, B., Goldsmith, G.R., Ponton, C., Arvin, L.J., Wu, M.S., Peters, T., West, A.J., Martin, R.E., Enquist, B.J., Asner, G.P., Malhi, Y., 2016a. Plant leaf wax biomarkers capture gradients in hydrogen isotopes of precipitation from the Andes and Amazon. Geochimica et Cosmochimica Acta 182, 155-172.

Feakins, S.J., Sessions, A.L., 2010a. Controls on the D/H ratios of plant leaf waxes in an arid ecosystem. Geochimica et Cosmochimica Acta 74, 2128-2141.

Feakins, S.J., Sessions, A.L., 2010b. Crassulacean acid metabolism influences D/H ratio of leaf wax in succulent plants. Organic Geochemistry 41, 1269-1276.

Feakins, S.J., Wu, M.S., Ponton, C., Tierney, J.E., 2019. Biomarkers reveal abrupt switches in hydroclimate during the last glacial in southern California. Earth and Planetary Science Letters 515, 164-172.

Fensterer, C., Scholz, D., Hoffmann, D., Spotl, C., Pajon, J.M., Mangini, A., 2012. Cuban stalagmite suggests relationship between Caribbean precipitation and the Atlantic Multidecadal Oscillation during the past 1.3 ka. The Holocene 22, 1405-1412.

Fensterer, C., Scholz, D., Hoffmann, D.L., Spötl, C., Schröder-Ritzrau, A., Horn, C., Pajón, J.M., Mangini, A., 2013. Millennial-scale climate variability during the last 12.5ka recorded in a Caribbean speleothem. Earth and Planetary Science Letters 361, 143-151.

Fornace, K.L., Hughen, K.A., Shanahan, T.M., Fritz, S.C., Baker, P.A., Sylva, S.P., 2014. A 60,000-year record of hydrologic variability in the Central Andes from the hydrogen isotopic composition of leaf waxes in Lake Titicaca sediments. Earth and Planetary Science Letters 408, 263-271.

Fornace, K.L., Whitney, B.S., Galy, V., Hughen, K.A., Mayle, F.E., 2016. Late Quaternary environmental change in the interior South American tropics: new insight from leaf wax stable isotopes. Earth and Planetary Science Letters 438, 75-85.

Freeman, K.H., Pancost, R., 2014. Biomarkers for Terrestrial Plants and Climate. ElSevier. Report.

Freimuth, E.J., Diefendorf, A.F., Lowell, T.V., 2017. Hydrogen isotopes of n-alkanes and n-alkanoic acids as tracers of precipitation in a temperate forest and implications for paleorecords. Geochimica et Cosmochimica Acta 206, 166-183.

Fritz, S.C., Björck, S., Rigsby, C.A., Baker, P.A., Calder-Church, A., Conley, D.J., 2011. Caribbean hydrological variability during the Holocene as reconstructed from crater lakes on the island of Grenada. Journal of Quaternary Science 26, 829-838.

Gamble, D.W., Curtis, S., 2008. Caribbean precipitation: review, model and prospect. Progress in Physical Geography 32, 265-276.

Gao, L., Guimond, J., Thomas, E., Huang, Y., 2015. Major trends in leaf wax abundance, δ2H and δ13C values along leaf venation in five species of C3 plants: physiological and geochemical implications. Organic geochemistry 78, 144-152.

Gregory, B.R.B., Peros, M., Reinhardt, E.G., Donnelly, J.P., 2015. Middle-late Holocene Caribbean aridity inferred from foraminifera and elemental data in sediment cores from two Cuban lagoons. Palaeogeography, Palaeoclimatology, Palaeoecology 426, 229-241.

Hasanean, H., 2004. Variability of the North Atlantic subtropical high and associations with tropical sea-surface temperature. International Journal of Climatology: A Journal of the Royal Meteorological Society 24, 945-957.

Haug, G.H., Günther, D., Peterson, L.C., Sigman, D.M., Hughen, K.A., Aeschlimann, B., 2003. Climate and the collapse of Maya civilization. Science 299, 1731-1735.

Haug, G.H., Hughen, K.A., Sigman, D.M., Peterson, L.C., Rohhl, U., 2001a. Southward migration of the intertropical convergence zone through the Holocene. Science 293, 1304-1308.

Haug, G.H., Hughen, K.A., Sigman, D.M., Peterson, L.C., Röhl, U., 2001b. Southward migration of the intertropical convergence zone through the Holocene. Science 293, 1304-1308.

He, D., Ladd, S.N., Sachs, J.P., Jaffé, R., 2017. Inverse relationship between salinity and 2H/1H fractionation in leaf wax n-alkanes from Florida mangroves. Organic Geochemistry 110, 1-12.

Herrera, D.A., Ault, T.R., Fasullo, J.T., Coats, S.J., Carrillo, C.M., Cook, B.I., Williams, A.P., 2018. Exacerbation of the 2013–2016 Pan-Caribbean Drought by Anthropogenic Warming. Geophysical research letters 45, 10,619-610,626.

Hodell, D.A., Brenner, M., Curtis, J.H., 2005. Terminal Classic drought in the northern Maya lowlands inferred from multiple sediment cores in Lake Chichancanab (Mexico). Quaternary Science Reviews 24, 1413-1427.

Hodell, D.A., Curtis, J.H., Jones, G.A., Higuera-Gundy, A., Brenner, M., Binford, M.W., Dorsey, K.T., 1991. Reconstruction of Caribbean climate change over the past 10,500 years. Nature 352, 790.

Horn, S.P., Sanford Jr, R.L., 1992. Holocene fires in costa rica. Biotropica, 354-361.

IAEA/WMO, 2019. Global Network of Isotopes in Precipitation. The GNIP Database.

Jury, M., Malmgren, B.A., Winter, A., 2007. Subregional precipitation climate of the Caribbean and relationships with ENSO and NAO. Journal of Geophysical Research: Atmospheres 112.

Kahmen, A., Schefuß, E., Sachse, D., 2013. Leaf water deuterium enrichment shapes leaf wax n-alkane δD values of angiosperm plants I: Experimental evidence and mechanistic insights. Geochimica et Cosmochimica Acta 111, 39-49.

Karnauskas, K.B., Donnelly, J.P., Anchukaitis, K.J., 2016. Future freshwater stress for island populations. Nature Climate Change.

Karnauskas, K.B., Schleussner, C.-F., Donnelly, J.P., Anchukaitis, K.J., 2018. Freshwater stress on small island developing states: population projections and aridity changes at 1.5 and 2 C. Regional environmental change 18, 2273-2282.

Killops, S., Frewin, N., 1994. Triterpenoid diagenesis and cuticular preservation. Organic Geochemistry 21, 1193-1209.

Kjellmark, E., 1996. Late Holocene climate change and human disturbance on Andros Island, Bahamas. Journal of Paleolimnology 15, 133-145.

Koch, B., Rullkötter, J., Lara, R., 2003. Evaluation of triterpenols and sterols as organic matter biomarkers in a mangrove ecosystem in northern Brazil. Wetlands Ecology and management 11, 257-263.

Ladd, S.N., Sachs, J.P., 2012. Inverse relationship between salinity and n-alkane δD values in the mangrove Avicennia marina. Organic Geochemistry 48, 25-36.

Ladd, S.N., Sachs, J.P., 2015a. Hydrogen isotope response to changing salinity and rainfall in Australian mangroves. Plant Cell Environ 38, 2674-2687.

Ladd, S.N., Sachs, J.P., 2015b. Influence of salinity on hydrogen isotope fractionation in Rhizophora mangroves from Micronesia. Geochimica et Cosmochimica Acta 168, 206-221.

Lane, C.S., Horn, S.P., 2013. Terrestrially derived n-alkane δD evidence of shifting Holocene paleohydrology in highland Costa Rica. Arctic, antarctic, and alpine research 45, 342-349.

Lane, C.S., Horn, S.P., Kerr, M.T., 2014. Beyond the Mayan lowlands: impacts of the terminal classic drought in the Caribbean Antilles. Quaternary Science Reviews 86, 89-98.

Lane, C.S., Horn, S.P., Mora, C.I., Orvis, K.H., 2009. Late-Holocene paleoenvironmental change at mid-elevation on the Caribbean slope of the Cordillera Central, Dominican Republic: a multi-site, multi-proxy analysis. Quaternary Science Reviews 28, 2239-2260.

Lane, C.S., Horn, S.P., Taylor, Z.P., Kerr, M.T., 2016. Correlation of bulk sedimentary and compound-specific δ13C values indicates minimal pre-aging of n-alkanes in a small tropical watershed. Quaternary Science Reviews 145, 238-242.

Lee, H., Feakins, S.J., Lu, Z., Schimmelmann, A., Sessions, A.L., Tierney, J.E., Williams, T.J., 2017. Comparison of three methods for the methylation of aliphatic and aromatic compounds. Rapid Communications in Mass Spectrometry 31, 1633-1640.

Lee, J.-E., Johnson, K., Fung, I., 2009. Precipitation over South America during the Last Glacial Maximum: An analysis of the "amount effect" with a water isotope-enabled general circulation model. Geophysical Research Letters 36.

Li, G., Li, L., Tarozo, R., Longo, W.M., Wang, K.J., Dong, H., Huang, Y., 2018. Microbial production of long-chain n-alkanes: Implication for interpreting sedimentary leaf wax signals. Organic Geochemistry 115, 24-31.

Li, L., Li, W., Kushnir, Y., 2012. Variation of the North Atlantic subtropical high western ridge and its implication to Southeastern US summer precipitation. Climate Dynamics 39, 1401-1412.

Li, W., Li, L., Fu, R., Deng, Y., Wang, H., 2011. Changes to the North Atlantic subtropical high and its role in the intensification of summer rainfall variability in the southeastern United States. Journal of Climate 24, 1499-1506.

Lin, L., Gettelman, A., Feng, S., Fu, Q., 2015. Simulated climatology and evolution of aridity in the 21st century. Journal of Geophysical Research: Atmospheres 120, 5795-5815.

Liu, W., Yang, H., 2008. Multiple controls for the variability of hydrogen isotopic compositions in higher plant n-alkanes from modern ecosystems. Global Change Biology 14, 2166-2177.

Malaizé, B., Bertran, P., Carbonel, P., Bonnissent, D., Charlier, K., Galop, D., Imbert, D., Serrand, N., Stouvenot, C., Pujol, C., 2011. Hurricanes and climate in the Caribbean during the past 3700 years BP. The Holocene 21, 911-924.

Martin, E.R., Schumacher, C., 2011. Modulation of Caribbean precipitation by the Madden–Julian oscillation. Journal of Climate 24, 813-824.

Martinez, C., Goddard, L., Kushnir, Y., Ting, M., 2019. Seasonal climatology and dynamical mechanisms of rainfall in the Caribbean. Climate dynamics 53, 825-846.

Nelson, D.B., Sachs, J.P., 2016. Galapagos hydroclimate of the Common Era from paired microalgal and mangrove biomarker 2H/1H values. Proc Natl Acad Sci U S A 113, 3476-3481.

Nelson, D.M., Henderson, A.K., Huang, Y., Hu, F.S., 2013. Influence of terrestrial vegetation on leaf wax δD of Holocene lake sediments. Organic geochemistry 56, 106-110.

Park, J.W., Ladd, S.N., Sachs, J.P., 2019. Hydrogen and carbon isotope responses to salinity in greenhouse-cultivated mangroves. Organic Geochemistry 132, 23-36.

Sachse, D., Billault, I., Bowen, G.J., Chikaraishi, Y., Dawson, T.E., Feakins, S.J., Freeman, K.H., Magill, C.R., McInerney, F.A., Van Der Meer, M.T., 2012. Molecular paleohydrology: interpreting the hydrogen-isotopic composition of lipid biomarkers from photosynthesizing organisms. Annual Review of Earth and Planetary Sciences 40, 221-249.

Sarkar, S., Prasad, S., Wilkes, H., Riedel, N., Stebich, M., Basavaiah, N., Sachse, D., 2015. Monsoon source shifts during the drying mid-Holocene: Biomarker isotope based

evidence from the core ‘monsoon zone’(CMZ) of India. Quaternary Science Reviews 123, 144-157.

Schefuß, E., Schouten, S., Schneider, R.R., 2005. Climatic controls on central African hydrology during the past 20,000 years. Nature 437, 1003.

Schneider, T., Bischoff, T., Haug, G.H., 2014. Migrations and dynamics of the intertropical convergence zone. Nature 513, 45-53.

Sessions, A., TW, B., A, S., Hayes, J., 1999. Fractionation of hydrogen isotopes in lipid biosynthesis. Organic Geochemistry 30, 1193-1200.

Slayton, I.A., 2010. A vegetation history from Emerald Pond, Great Abaco Island, the Bahamas, based on pollen analysis.

Smith, F.A., Freeman, K.H., 2006. Influence of physiology and climate on δD of leaf wax n-alkanes from C3 and C4 grasses. Geochimica et Cosmochimica Acta 70, 1172-1187.

Steadman, D.W., Franz, R., Morgan, G., Albury, N.A., Kakuk, B., Broad, K., Franz, S.E., Tinker, K., Pateman, M.P., Lott, T.A., Jarzen, D.M., Dilcher, D.L., 2007. Exceptionally well preserved late Quaternary plant and vertebrate fossils from a blue hole on Abaco, The Bahamas. Proceedings of the National Academy of the Sciences 104, 19897-19902.

Sullivan, R.M., van Hengstum, P.J., Donnelly, J.P., Winkler, T., Mark, S.E., Albury, N., 2020. Absolute and relative dating of human remains in a Bahamian sinkhole (Great Cistern, Abaco). Journal of Archaeological Science: Reports.

Tamalavage, A.E., van Hengstum, P.J., Louchouarn, P., Molodtsov, S., Kaiser, K., Donnelly, J.P., Albury, N.A., Fall, P.L., 2018. Organic matter sources and lateral sedimentation in a Bahamian karst basin (sinkhole) over the late Holocene: Influence of local vegetation and climate. Palaeogeography, Palaeoclimatology, Palaeoecology 506, 70-83.

Taylor, Z.P., Lane, C.S., Horn, S.P., 2020. A 3600-year record of drought in southern Pacific Costa Rica. Quaternary Research, 1-13.

Tierney, J.E.R., James M.; Huang, Yongsong; Sinninghe Damste, Jaap S., Hopmans, Ellen C.; Cohen, Andrew S., 2008. Northern Hemisphere Controls on Tropical Southeast African Climate During the Past 60,000 Years. Science 322.

Tipple, B.J., Berke, M.A., Doman, C.E., Khachaturyan, S., Ehleringer, J.R., 2013. Leaf-wax n-alkanes record the plant–water environment at leaf flush. Proceedings of the National Academy of Sciences 110, 2659-2664.

Urrego, L.E., Bernal, G., Polanía, J., 2009. Comparison of pollen distribution patterns in surface sediments of a Colombian Caribbean mangrove with geomorphology and vegetation. Review of Palaeobotany and Palynology 156, 358-375.

van Hengstum, P.J., Donnelly, J.P., Fall, P.L., Toomey, M.R., Albury, N.A., Kakuk, B., 2016. The intertropical convergence zone modulates intense hurricane strikes on the western North Atlantic margin. Scientific Reports 6, 1-10.

van Hengstum, P.J., Maale, G., Donnelly, J.P., Albury, N.A., Onac, B.P., Sullivan, R.M., Winkler, T.S., Tamalavage, A.E., MacDonald, D., 2018. Drought in the northern Bahamas from 3300 to 2500 years ago. Quaternary Science Reviews 186, 169-185.

Versteegh, G.J., Schefuß, E., Dupont, L., Marret, F., Damsté, J.S.S., Jansen, J.F., 2004. Taraxerol and Rhizophora pollen as proxies for tracking past mangrove ecosystems. Geochimica et Cosmochimica Acta 68, 411-422.

Wu, M.S., Feakins, S.J., Martin, R.E., Shenkin, A., Bentley, L.P., Blonder, B., Salinas, N., Asner, G.P., Malhi, Y., 2017. Altitude effect on leaf wax carbon isotopic composition in humid tropical forests. Geochimica et Cosmochimica Acta 206, 1-17.

3. PALEOLIMNOLOGY OF A SINKHOLE LAKE IN THE NORTHERN BAHAMAS AND EVIDENCE FOR HYDROCLIMATE VARIABILITY DURING THE MIDDLE HOLOCENE

3.1. Introduction

On carbonate landscapes and platforms, the stratigraphy, geochemistry and long-term environmental proxies preserved in sinkhole and karst lakes can provide insight regional hydroclimate and landscape dynamics (Hatcher et al., 1982; Teeter, 1989; Grimm et al., 1993; Kjellmark, 1996; Park Boush et al., 2014; Gregory, 2016; Peros et al., 2017), complementing the geochemical proxies recorded in speleothems, which are also common on karst landscapes. Sedimentary records from sinkhole lakes have been used to reconstruct hurricane strikes (Donnelly and Woodruff, 2007; Lane et al., 2011; van Hengstum et al., 2016; Wallace et al., 2019; Winkler et al., 2020), landscape and ecological shifts (Steadman et al., 2007; Slayton, 2010; Steadman et al., 2014), environmental conditions (Tamalavage et al., 2018; van Hengstum et al., 2018; van Hengstum et al., 2020), and regional hydroclimate history (Tamalavage et al., 2020) on Holocene timescales. Sediment within sinkhole lakes (including blue holes and cenotes) is primarily sourced from carbonate particles and organic matter fragments from the adjacent karst landscape, autogenic calcium carbonate generation, and *in situ* production of organic matter. But, there are site specific physical, chemical and biologic controls on sedimentology (e.g., variations in primary productivity, water level, proximity to shoreline) that impact preserved stratigraphy (van Hengstum et al., 2020). Constraining the sedimentary processes operating within coastal sinkholes can improve application of

these records to investigate past climate change, which in turn can help inform mitigation strategies for 21st century environmental stressors such as drought (Herrera et al., 2018) and freshwater security (Karnauskas et al., 2018; Spellman et al., 2021).

Coastal sinkholes are hydrographically open systems (Smart et al., 2006), and the vertical migration of the connected coastal aquifer, driven by changes in relative sea level, controls accommodation space in the basin. This provides a unique opportunity to resolve coastal sinkhole dynamics, influenced by both a connection to the coastal ocean and carbonate lake-like geomorphology. During a transgressive sea level cycle, development within these coastal basins can be divided into the following phases: 1) initial collapse of the antecedent carbonate into an open pit with carbonate rubble at the base, 2) vertical migration of the coastal aquifer forced by sea level, which often promotes enough water depth for colonization of marsh vegetation and subsequent deposition of peat, 3) continued migration of the coastal aquifer, leading to lake-like conditions and the establishment of three stratified water layers (meteoric lens, mixing zone and anoxic saline groundwater) promoting deposition of organic rich sapropel, or palustrine to lacustrine marl (Surić et al., 2005; Gabriel et al., 2009; van Hengstum et al., 2011; Gregory, 2016; van Hengstum et al., 2020). Subtidal blue holes form as continued sea level rise eventually submerges a coastal sinkhole (Shinn et al., 1996; Gregory, 2016). Aquatic conditions (e.g., water level, salinity) within those basins can change relative to precipitation delivery to the aquifer or coastal recharge (Beddows et al., 2007), and can impact (through associated biologic activity and evaporative forcing) sediment type preserved (van Hengstum et al., 2010).

Here we examine the paleolimnology of Emerald Pond, and the geochemical (leaf wax) proxies archived in its stratigraphic record during the middle to late Holocene interval. Motivation for this study was driven by the positioning of Emerald Pond on the Little Bahama Bank in the North Atlantic Ocean, where rainfall is sensitive to western boundary displacements of the North Atlantic Subtropical High (Li et al., 2012). Previous work has also documented evidence that Emerald Pond has a continuous stratigraphic record beginning from ~8300 years ago (Slayton, 2010), and continuous sediment records like this are rare for the Bahamian archipelago. The sedimentary record in Emerald Pond preserves evidence of regional sea level position at ~8300 Cal yrs BP in response to rising local groundwater level from deglacial eustatic sea-level rise. Thereafter, the preserved stratigraphy provides evidence for both internal environmental changes, and regional hydroclimate conditions from ~8300 to 1300 cal yr BP.

3.2. Study Site

Emerald Pond (EMLD) is a shallow (<4 m) groundwater-fed sinkhole that is located approximately 1.8 km inland from the eastern shoreline of Great Abaco Island. Great Abaco Island is a part of the Little Bahama Bank (LBB, 26.79 °N, 77.42 °W; **Fig. 3:1**), which is the northern most carbonate platform in the Bahamian Archipelago (Carew and Mylroie, 1997; Walker et al., 2008). Only in the last ~700 years have pine trees (*Pinus caribaea* var. bahamensis) dominated the landscape on Abaco Island (Slayton, 2006; Fall et al., 2021), and prior to this the landscape was dominated by tropical hardwoods and palms. The Little Bahama Bank is one of the many Bahamian

carbonate islands and shallow water banks that cover 300,000 km^2 in the North Atlantic (Carew and Mylroie, 1997). Sinkholes and other karst features are ubiquitous on the Bahamian landscape, which have developed from carbonate dissolution throughout at least the Quaternary (Mylroie, 1995; Whitaker and Smart, 1997). EMLD is ~26 m in diameter with an ~4 m cliff between the subaerial surface and water table of the local coastal aquifer flooding the sinkhole (**Fig. 3:1d**), and the site is currently surrounded by a forest of Bahamian pine (*Pinus caribaea* var. bahamensis), tropical hardwoods (e.g., *Metopium*), palms, and ferns and shrubs (Slayton, 2007). The water table from the local coastal aquifer that is flooding EMLD vertically varies in response to the local ~1 m tidal range (Reeder and Rankey, 2009), which is common in unconfined karst aquifers (Beddows et al., 2007; Martin et al., 2012; Little and van Hengstum, 2019). There are currently no significant quantities of aquatic macrophytes like *Chara* currently growing in the sinkhole, but algae cover the base. There is little bathymetric variability, but close to the walls the depth to the sediment-water interface increases. There are no significant cave passages extending into the phreatic zone that are presently exposed on vertical limestone walls of the sinkhole, but there is some limestone (2-3 m) overhang on one side of the periphery.

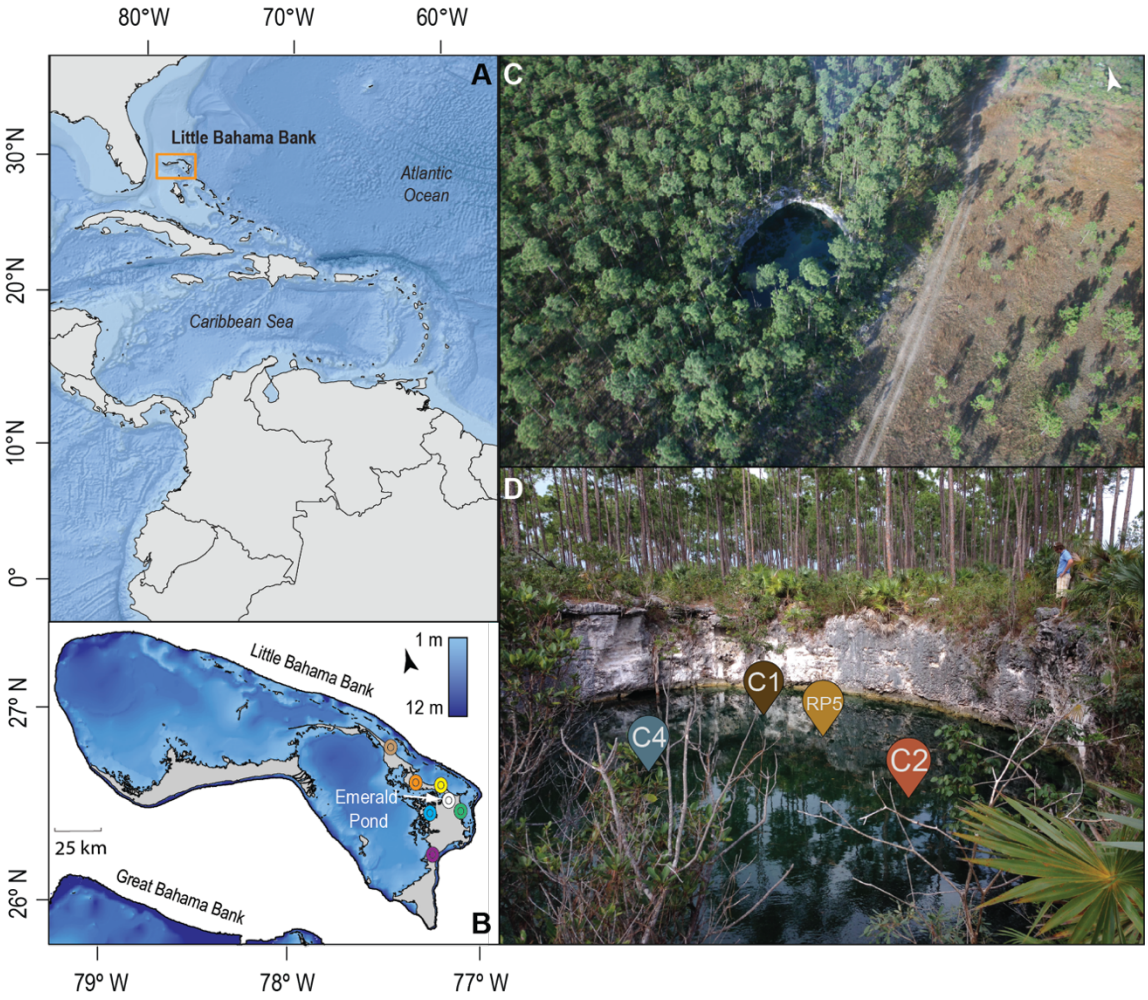

Figure 3:1: Map of Emerald Pond**.**
A) Tropical North Atlantic with the little Bahama bank outlined in orange, B) scaled in photo of the Little Bahama bank, with Emerald Pond sinkhole shown in white, plus other sinkhole basins on Abaco with paleoenvironmental records including: Blackwood (brown), No Man's Land (orange), Great Cistern (yellow), Runway (green), Freshwater River (blue), and Sawmill Sink (purple), c) aerial photo of Emerald Pond (Nancy Albury), d) Landscape-level photo of Emerald pond (Nancy Albury) with coring locations marked.

As there is no long term rainfall record on Abaco, we use regional analysis for rainfall compiled from Western Cuba and the northern Bahamas (Zone 1) within (Jury et al., 2007). Mean Annual Rainfall (MAR) in that zone is on average ~ 1470 mm

annually, with 75% of the rain occurring in the wet season from May to October (~195 mm/month, **Fig. 3:2**), and a dry season from November to April (~50 mm/month). The closest station with measured rainfall isotopic data is Centro de Proteccion e Higiene de la Radiacion (CPHR), Havana in Cuba, which falls in the same regional precipitation zone as Abaco (Jury et al., 2007), recording a similar seasonality and MAP (**Fig. 3:2**). Weighted mean annual δ^2H is –11.8‰ (wet season mean δ^2H –15.2‰, dry season mean δ^2H –3.5‰) measured at CPHR. Multiple, large scale ocean and atmospheric factors impact rainfall variability in the northern IAS, including meridional shifts in the Intertropical Convergence Zone (ITCZ), pressure and geographic changes to the intensity and extent of the North Atlantic Subtropical High (NASH), sea-surface temperature (SST) anomalies in the Atlantic warm pool, and the El Niño Southern Oscillation (ENSO) (Gamble and Curtis, 2008) (Hastenrath, 1976; Giannini et al., 2000; Wang et al., 2006; Li et al., 2012; Martinez et al., 2019). Additionally, changes in MAR can be associated with impacts from the Caribbean Low-Level Jet, local divergence, vertical wind shear on atmospheric convection (Magaña, 2005; Jury et al., 2007; Martin and Schumacher, 2011). Yet, Abaco rainfall is highly sensitive to seasonal variability of the strength (central pressure) and geographic positioning (westward margin) of the NASH (Li et al., 2011; Li et al., 2012), due to its positioning in the North Atlantic.

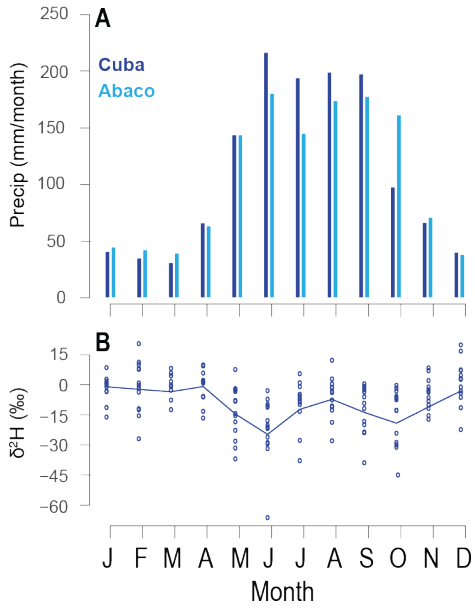

Figure 3:2: Monthly northern-Intra American Sea climatology.
A) Monthly mean precipitation amount from Centro de Proteccion e Higiene de la Radiocion; CPHR (Havana, Cuba) and the Nassau rain gauge (1855-2017), adapted from (Sullivan et al., 2020), B) monthly mean δ^2H_{precip} from Centro de Proteccion e Higiene de la Radiocion; CPHR (Havana, Cuba).

3.3. Methods

3.3.1. Fieldwork

The shallow water depth and small size (<4 m) of EMLD allowed the sediment water interface to be extensively observed by snorkelers prior to sediment coring, and the shallow subsurface was explored with probes. While sediment was easily penetrated in the upper surface, there is a notable layer of pine needles in the shallow subsurface. Sediment vibracores were collected from EMLD in 2016 (EMLD C1, C2, C4) using 7.6 cm diameter aluminum pipe that were fitted with a polystyrene core catcher at the base of the pipe (i.e., core nose) to enhance the likelihood of recovery in unlithified sedimentary sequences. Additionally, a hand-driven push core was recovered in December 2018 (EMLD RP5) to sample the upper ~1 m of sediment. The push core RP5

was 7.6 cm diameter polycarbonate pipe that did not have a core catcher installed, which offers the best opportunities for careful collection of the upper stratigraphic column and sediment-water interface. Immediately after coring, and while the pipe was still positioned vertically in the water column, floral foam was manually inserted into the core pipe to stabilize the sediment-water interface. This procedure preserves the upper 10 cm of the core while the long core pipes are stored and transported horizontally. All cores were split lengthwise, photographed, X-rayed, and stored at 4°C until further analysis. Depth-wise hydrographic profiles were collected from both sites in multiple seasons spanning several years to better characterize water column variability [June 2016, January 2017, January 2018, July 2018, and July 2019 (**Fig. 3:3**)]. Temperature (±0.01°C), salinity (±0.1 psu), pH (±0.1 pH units), dissolved oxygen (±0.1 mg L^{-1}), and depth (±0.004 m) were measured using a YSI EXO1 Multiparameter Sonde, with data collected at a sampling rate of 2 measurements per second. The multi-parameter probe was routinely calibrated before deployment, and the pH sensor was replaced annually before fieldwork to promote accuracy in field measurements. Salinity was determined automatically from the sonde conductivity and temperature readings using instrument instructions, which includes using algorithms found in Standard Methods for the Examination of Water and Wastewater (ed. 1989, in reference to the conductivity of standard seawater at 15°C). Lastly, a low salinity Onset HOBO Data Logger (CTD, U24-001), calibrated for the full range conductivity (0 to 10,000 μS/cm) was deployed within the water column of EMLD at ~1.84 m near EMLD C2 (**Fig. 3:1**) to continuously measure temperature and conductivity from January 2017 to January 2018, and from

December 2018 to June 2019. Salinity was calculated using the factory calibration for full salinity range in the proprietary HOBOware software (**Fig. 3:4**).

The coarse sediment content in the stratigraphy (>63 μm) was contiguously measured downcore using the Sieve-first Loss-on-Ignition (LOI) procedure (van Hengstum et al., 2016). Sub-samples (2.5 cm^3) were contiguously sampled downcore at 1 cm increments for EMLD C1, C2, C4 and RP5. Samples were first wet-sieved over a 63 μm mesh, dried for 12 h in an oven at 80°C and weighed to determine the original sediment mass. Samples were then combusted for 4 h at 550°C in a muffle furnace to remove sedimentary organic matter [choice of temperature selection based on experiments of (Heiri et al., 2001)]. Samples were then re-weighed post-combustion to determine mineral mass. The variability in coarse sediment fraction was then expressed as mass per unit volume (D >63 μm mg cm^{-3}). Additionally, a separate 1.25 cm^3 sub-sample, sampling continuously downcore at 1 cm intervals, was subjected to a Classic LOI procedure following standard methods (550°C, 4.5 hours) to determine bulk organic matter content, reported as weight percent (%) of the original sediment mass (Heiri et al., 2001). Uncertainty on replicate sieve first and Classic LOI measurements is typically less than ± 1%. To further examine the nature of sedimentary particles in the coarse sediment fraction, test samples were sieved over a 63 μm mesh and examined wet in Petri dishes using stereomicroscopy.

3.3.2. Age Model

Terrestrial plant macrofossils (n = 30) were radiocarbon dated at the National Ocean Sciences Accelerator Mass Spectrometer at Woods Hole Oceanographic

Institution to generate downcore age models for the cores and calculate sedimentation rates (**Table 1**). The conventional radiocarbon age results were calibrated into calendar years before present (cal yr BP) with IntCal20 using 1950 CE as present (Reimer et al., 2020). The final downcore Bayesian age model (**Fig. 3:9**) for EMLD C1, C2, C4 and RP5 was computed with Bacon (v2.5.1) in R. This output provides probability estimates at each designated level downcore (Blaauw and Christen, 2011), and we calculated age outputs for every contiguous cm downcore.

3.3.3. Leaf Wax Biomarkers

Isotopic signatures measured on individual compound classes of specific geochemical markers (biomarkers) can quantify the precursor biochemical processes, which allows for detailed reconstruction of past environments (Hayes et al., 1990). The hydrogen isotopic composition of δ^2H measured on alkanoic acids of terrestrial plant leaf waxes are demonstrated proxies for prehistoric precipitation δ^2H (Estep and Hoering, 1980; Sternberg, 1988). It has been found that the hydrogen isotopic ratio preserved in geochemical biomarkers, such as plant derived leaf wax lipids, correlates to the source water used during photosynthesis (Sessions et al., 1999). Sediment sub-samples were collected for biomarker analysis every 10 cm (~every 120 years) within EMLD-C4, with additional samples added for higher resolution (n = 110) and every ~50 years in RP5 (n = 12). Each sub-sample integrates 1 cm of stratigraphy, or ~12 years of inputs in EMLD C4 and ~9 years of inputs in EMLD RP5. Samples were freeze dried and homogenized with a mortar and pestle. Methods for lipid extraction, quantification and isotopic

analysis of these sinkhole sediments follow closely to published methods used in a nearby sinkhole (Tamalavage et al., 2020). Briefly, *n*-alkanoic acids (as fatty acid methyl esters, FAME) were identified by gas chromatography/mass spectrometry (GC/MS) and quantified by a flame ionization detector (FID) on an Agilent GC-MSD/FID, and then injected via a split/splitless inlet in splitless mode to a capillary column (Rxi®-5ms 30 m x 0.25 mm, film thickness 0.25 mm). Quantification was achieved using an in-house standard comprising a mixture of 4 *n*-alkanes and 3 *n*-alkanoic acids of varied and known concentration, with the linear calibrations determined separately for the two compound classes.

Measurements for compound-specific hydrogen isotopic values using gas chromatography isotope ratio mass spectrometry (GC-IRMS) were attempted for 74 samples (EMLD-C4) and 19 samples for compound-specific carbon isotopic analysis. However, due to challenges with core-top sediment recovery and low *n*-alkanoic acid concentrations for terrestrially-derived C_{28} (further described below), trustable hydrogen isotopic measurements were made on 29 samples (below 213.5 cm total core depth) for δ^2H and 12 measurements for $\delta^{13}C$. A Thermo Scientific Trace gas chromatograph equipped with a Rxi-5ms column (30 m x 0.25 mm, film thickness 0.25 μm) and a programmable temperature vaporizing (PTV) injector operated in solvent split mode with an evaporation temperature of 60°C. The GC was connected via a GC Isolink with pyrolysis furnace (at 1400°C) via a Conflo IV interface to a DeltaVPlus isotope ratio mass spectrometer. To check for linearity, the H_3^+ factor was measured daily and remained close to 4 ppm mV^{-1} (across 1−8 V), for CO_2 the standard deviation of

reference pulses was better than 0.9‰. Reference peaks of H_2 or CO_2 were co-injected during the course of a GC-IRMS run; two were used for standardization. Samples were interspersed with standard compound mixtures of known isotopic composition, with several standards run per day.

Data were normalized to the VSMOW/SLAP hydrogen isotopic scale by comparing with an external standard (A3 mix for samples run before August 2017; A6 mix for samples run after August 2017) obtained from A. Schimmelmann (Indiana University) containing 15 *n*-alkane compounds (C_{16} to C_{30}), with δ^2H values spanning −46 to −227‰; and $\delta^{13}C$ values spanning −33.37 to −28.61‰ for A3 mix and −33.97 to −26.15‰ for A6 mix. The RMS error determined by replicate measurements of the standard across the course of analyses was 3.7‰ for δ^2H and 0.21‰ $\delta^{13}C$. Correction for H or C added by methylation of FAs as methyl esters was made by way of mass balance (Lee et al., 2017). The results are reported using conventional delta notation (δ^2H and $\delta^{13}C$ in permil: ‰),

$$\delta=(R_{sample}-R_{standard})/R_{standard} \quad (1)$$

in which R is $^2H/^1H$ or $^{13}C/^{12}C$, respectively.

Isotopic fractionations between δ_a and δ_b, as ^2H-depletion factors ($\varepsilon_{a/b}$), were calculated with the following equation:

$$\varepsilon_{a/b} = \alpha_{a/b} - 1 = [(\delta_a+1)/(\delta_b+1)] - 1 \quad (2)$$

3.4. Results

3.4.1. Modern Water Column Physical Properties

The five water column profiles collected over multiple years indicate that physical and chemical conditions in the water column are vertically and seasonally dynamic (**Fig. 3:4**). In unconfined carbonate aquifers, sinkholes essentially function as uncased wells, and their internal hydrography reflects conditions of the local aquifer. In general, the hydrographic structure that is observed in other similar sinkhole lakes is three, distinct salinity-stratified water layers: an upper meteoric lens (fresh to slightly oligohaline), a transitional mixing zone, and basal saline groundwater (van Hengstum et al., 2016; van Hengstum et al., 2018; van Hengstum et al., 2020). As defined by others (Beddows et al., 2007), the mixing zone can be defined as the layer that separates isohaline and isothermal values. These stratified water layers are not easily defined within EMLD pond. For example, casts taken in January 2018, July 2018, and June 2016 measure a relatively isothermal water column (variability <1° C), with higher temperatures (~28° C) observed in the entire water column during boreal summer. The greatest vertical temperature variability (~4° C) and a defined thermocline were observed in January 2017. Although all measured salinities are within the oligohaline range (0.5 to 5 psu), a subtle halocline can be observed in June 2016, January 2017, July 2018, July 2019 between the uppermost fresh meteoric lens. Surface salinities of the meteoric lens range from 1.2 to 1.6 psu, and the depth at which salinity begins to change is varied (e.g., 1.8 m in January 2017 versus 2.2 m in July 2018). pH values in the meteoric lens range from 7.5 to 7.9 (mean: 7.8 ± 0.04), decreasing along salinity

(density) gradients to values ~0.3 pH less than surface measurements. Dissolved oxygen concentration in the meteoric lens ranges from 6.3 to 8.4 mg/L (highest during boreal winter), with decreasing concentration with depth along physicochemical gradients. At the sediment-water interface at ~3 m depth, which is most of the flat sinkhole-lake bottom, the mean dissolved oxygen concentration is 0.4 to 5.4 mg/L (highest concentration during January 2018 cast), ranging from dysoxic to oxic conditions (Tyson and Pearson, 1991). Given the overall parameters measured, we consider that EMLD is flooded by the meteoric lens of the local unconfined aquifer in the carbonate platform. However, hydrographic conditions are sensitive to seasonal changes in atmospheric conditions caused by: its shallow water column (~3 m), narrow diameter (~26 m), small water volume, close proximity of the water table to the subaerial landscape (~4 m cliff), changes in either the chemistry of groundwater, direct freshwater additions through rainfall, or evaporation which impacts salinity at the sediment-water interface.

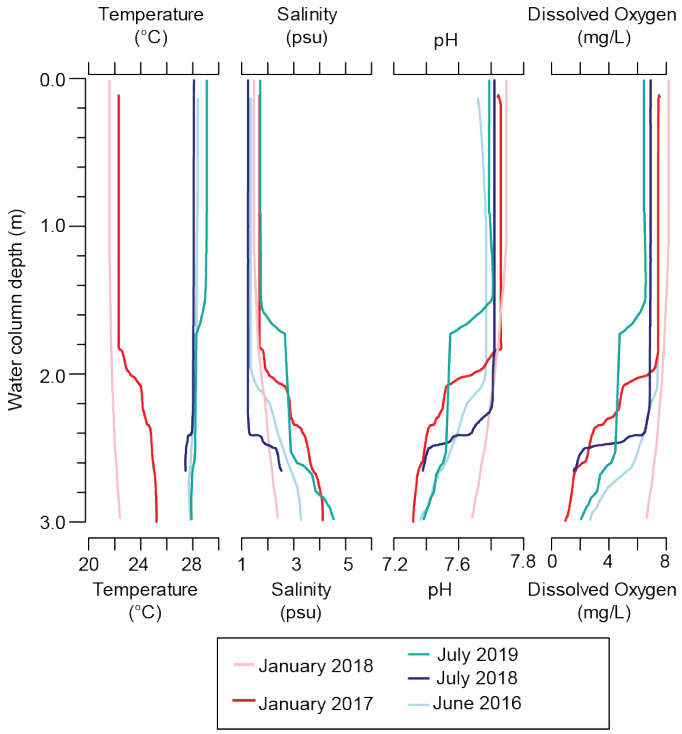

Figure 3:3: Hydrographic profiles from EMLD using a YSI EXO1 Multiparameter Sonde, not vertically corrected for tidal variability of the water table.

The deployed HOBO sensor at the sediment-water interface (~1.84 m) near EMLD C2 consecutively recorded temperature, conductivity, and salinity from February 2017 (2/14/17) to January 2018 (1/9/2018) and from December 2018 (12/5/18) - June 2019 (6/27/2019), with a data logging failure from January 2018 through December 2018. Mean annual temperature is 27.3° C ± 1 at ~1.84 m water depth ranging from 24.7 to 33.4° C and is ~4° C warmer in boreal summer. Mean annual salinity at ~1.84 m depth is 5.1 psu ± 0.9, ranging from 2.1 to 7.1 psu (**Fig. 3:4**), with monthly variability of ~ 2 psu. The range of temperatures and salinities measured *in-situ* across 18 months extend beyond what was measured within the five collected EXO casts. Yet, mean HOBO temperatures are similar to measured EXO values. Mean salinity measured by

the HOBO sensor can be up to ~4 psu higher at ~1.84m depth than values measured through EXO casts, which may be due to using the HOBOware factory calibration, or perhaps positioning of the cast in the basin. Importantly, both the HOBO sensor and EXO sonde values display the same trends: the wet season (boreal summer) is warmer with higher salinity, versus the dry season (boreal winter) is cooler with lower salinity.

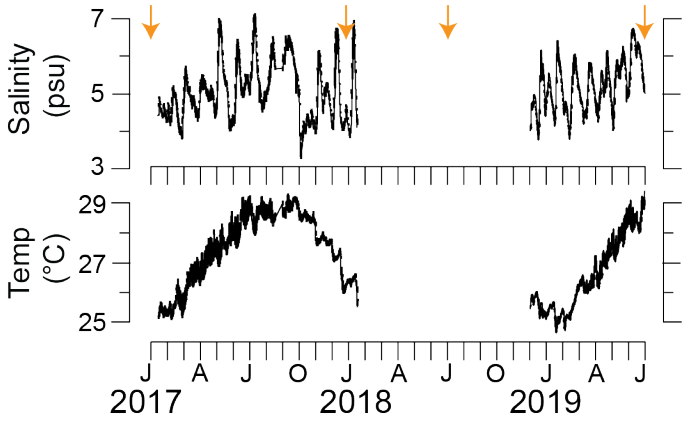

Figure 3:4: HOBO Temperature and salinity data.
Logger at ~1.8 m in the EMLD pond water column, collected by Onset HOBO data loggers from January 2017 to July 2018, orange arrows denote additional water column casts using the EXO sonde (**Fig. 3:3**).

3.4.2. Sediment Stratigraphy and Age Model

All conventional radiocarbon dates are reported (**Appendix A, Table 1**), and were used to generated age models using Bacon v. 2.5 (**Figure 3:9**) for further time-wise comparison between cores. Calibrated radiocarbon dates (using IntCal 20) are presented along stratigraphic data for depth-wise comparison between cores (**Figure 3:5**). Coring efforts terminated at a similar subsurface level, and basal sediment recovery in the in the

core pipes included medium to coarse carbonate fragments (e.g., EMLD C4). Immediately above the carbonate fragments, a peat deposit was recovered within EMLD C4. Similar basal sediments were previously observed (Slayton, 2010), which suggests we have recovered the available unlithified stratigraphy preserved in EMLD Pond. The peat deposit has a bulk OM content exceeding 65%, and it contained fibrous leaf and wood fragments in a fine grained organic-rich matrix. Terrestrial plant macrofossils at the base of the peat deposit were aged to 8235 ± 30 cal yr BP, which provides a minimum age for the onset of peat accumulation. Radiocarbon dates just above the transition to lacustrine marl above were aged to 8250 ± 15 (2σ) cal yr BP and 8100 ± 75 (2σ) cal yr BP (EMLD C4) and 8040 ± 360 (2σ) cal yr BP (EMLD C2), which indicates that conditions suitable for peat accumulation at the bottom of the sinkhole were no longer present (i.e., internal environmental change). Results for age model (using Bacon) (**Fig. 3:9**) indicate that carbonate marl deposition began at ~8290 cal yr BP within EMLD C4, and is consistent within EMLD C2 (recording lacustrine marl by ~8050 cal yr BP). EMLD C1 sampled lacustrine marl deposited from ~5200 to 2650 cal yr BP. However, lacustrine marl deposition in Emerald Pond likely persisted until ~1700 cal yr BP based on a marl-sapropel sedimentary transition observed in RP5. Sedimentation rate in the marl unit within EMLD C2 (1.4 cm/yr) was similar to EMLD C2 (1.2 cm/yr). However, the sedimentation rate was slower from ~5200 to 2260 cal yr BP in the lacustrine marl unit archived in EMLD C1 (0.9 cm/yr), and within the small amount of marl recovered (~13 cm) in EMLD RP5 (0.6 cm/yr). In general, the recovered stratigraphy indicates a rapid change in sedimentary rate and environmental conditions

in EMLD over the last ~3000 years that is consistent across the retrieved cores. EMLD C2 and C4 did not recover any sediment younger than ~3200 cal yrs BP and ~2700 cal yrs BP, respectively. We think this was caused by sampling interference from the pine needle layer in the shallow surface and core catcher in the aluminum pipe (i.e., core nose) acting as a barrier to sampling watery upper sediments until older (>3000-year-old) compacted carbonate marl units were penetrated. Based on previous work (Slayton, 2010), and new results presented here, lacustrine marl was continuously deposited from ~8200 to 1700 cal yrs BP.

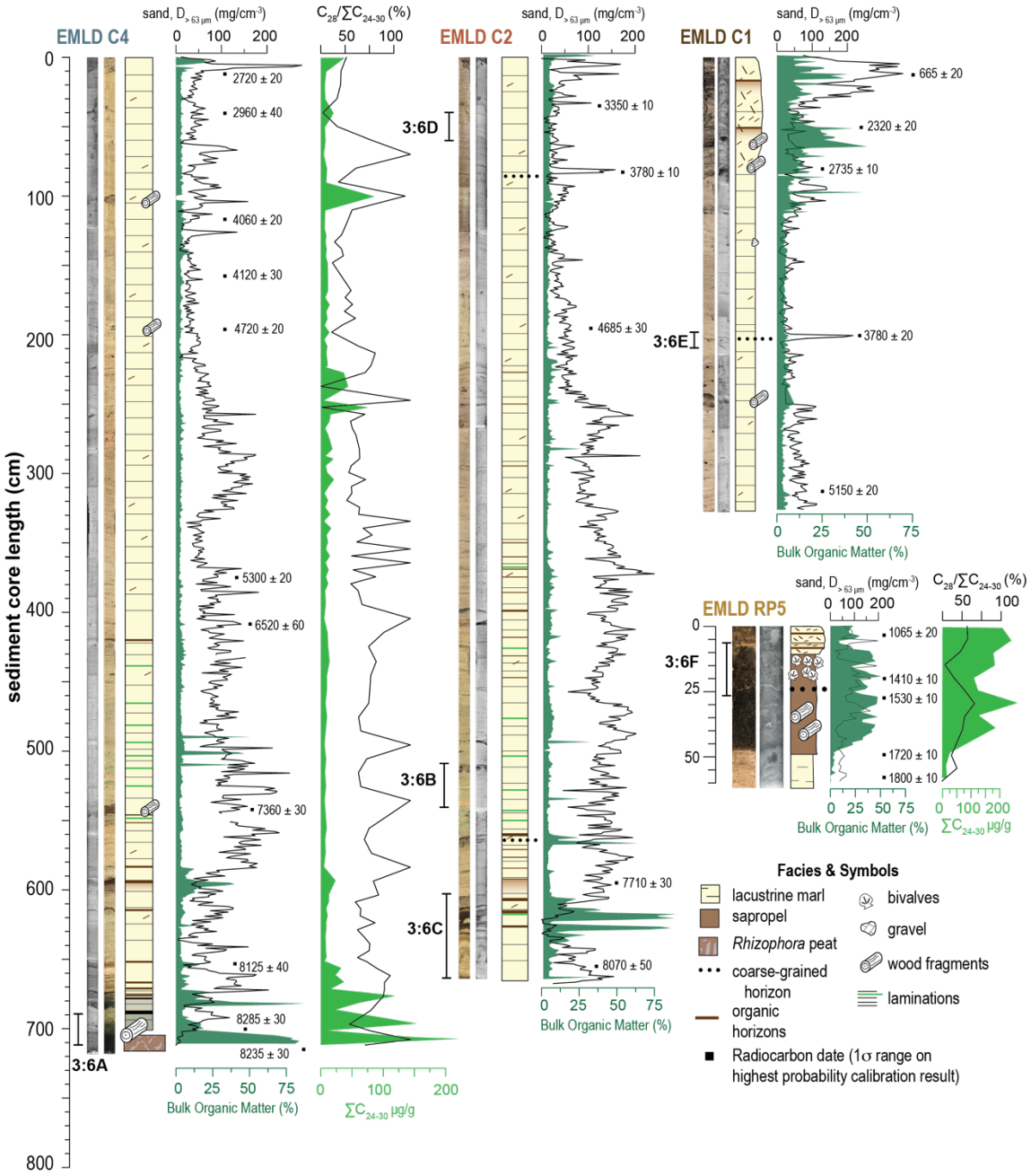

Figure 3:5: Stratigraphic columns and radiocarbon dates for EMLD.
Selected, bracketed sections (e.g., 3:6A on EMLD C4) of each core are referenced to a larger resolution image within Fig. 3:6. Also plotted: downcore coarse-grained particle deposition (Sieve-first LOI, D> 63µm), bulk organic matter (dark green, Classic LOI, weight %), sum of *n*-alkanoic acids (light green) $C_{24\text{-}30}$ (µg/g) for EMLD C4 and EMLD RP5, and relative abundance of C_{28} *n*-alkanoic acid (%) for EMLD C4 and EMLD RP5.

Qualitatively, the carbonate marl is dominated by a fine-grained carbonate mineral matrix and visible organic matter fragments (e.g., pine needles, bark, leaf fragments). At the base of the carbonate marl section, distinctive organic-rich horizons were present above the basal peat (e.g., **Fig 3:5**, EMLD C4), but these organic-rich horizons were not routinely observed throughout the carbonate marl unit. While not always visible in the photographs, the x-radiographs document continuous laminations throughout the carbonate marl unit, which suggests little vertical sediment mixing has occurred (e.g., bioturbation, **Fig 3:6D**). From ~8140 to 6000 cal yr BP, there are organic-rich horizons and green layers depositing within the marl unit. Qualitatively, the layers of green-hued sediment preserved within EMLD C2 (430 to 660 cm) and EMLD C4 (440 to 690 cm), have no major observable change in sediment texture or composition (**Fig. 3:6B**). The green-hued intervals could be due to preserved blue-green algal remains in the sedimentary matrix, which thrives in shallow, coastal carbonate environments (Black, 1932). The carbonate marl unit younger than ~6000 cal yr BP no longer has the distinctive green-hued intervals or organic-rich horizons that characterized the older part of the unit. There are occasional inclusions of coarse-grained shell material like gastropods throughout the carbonate marl, (**Fig. 3:5**). The carbonate marl contains ostracode remains like *Darwinula stevensoni*, *Cypridopsis vidua*, and *Candonna anna*, and some testate amoebae like *Centropyxis aculeata* and *Arcella vulgaris.* These ostracodes are common in fresh to slightly oligohaline subtropical and tropical waters in the Bahamas (Teeter, 1989), Bermuda (Keyser and Schöning, 2000), south Florida (Keyser, 1978), and the testate amoebae found are known from fresh to

slightly oligohaline settings from sinkhole lakes in the Yucatan (Van Hengstum et al., 2008). As discussed further below, the carbonate marl was most likely deposited in lacustrine conditions (fresh to slightly oligohaline salinities) that are not characteristic of the current limnology in the sinkhole.

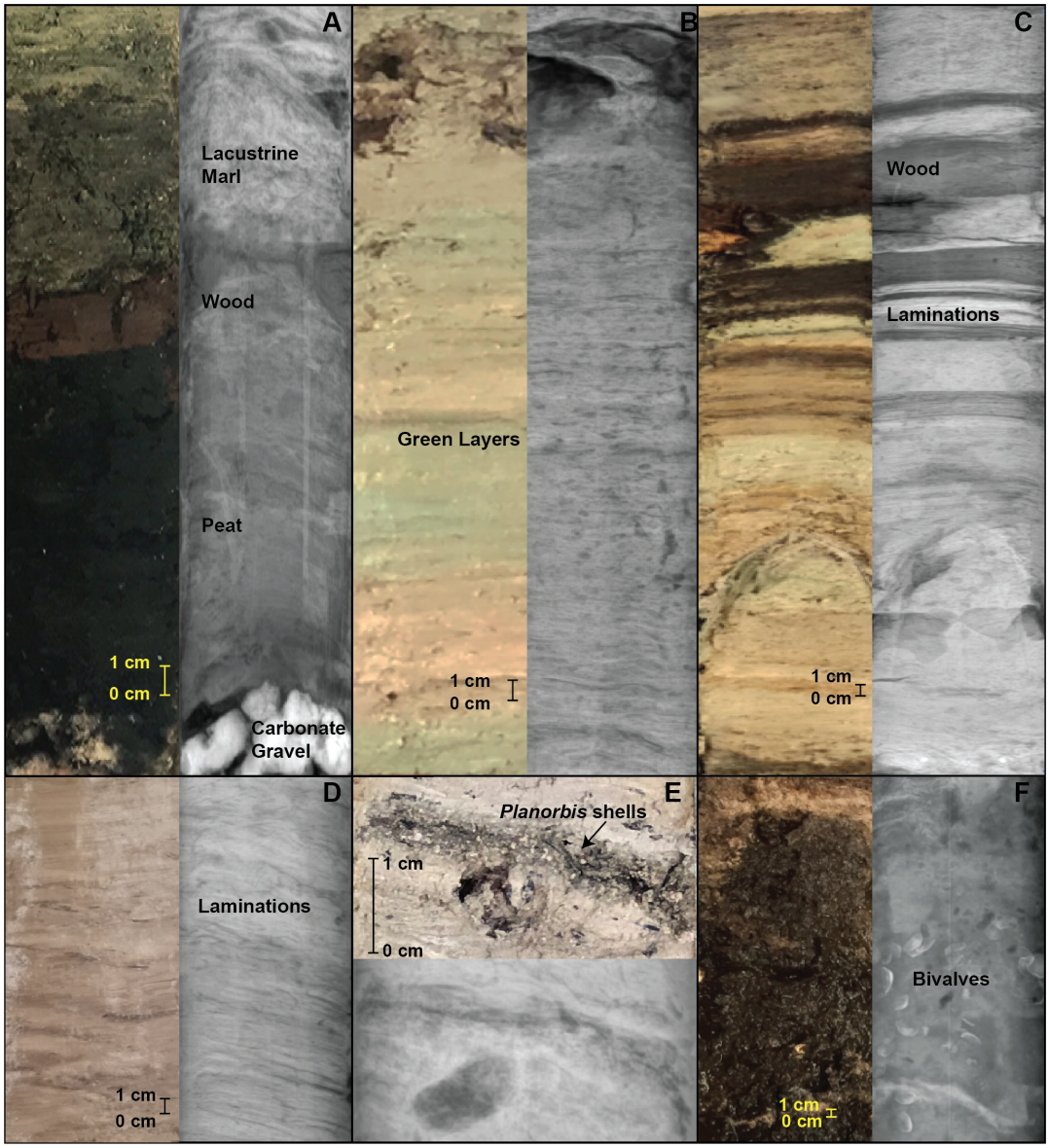

Figure 3:6: Larger photograph pop-outs and x-radiographs for EMLD.

Bracketed sections selected within Figure 2, A) ~690 to 716 cm within EMLD C4 showing basal peat to lacustrine marl transition, B) 510 to 540 cm of EMLD C2 showing green layers, C) ~605 to 670 cm of the basal stratigraphy of EMLD C2, D) ~40 to 60 cm of EMLD C2 showing homogenous carbonate mud with x-radiographed laminae, E) coarse grained deposit at ~208 cm within EMLD C1, and F) sapropel layer within EMLD C5 from ~7 to 26 cm with abundant bivalves throughout, visible within the x radiograph.

The carbonate marl has an average of ~6 ± 9% bulk OM (range: 1.3 to 86%) and variable content of coarse-grained (>63 μm) particles downcore (**Table 2**). In general, there are similar patterns of coarse particle deposition between the longer cores (EMLD C2 and EMLD C4). There is more coarse-particle content deposition and variability from ~8200 to 7100 cal yr BP (EMLD C4, mean: 117.8 μm /cm^3, ranges: 19.1 to 264.0), a salient decrease in coarse-particle deposition occurs at ~5000 cal yrs BP from ~ 117.8 to 56.1 μm /cm^3. Stereomicroscopic examination of 13 downcore sub-samples from EMLD C2, representing both intervals with increased (>140 mg/cm^3) and decreased coarse fraction content (<50 mg/cm^3), indicates that individual coarse particles are largely similar downcore. Ostracodes and biogenous calcite particles (**Fig. 3:7,** calcite tubes and circular particles) dominate the >63 μm particle fraction, but the quantity of individual constituents varied (e.g., ostracods versus biogenous calcite particles and tube structures). The tubular structures are similar to those described from other carbonate lakes, and they are thought to be autogenic calcite precipitation around submerged vegetation from increased pH related to primary productivity (Pełechaty et al., 2013). The origin of the tubular calcite structures in EMLD is inconclusive, but could be due to calcification around aquatic algae or vegetation (Leng et al., 2010). Offsets within the

basin (between EMLD C2 and C4 from ~7100 to 5200 cal yr BP) in the abundance of coarse-grained particles likely reflect site-specific variability within the sinkhole lake.

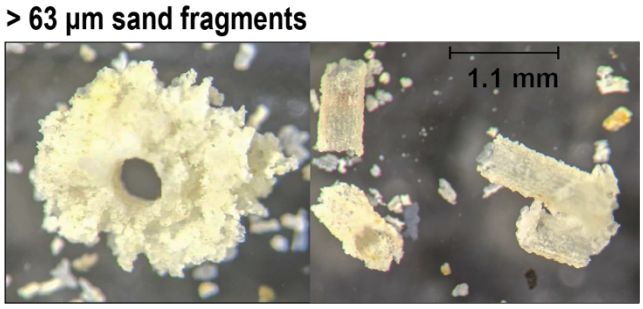

Figure 3:7: Biogenous coarse-grained particles >63 µm within EMLD Pond.

Table 3:1: Bulk Coarse Particle density and OM for the three main facies present within the EMLD cores.

Core	Coarse Particles Range (mg/cm^3)	Coarse Particles Mean (mg/cm^3)	Bulk OM (%) Range	Bulk OM (%) Mean
Peat	13.7 to 28.9	21.5 ± 5.5	3.0 to 79.4	79.5 ± 3.4
Marl	5.4 to 327.1	89.0 ± 5.7	0.3 to 88.0	5.7 ± 8.1
Sapropel	11.8 to 118.1	49.2 ± 26.4	31.0 to 86.0	62.2 ± 14.3

There is a distinct fine-grained biogenic sapropel in the upper 50 cm of RP5, and a transition to more organic rich sediments in EMLD C1 (**Fig. 3:5**). These deposits are not present in EMLD C2 and C4, and are most likely the youngest sediments preserved in EMLD. Sapropels are fine-grained organic matter deposits that are derived from decomposed algal, bacterial, or higher plant sources (Schnurrenberger et al., 2003). Mean bulk OM% within the sapropel unit of EMLD RP5 (10–45 cm) was 65.6 ± 11.6% (**Fig. 15**), which is an order of magnitude higher OM than observed in the carbonate marl unit. The lower part of the sapropel also contained bivalves in a concentration not

observed elsewhere in the cores. Based on the radiocarbon date at 49.5 cm (1720 ± 10 cal yr BP) in EMLD RP5, the sapropel started to accumulate after ~1700 cal yrs BP. A younger age of ~1000 years ago was obtained near the top of EMLD C5 (~5 cm depth), which suggests that sedimentation has drastically reduced during the last millennium. The sapropel dates from RP5 are consistent with the salient decrease in sedimentation rate observed in EMLD C1, assuming that the radiocarbon date from 10.5 cm (665 ± 20 cal yr BP) in EMLD C1 is an accurate reflection of its stratigraphic age.

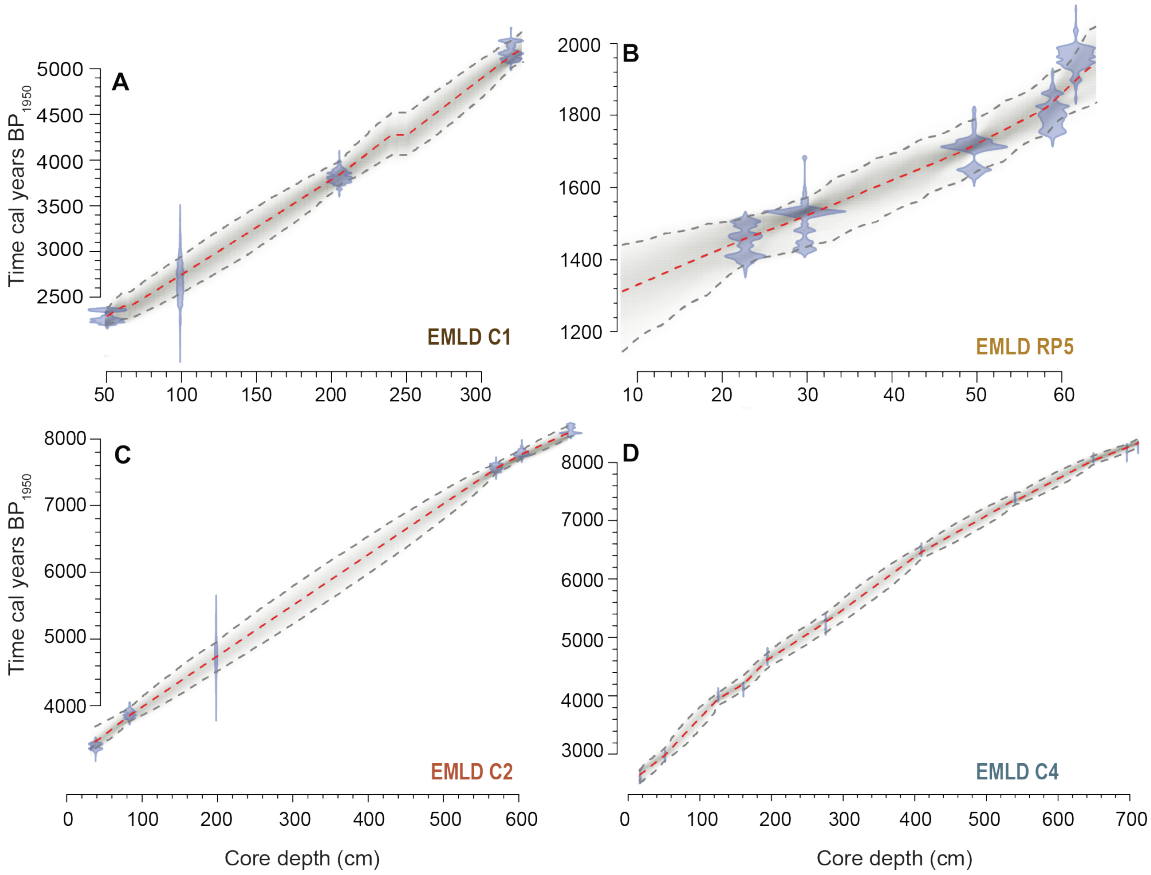

Figure 3:8: Bayesian age models for all EMLD cores using Bacon (v2.5.1) in R. Dated substrates (blue shaded shapes) are terrestrial macrofossils (**Appendix A, Table 1**), gray dashed lines bound the minimum and maximum 95% confidence interval around possible model age-depth outputs, with the red line representing the 'best' model based on the mean age for each depth (Blaauw and Christen, 2011)

3.4.3. *n*-alkanoic acid Abundance

We find plant wax *n*-alkanoic acids with characteristic homologous series distributions typical of vascular, terrestrial plants (Freeman and Pancost, 2014). Within EMLD C4, concentrations of *n*-alkanoic acids with chain lengths of 24 (0.4 to 59 μg/g), 26 (0.4 to 40.6 μg/g), 28 (0.2 to 216.9 μg/g) and 30 (0.2 to 57.5 μg/g) Although, concentrations of C_{28} decline after ~4700 cal yr BP (some samples < ~1 μg/g). Overall, the modal chain length of *n*-alkanoic acids was 28, with an Average Chain Length (ACL) of 27 ± 0.8 (1 σ, *n* = 105). The average Carbon Preference Index (CPI) was 8.9 ± 7. Both ACL and CPI indicate inputs from terrestrial higher plants (Freeman and Pancost, 2013). Within EMLD RP5, *n*-alkanoic acids were quantified with carbon chain lengths of 24 (3.2 to 34.3 μg/g), 26 (3.9 to 51.5 μg/g), 28 (2.1 to 101.3 μg/g) and 30 (1.6 to 58.1 μg/g). The modal chain length was 28 with an ACL of 27 ± 0.5 (1 σ, *n* = 12).

The sum of *n*-alkanoic acid concentrations ($C_{24\text{-}30}$) tracks with bulk OM% (e.g., increase in Σ acids with increased OM%) downcore in both EMLD C4 and RP5 (**Fig. 3:5**), providing evidence of continuous organic matter input to EMLD Pond through time. There are two main patterns in chain length abundance in EMLD C4 from ~8320 to 4780 and ~4780 to 2630 cal yr BP. C_{28} has a higher relative abundance ($C_{28}/\Sigma\ C_{24}{:}C_{30}$) between 8320 to 4780 cal yrs BP (mean 30%), compared to 16% from 4770 to 2630 cal yrs BP (**Fig. 3:10**), and this higher abundance of C_{28} is synchronous to a decrease in >63 μm particle density. The dominant C_{28} *n*-alkanoic acid relative

abundance from ~8300 to 4800 cal yr BP is typical of tropical forests (Feakins et al., 2016a). Although *n*-alkanoic chain lengths from C_{24}-C_{30} are common in land plants, C_{24} and C_{26} can also derive from submerged/floating aquatic macrophytes (Ficken et al., 2000). Therefore, the decrease in C_{28} *n*-alkanoic acid dominance (from 30 to 16% relative abundance) after ~4800 cal yr BP and increased dominance of C_{26} (**Fig. 3:10B**) could be due to increased inputs from aquatic plants (Ficken et al., 2000). Whereas we infer the C_{28} chain length derives from terrestrial plants.

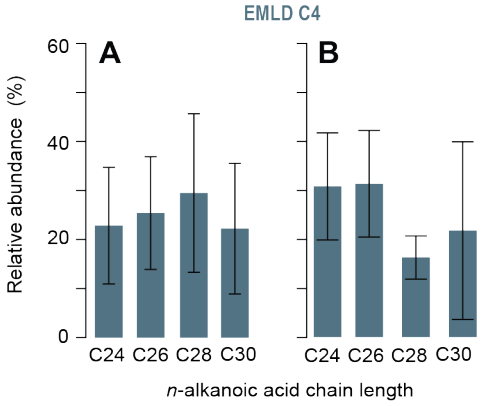

Figure 3:9: Chain length abundance of *n*-alkanoic acids.
Displaying for A) whole core, and B) 0.5-213.5 cm, ~213 cm is synchronous with a change in coarse grained particle deposition (D> 63μm).

3.4.4. Hydrogen and Carbon Isotopic Composition

Hydrogen isotopic compositions of *n*-alkanoic acids from EMLD C4 ranged from –186 to –127‰ (mean = –12‰, 1σ=12‰, *n* = 38) for C_{24}, –178 to –107‰ (mean = –149‰, 1σ = 15‰, *n* = 36) for C_{26}, –190 to –77‰ (mean = –138‰, 1σ =21‰, *n* = 29) for C_{28}, and –154 to –117‰ (mean = –138‰, 1σ = 11‰, *n* = 9) for C_{30} through the core (**Fig. 3:11A**). Values of δ^2H_{28} span ~110‰ throughout the record. δ^2H_{28} values were

relatively stable from ~7680 to 6150 cal yr BP (mean = –133, 1σ = 5‰, *n* =15), and are generally more depleted from ~5975 to 4780 cal yr BP (mean = –133, 1σ = 19‰, *n* = 10). In order to reconstruct precipitation we apply the net fractionations ($\varepsilon_{28/precip}$) of –121‰ (± 3‰) reported for C_{28} *n*-alkanoic acids within tropical forests (Feakins et al., 2016a) was used to calculate δ^2H_{precip} . Reconstructed δ^2H_{precip} values from ~8320 to 4780 cal yr BP ranged from –68 to 12‰ (mean = –22‰, 1σ = 20‰) (**Fig. 3:11C**).

Carbon isotopic compositions of n-alkanoic acids from EMLD C4 ranged from–35 to –27‰ (mean = –32‰, 1σ = 2‰, *n* = 12) for C_{24}, –37 to –28‰ (mean = –33‰, 1σ = 3‰, *n* = 12) for C_{26}, –39 to –30‰ (mean = –34‰, 1σ = 3‰, *n* = 12) for C_{28}, and –37 to –28‰ (mean = –33‰, 1σ = 2‰, *n* = 12) for C_{30}. $\delta^{13}C_{28}$ values were determined for a subset of 18 samples downcore EMLD C4 (**Fig. 3:11C)**. Values of δ^2C_{28} span ~9‰ throughout the record. $\delta^{13}C_{28}$ values are most depleted within from ~7600 to 7100 cal yr BP, aligning with values measured in late Holocene records from nearby Blackwood sinkhole (Tamalavage et al., 2020; Chapter II) when pollen indicate there was abundant tropical hardwoods and palms on the landscape (Tamalavage et al., 2020; Fall et al., 2021). Values are most depleted from ~7875 to 7125 cal yr BP (mean = –39‰, 1σ = 0.8‰). The most enriched $\delta^{13}C_{28}$ value is at ~4785 cal yr BP, synchronous with depleted values of δ^2H_{28}. From ~4200 to 2700 cal yr BP, low concentrations of C_{28} < ~1 µg/g, made it difficult to obtain sufficient abundance for robust isotopic determinations in the processed samples. Using a larger sub-sample size (~>20 g) would be needed to extend the record to the later Holocene.

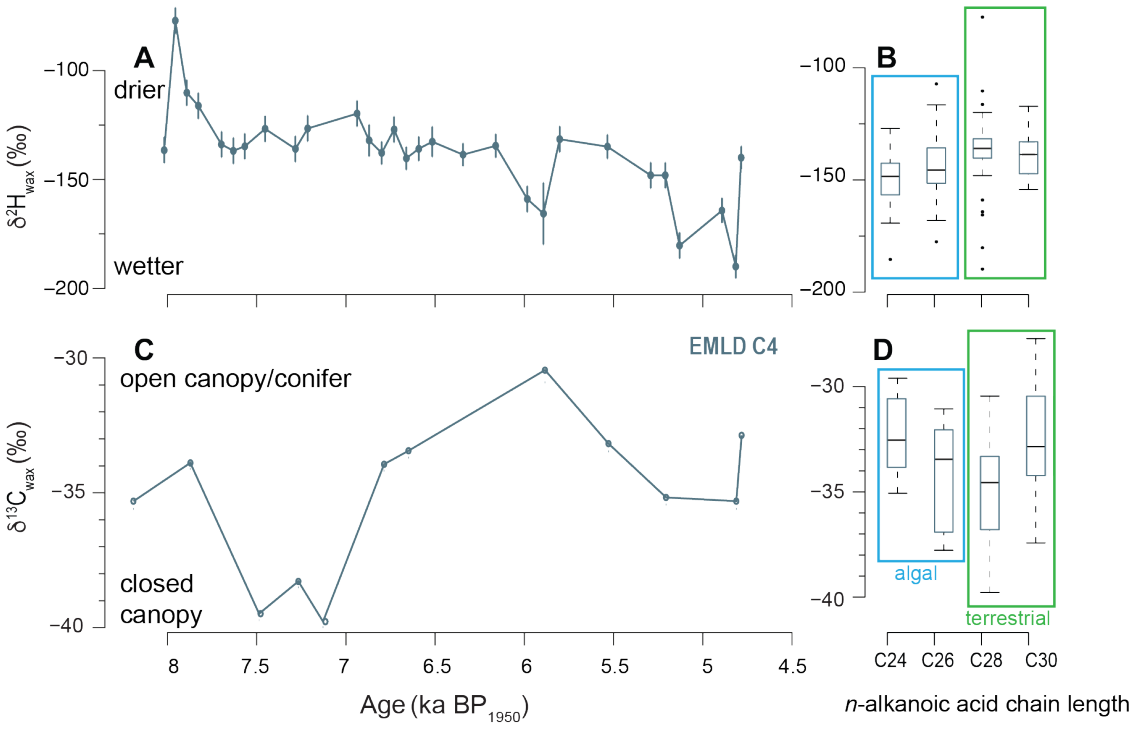

Figure 3:10: Hydrogen isotopic measurements for *n*-alkanoic acids within EMLD C4. Showing (A) downcore δ^2H_{28} values for the mid-Holocene, (B) δ^2H values by chain length for the even chain length C_{24} to C_{30} *n*-alkanoic acids, (C) downcore $\delta^{13}C_{28}$ values, and (D) $\delta^{13}C$ values by chain length for the even chain length C_{24} to C_{30} *n*-alkanoic acids. Box and whisker plots (B, D) show median (thick line), interquartile range (box), and range (whiskers). Based on abundance and isotopic composition, the C_{28} and C_{30} *n*-alkanoic acids are thought to be terrestrially-derived, whereas the C_{24} and C_{26} are thought to have substantial algal influence.

3.5. Discussion

3.5.1. Paleolimnology of Emerald Pond

Three primary facies characterize the deglacial stratigraphic architecture in Emerald Pond: (i) a basal peat that accumulated from ~8350 to 8290 cal yrs BP, (ii) a

lacustrine carbonate marl that accumulated from ~8290 to 1700 cal yrs BP, and (iii) a sapropel unit that was deposited from ~1700 to 1310 cal yrs BP and preserved in the northeastern portion of the lake (core RP5). While older deposits may be present at the base of the sinkhole, the carbonate gravel collected at the base of EMLD C4 suggests that the entire unlithified sedimentary sequence in the sinkhole lake was sampled. All three unlithified sedimentary deposits have been previously recovered from other lakes on carbonate landscapes (e.g., sinkhole lakes, karst depressions) in the tropical North Atlantic region, and these previous studies provide modern and prehistoric analogs to inform the past sedimentary processes operating in EMLD Pond.

On carbonate platforms that are devoid of fluvial systems, rainwater directly infiltrates into aquifers whose elevation is ultimately linked to glacioeustic sea-level change (Richards et al., 1994; Surić et al., 2005; van Hengstum et al., 2011). Basal mangrove and terrestrial peats on the epikarst surface have been widely used to understand regional sea-level histories (Boardman et al., 1989; Rasmussen et al., 1990; Gehrels, 1999; Toscano and Macintyre, 2003; Törnqvist et al., 2004), and at a minimum they can provide a maximum sea-level indicator (Milne and Peros, 2013; Khan et al., 2017). Basal peats can also form in sinkholes lakes when a wetland becomes established *in situ* on the sinkhole tallus pile (formed from initial carbonate collapse) as concomitant eustatic sea level and the local groundwater system rose during the last deglacial (Gabriel et al., 2009). On Abaco Island, basal *in situ* peat deposits were found in No Man's Land (van Hengstum et al., 2018) and Freshwater River Blue Hole (van Hengstum et al., 2020), but basal peat in Runway Sinkhole is possibly organic matter

transported from elsewhere on the adjacent epikarst surface (Kovacs et al., 2013). Elsewhere in the region, basal peat deposits in sinkhole lakes have also been documented including: Mullet Pond in Florida (Lane et al., 2011), Cenote Carwash in the Yucatan Peninsula (Gabriel et al., 2009), and Grand Bahama (van Hengstum and Bernhard, 2016). However, basal peat development is not guaranteed in sinkhole basins. Little Salt Spring in Florida does not have basal peat (Zarikian et al., 2005; Gregory, 2016), and the initial deposits above a hardground in Cenote Jennifer in Cuba are carbonate marl deposits like EMLD Pond. Because of hydraulic head, there are elevational differences between the groundwater table inland and sea level at the shoreline (Beddows et al., 2007; Martin et al., 2012), so basal peats can only be a terrestrial-limiting sea-level indicator. The presence of fibrous organic matter and mangrove pollen (Slayton, 2010) within the peat deposit at EMLD pond suggest wetland taxa (e.g., *Rhizophora mangle*, *Laguncularia racemosa*) growing *in situ.* The most confident ages and elevations for basal peat from sinkhole lakes in Abaco plot just above, or within uncertainty, of the sea-level curve for the northern Bahamas (**Fig. 3:12H**).

Most of the stratigraphic sequence in EMLD Pond above the basal peat is carbonate marl, which is consistent with the expectation of early sedimentologists (Shinn et al., 1996) and found within other sinkhole lakes in the Bahamas (van Hengstum et al., 2018) and Cuba (Peros et al., 2017). Extensive geochemistry and sedimentology conducted at Wallywash Great Pond (WGP, 17.97°, –77.80°, max, 5 m water depth, size: 0.76 km^2) in Jamaica provides one of the best modern analog sites in the tropical

North Atlantic (Street-Perrott et al., 1993; Holmes et al., 1995a; Holmes et al., 1995b), which can be used to infer favorable conditions for middle to late Holocene marl deposition in EMLD Pond in Abaco. At least 3 m of lacustrine marl was deposited in WGP during the late Holocene, and current lake water in central WGP has a pH range of 8.2 to 8.6, total dissolved solids 0.43 ppt, and alkalinity of 3.6 to 3.9 meq/l (Street-Perrott et al., 1993; Holmes et al., 1995a; Holmes et al., 1995b). Additionally, the isotopic composition of lake water (δ^2H, $\delta^{18}O$) indicate good vertical mixing and at least 30% evaporation as lake water flows from south to the north (Holmes et al., 1995a). Inflowing groundwater at a spring has much lower pH (7.5) and an alkalinity of 4.8-5.1 meq/l (Street-Perrott et al., 1993). The periphery of WGP is a freshwater swamp (*Typha*, *Cyperus*, and *Cladium*) that transitions to floating macrophytes (*Nymphaea*, *Nymphoides*) with increased bathymetry, and the deepest areas have submerged macrophytes (*Potamogeton*, *Chara)* (Holmes et al., 1995a). Water at the northern surficial lake outflow also has lower pH of 7.58 in an area with filamentous algae, where decaying vegetation promotes CO_2 production, which decreases pH and the $SI_{calcite}$ to favor $CaCO_3$ dissolution (Holmes et al., 1995a).

Fine-grained, high-Mg calcite marl precipitation in WGP is likely promoted by several processes (Street-Perrott et al., 1993; Holmes et al., 1995a). First, cooler groundwater (25°C) discharging into a warmer lake (28.5-31°C) degasses CO_2, which raises the lake water pH above 8 (Holmes et al., 1995a). As pH transitions above 7.5 in Jamaican karstic lakes, $SI_{calcite}$ exceeds 0 and calcium carbonate precipitation is favored (Holmes et al., 1995a). Second, in alkaline waters with pH>8 and low $CO_{2\,(aq.)}$,

submerged macrophytes (e.g., *Chara*, *Potamogeton*) can directly use HCO_3^- in photosynthesis. This process raises the pH of water, increases its alkalinity, and promotes $CaCO_3$ precipitation by increasing the $SI_{calcite}$ (i.e., biogenic decalcification of spring water). Lacustrine marl deposition is mediated by the concentration of dissolved ions in lake water (Street-Perrott et al., 1993; Holmes et al., 1995a) impacted by 1) evaporation, 2) degassing of CO_2 of thermally distinct water bodies mixing, and 2) decalcification of freshwater through bicarbonate assimilation by submerged plants and algae.

There are at least two hypotheses that could be driving lacustrine marl precipitation within EMLD Pond from ~8290 to 1700 cal yr BP. First, air temperature at Abaco in the mid-Holocene could have been warmer, promoting a more isothermal sinkhole and consistent degassing of CO_2, similar to conditions in the late Quaternary in WGP (Holmes et al., 1995a). Second, increased rainfall discharge rates (assuming that the freshwater meteoric lens on the carbonate platform is saturated with respect to HCO_3^-) would result in consistent bicarbonate concentration, promoting assimilation by plants and algae. It is possible that these conditions are not mutually exclusive, and aquatic conditions and the subsequent sedimentation at EMLD pond were influenced by climate. These conditions do not exist in the basin today, as recent hydrographic monitoring suggests that pH is too low (**Fig. 3:3**), and water column temperature at the sediment water interface is too variable (**Fig. 3:4**) for the precipitation of lacustrine marl.

The consistent accumulation of lacustrine marl for ~6600 years suggests an extended period of homogeneity in basin hydrography that is that is not often documented in

Holocene records from sinkhole lakes. Many factors can impact stratigraphic variability within coastal sinkholes, including sea level change, coastal positioning, water level depth to bedrock, sinkhole diameter, openness to sunlight, and karst conduit geometry (Whitaker and Smart, 1997). In Cenote Jennifer in Cuba (Peros et al., 2017), relative sea level forced a water level increase, increasing connectivity with the saline aquifer, and impacted a transition in stratigraphy from lacustrine marl to organic-rich sediment. Fine grained carbonate (marl) deposition promoted by shifts in rainfall and hydrology has been documented in the coastal karst lakes of Pacific islands (Trichet et al., 2001), but also in inland karst lakes with clastic influence in the Iberian Peninsula (Valero-Garcés et al., 2014). On Abaco, there are three basins (Freshwater River Blue Hole, No Man's Land sinkhole, and Great Cistern sinkhole) that record stratigraphic variability relative to regional hydrodynamic change during the mid-Holocene, synchronous with the deposition of marl in Emerald Pond. Variable lacustrine marl and sapropel deposition was recorded within Freshwater River (on the coast) ~7600 to 4100 cal yr BP, relative to establishment of a water column and aquifer recharge until conditions became persistently marine after 3200 cal yr BP (van Hengstum et al. 2020). Shallow conditions within No Man's Land sinkhole (inland) supported lacustrine/palustrine carbonate marl deposition from ~6500 cal yr BP to 3300 cal yr BP, perhaps influenced by expansion of a meteoric lens from increased local rainfall. A transition to algal sapropel deposition at ~3300 cal yr BP was likely due to a contracted meteoric lens in the basin driven by a decrease in regional rainfall and resultant drought (van Hengstum et al. 2018).

The transition from carbonate marl to sapropel observed in EMLD RP5 would suggest that the limnology of EMLD Pond fundamentally changed at ~1700 cal yr BP. Sapropel is fine grained, amorphous organic remains that can be sourced from algae, bacteria, or degraded terrestrial/aquatic plants (Schnurrenberger et al., 2003). The deposition of sapropel would suggest enhanced *in situ* production or OM accumulating within the basin, leading to more OM degradation, increased CO_2, and lower pH (more acidic conditions). Increased water level (as low as <1 m) can promote stratified conditions (van Hengstum et al., 2020), or increase light availability and *in situ* biological productivity (Gregory, 2016) within a sinkhole, and result in sapropel deposition. Characterization of sapropel organic matter deposited throughout much of the Holocene in Mangrove Lake, Bermuda suggests that algal sapropel can be deposited in both freshwater and marine conditions (Hatcher et al., 1982). Conditions supporting sapropel deposition can be influenced by sea level forcing water level to rise in the basin, and it can accumulate as a laminated or homogenous sedimentary deposit, characterized by a variety of specific organic compound classes (e.g., carbohydrates) and stable isotopic compositions that reflect aquatic conditions in which it was produced (Hatcher et al., 1982). More enriched stable isotopic compositions ($\delta^{13}C_{org}$) and C:N <12 represent a transition to marine conditions at Mangrove Lake (Hatcher et al., 1982), while depleted stable isotopic compositions and C:N < 18 in a sapropel deposited over the last ~6500 years in the Carwash Cave System, Mexico suggests a freshwater algal source (van Hengstum et al., 2010). The presence of bivalves (freshwater pea calms) within the sapropel unit at EMLD Pond (**Fig. 3:6F**) would suggest fresh conditions in

the basin at that time. Modern conditions at EMLD do not currently support the continuous deposition of algal sapropel, which might reflect instability of the water column and the sensitivity of autochthonous sediment production to aquatic change within these basins.

3.5.2. Hydroclimate Evidence from Leaf Wax Geochemistry

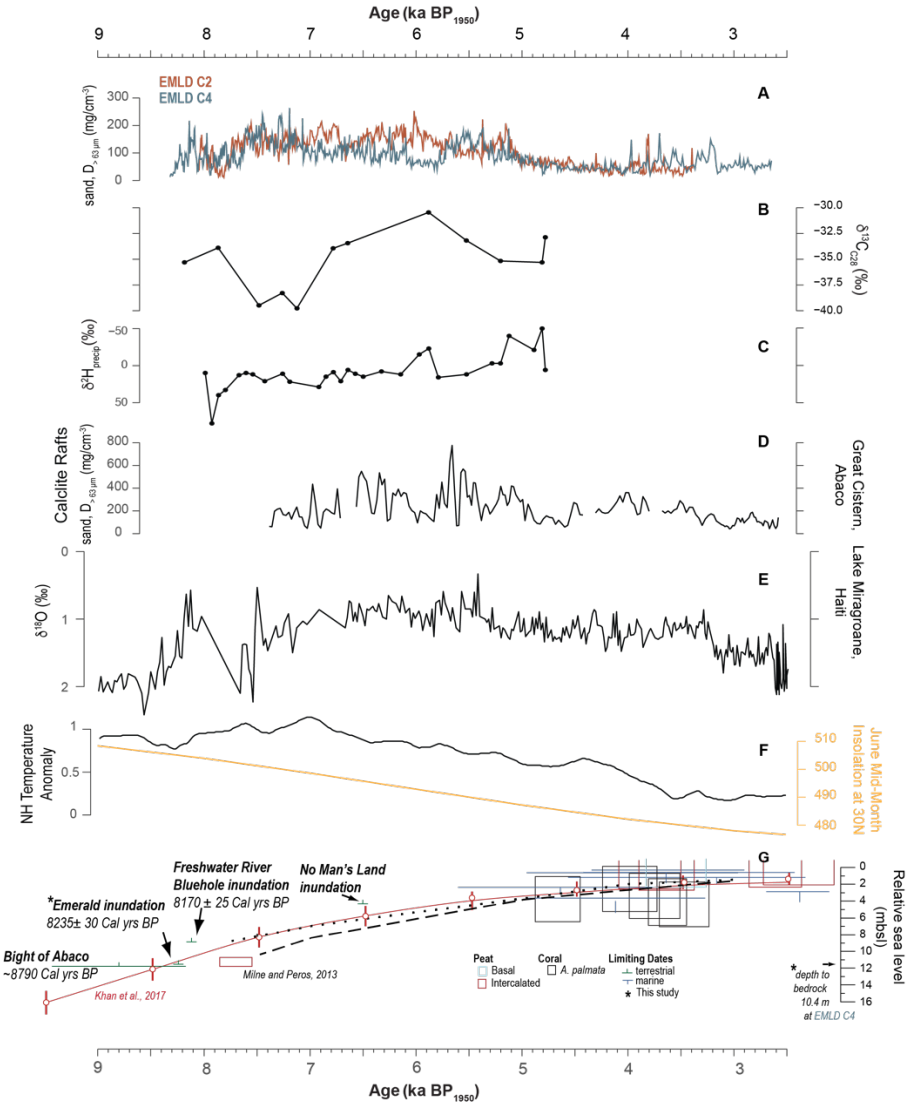

Figure 3:11: Regional comparison of hydroclimate records, sea level, and North Atlantic climatic conditions.

A-C) coarse grained particle deposition (D> 63µm) for EMLD C2 (brown) and EMLD C4 (blue), downcore $\delta^{13}C_{28}$ from EMLD C4, and reconstructed $\delta^{2}H_{precip}$ (this study), D) evidence for hydroclimate variability (calcite rafts) reconstructed from Great Cistern, Abaco (Sullivan et al., 2021, accepted), E) $\delta^{18}O$ values from a single species of ostracode *(Candona* sp.) from Lake Miragoane, Haiti (Hodell et al., 1991), F) Northern to Southern Hemisphere Temperature Anomaly (Schneider et al., 2014) (black line), and the mid-month (June) insolation at 30°N (orange line) (Berger and Loutre, 1991), and G) evidence for relative sea-level rise in the region based on indicators and resultant sea level curve from (Neumann and Land, 1975; Rasmussen et al., 1990; Khan et al., 2017; van Hengstum et al., 2018; van Hengstum et al., 2020)

The main feature of the $\delta^{2}H_{precip}$ reconstructed across ~8300 to 4700 cal yr BP EMLD pond is more depleted values (up to ~27 ‰) suggesting increased rainfall in the mid-Holocene (~6000 to 4800 cal yr BP), which is consistent within another regional record (Hodell et al., 1991). These reconstructed values align with recorded $\delta^{2}H_{precip}$ from the Havana CPHR GNIP station, which ranges from –66.3 to 20.6‰, and are therefore theoretically possible. Mean climatological seasonality of $\delta^{2}H_{precip}$ ranges from –15.2 to –3.5 ‰ (Tamalavage et al., 2020) making the range of variability recorded in sediments (~110‰) surprising given the considerable temporal averaging of sediments, with a single sample expected to integrate ~12 years. We find values of $\delta^{2}H_{precip}$ are relatively consistent from ~8000 to 6100 cal yr BP (mean= –13.7 ‰ ± 6‰), in comparison to generally more depleted values suggesting increased rainfall from ~6000 to 4800 cal yr BP (mean= –40.1 ‰ ± 22‰). Simulations from the isotope enabled Community Earth System Model indicate that ^{2}H-depleted rainfall corresponds to a weak NASH (lower central pressure, and western boundary displaced to the East) (Tamalavage et al., 2020). The implications are that EMLD pond records evidence for a more eastern position of the NASH from ~6000 to 4800 cal yr BP.

Vegetation can also modulate the leaf wax hydrogen isotope rainfall proxy. We therefore analyze the carbon isotopic composition in the same molecules to screen for the potentially confounding effects of vegetation change. We detect a shift to more enriched $\delta^{13}C_{28}$ values starting at ~6900 cal yr BP, with the most enriched value (–30 ‰) at ~6000 cal yr BP (**Fig. 3:12B**). These enriched $\delta^{13}C$ values, characteristic of open canopy woodlands or conifers (Diefendorf and Freimuth, 2017), are consistent with pollen evidence for increased *Pinus* and palm species after ~6300 cal yr BP (Slayton, 2010). In addition, we note that variability in $\delta^{13}C_{28}$ may be explained by varied inputs from the diverse pollen preserved in EMLD from ~7000 to 6500 cal yr BP (Slayton, 2010). $\delta^{2}H_{28}$ is stable from ~6900 to 6000 cal yr BP when $\delta^{13}C_{28}$ values shift, which means $\delta^{2}H_{28}$ is likely reflecting hydrologic change, rather than vegetation shifts. One concern, is the possibility of pre-aging of leaf waxes on the landscape, by storage in soils (Freimuth et al., 2021), or potentially during groundwater transport through channels in karstic landscapes (Douglas et al., 2012). In which case, the leaf wax record may be temporally offset from the dated terrestrial plant macrofossils upon which the age model is based (**Fig. 3:9**). However, given the small catchment contributing to EMLD Pond OM, we discount that possibility here. We interpret the leaf wax reconstruction of $\delta^{2}H_{precip}$ along with stratigraphic evidence and comparison to other basins as evidence that it was wetter during the mid-Holocene at Abaco.

Similarly, two Holocene hydroclimate reconstructions using stable isotopes ($\delta^{18}O$) measured on ostracodes from a lake core retrieved from Haiti (Hodell et al., 1991), and calcite rafts indicating more positive regional water balance (Sullivan et al., 2021)

document wetter conditions from ~6000 to 4800 cal yr BP (**Fig. 3:12 D, E**). These changes are coeval with the decrease in NH summer insolation (**Fig. 3:12G**). Paleoclimate reconstructions in the tropical North Atlantic have been used to infer the behavior of the ITCZ over centennial and millennial timescales (Hodell et al., 1995; Haug et al., 2001; Lane et al., 2011), as it is a major driver of hydroclimate variability in the Yucatan, Central America, and the northern part of the South American continent. In contrast, NASH variability is the dominant regulator of regional rainfall in the northern IAS (Li et al., 2012), but the behavior of the NASH on paleoclimate timescales is less understood, in part because available paleoclimate records are currently lacking. The geochemical proxies preserved within EMLD provide additional evidence for a wetter mid-Holocene in the Caribbean, supporting previous evidence from Haiti (Hodell et al., 1991).

Most current generation climate models suggest that the region should be drier (especially in boreal summer) during the mid-Holocene (6000 cal yr BP) (Brierley et al., 2020). This climate model-paleoclimate data discrepancy could result from a number of issues inherent to simulating the climate of the mid-Holocene. For instance, at ~6000 cal yr BP, climate models underestimate the extent of the West African Monsoon (WAM) (Braconnot et al., 2007), in part, because of issues capturing the "Green Sahara" or African Humid Period (Gasse, 2000). Improved simulations of the WAM tied to including vegetation feedbacks and changes to the dust aerosol forcing during the mid-Holocene (Pausata et al., 2016), and improved paleoclimate records (Shanahan et al., 2015; Tierney et al., 2017) have narrowed this discrepancy. A strengthened WAM has

connections to ENSO (Pausata et al., 2017) and hurricane activity (Dandoy et al., 2021) in the mid-Atlantic, both of which are likely to be relevant to Caribbean hydroclimate. The impacts of the WAM on the NASH, however, is not fully understood. Nevertheless, there is a likely link between the strength and extent of the NH monsoons and NASH position, through stationary wave dynamics (e.g. (Mantsis et al., 2013; Kelly et al., 2018)). As the NASH regulates rainfall in the northern IAS, further work on constraining NASH behavior during the mid-Holocene, its link to the NH monsoon systems, and the role for orbital forcing in driving these changes may address the discrepancy between climate model and proxy records. Additional high-resolution sedimentary records from this region will help to inform the regional hydroclimate history for comparison with climate models.

3.6. Conclusions

- A basal deposit of peat forming *in-situ* at EMLD pond represents a terrestrially limiting sea level indicator, and aligns with regional estimates of Holocene sea level rise.
- At ~8290 cal yr BP, lacustrine marl starts precipitating within EMLD pond, homogeneously depositing until ~1700 cal yr BP, while other basins in Abaco are recording stratigraphic variability. This suggests that water chemistry, level, and accommodation space within EMLD pond remain uniquely consistent throughout the mid-Holocene. Modern conditions (pH < 8) no longer promote the deposition of lacustrine marl.

- A recovered sapropel deposit from ~ 1700 to 1400 cal yr BP, taken on the northeastern periphery of the basin, provides evidence for hydrodynamically sensitive conditions including water level variability (potentially as little as <1 m), an increase in biological productivity and chemical change (decreased pH) within the lake.
- A decrease in reconstructed δ^2H_{precip} from terrestrial leaf waxes (*n*-alkanoic acids) ~6000 to 4800 cal yr BP suggests a wetter mid-Holocene, aligning with nearby hydroclimate records.

3.7. References

Beddows, P.A., Smart, P.L., Whitaker, F.F., Smith, S.L., 2007. Decoupled fresh–saline groundwater circulation of a coastal carbonate aquifer: spatial patterns of temperature and specific electrical conductivity. Journal of Hydrology 346, 18-32.

Berger, A., Loutre, M.-F., 1991. Insolation values for the climate of the last 10 million years. Quaternary Science Reviews 10, 297-317.

Blaauw, M., Christen, J.A., 2011. Flexible paleoclimate age-depth models using an autoregressive gamma process. Bayesian analysis 6, 457-474.

Black, M., 1932. VI. The algal sediments of Andros Island, Bahamas. Philosophical Transactions of the Royal Society of London. Series B, Containing Papers of a Biological Character 222, 165-192.

Boardman, M.R., Neumann, A., Rasmussen, K., Year. Proceedings of Proc. Fourth Symposium on the Geology of the Bahamas, Bahamian Fieldstation, Fort Lauderdale, pp. 45-52.

Braconnot, P., Otto-Bliesner, B., Harrison, S., Joussaume, S., Peterchmitt, J.-Y., Abe-Ouchi, A., Crucifix, M., Driesschaert, E., Fichefet, T., Hewitt, C., 2007. Results of

PMIP2 coupled simulations of the Mid-Holocene and Last Glacial Maximum–Part 2: feedbacks with emphasis on the location of the ITCZ and mid-and high latitudes heat budget. Climate of the Past 3, 279-296.

Brierley, C.M., Zhao, A., Harrison, S.P., Braconnot, P., Williams, C.J., Thornalley, D.J., Shi, X., Peterschmitt, J.-Y., Ohgaito, R., Kaufman, D.S., 2020. Large-scale features and evaluation of the PMIP4-CMIP6 midHolocene simulations. Climate of the Past 16, 1847-1872.

Carew, J.L., Mylroie, J.E., 1997. Geology of the Bahamas, in: Vacher, L., Quinn, T. (Eds.), Geology and Hydrogeology of Carbonate Islands, Developments in Sedimentology. Elsevier Science Publishers, Amsterdam, pp. 91-139.

Dandoy, S., Pausata, F.S., Camargo, S.J., Laprise, R., Winger, K., Emanuel, K., 2021. Atlantic hurricane response to Saharan greening and reduced dust emissions during the mid-Holocene. Climate of the Past 17, 675-701.

Diefendorf, A.F., Freimuth, E.J., 2017. Extracting the most from terrestrial plant-derived n-alkyl lipids and their carbon isotopes from the sedimentary record: A review. Organic Geochemistry 103, 1-21.

Donnelly, J.P., Woodruff, J.D., 2007. Intense hurricane activity over the past 5,000 years controlled by El Niño and the West African monsoon. Nature 447, 465.

Douglas, P.M., Pagani, M., Brenner, M., Hodell, D.A., Curtis, J.H., 2012. Aridity and vegetation composition are important determinants of leaf-wax δD values in southeastern Mexico and Central America. Geochimica et Cosmochimica Acta 97, 24-45.

Estep, M.F., Hoering, T.C., 1980. Biogeochemistry of the stable hydrogen isotopes. Geochimica et Cosmochimica Acta 44, 1197-1206.

Fall, P.L., van Hengstum, P.J., Lavold-Foote, L., Donnelly, J.P., Albury, N.A., Tamalavage, A.E., 2021. Human arrival and landscape dynamics in the northern Bahamas. Proceedings of the National Academy of Sciences 118.

Feakins, S.J., Bentley, L.P., Salinas, N., Shenkin, A., Blonder, B., Goldsmith, G.R., Ponton, C., Arvin, L.J., Wu, M.S., Peters, T., West, A.J., Martin, R.E., Enquist, B.J., Asner, G.P., Malhi, Y., 2016a. Plant leaf wax biomarkers capture gradients in hydrogen isotopes of precipitation from the Andes and Amazon. Geochimica et Cosmochimica Acta 182, 155-172.

Ficken, K.J., Li, B., Swain, D., Eglinton, G., 2000. An n-alkane proxy for the sedimentary input of submerged/floating freshwater aquatic macrophytes. Organic geochemistry 31, 745-749.

Freeman, K.H., Pancost, R., 2013. Biomarkers for terrestrial plants and climate, Treatise on Geochemistry: Second Edition. Elsevier Inc., pp. 395-416.

Freeman, K.H., Pancost, R., 2014. Biomarkers for Terrestrial Plants and Climate. ElSevier. Report.

Freimuth, E.J., Diefendorf, A.F., Lowell, T.V., Schartman, A.K., Landis, J.D., Stewart, A.K., Bates, B.R., 2021. Centennial-scale age offsets of plant wax n-alkanes in Adirondack lake sediments. Geochimica et Cosmochimica Acta 300, 119-136.

Gabriel, J.J., Reinhardt, E.G., Peros, M.C., Davidson, D.E., van Hengstum, P.J., Beddows, P.A., 2009. Palaeoenvironmental evolution of Cenote Aktun Ha (Carwash) on the Yucatan Peninsula, Mexico and its response to Holocene sea-level rise. Journal of Paleolimnology 42, 199-213.

Gamble, D.W., Curtis, S., 2008. Caribbean precipitation: review, model and prospect. Progress in Physical Geography 32, 265-276.

Gasse, F., 2000. Hydrological changes in the African tropics since the Last Glacial Maximum. Quaternary Science Reviews 19, 189-211.

Gehrels, W.R., 1999. Middle and late Holocene sea-level changes in eastern Maine reconstructed from foraminiferal saltmarsh stratigraphy and AMS 14C dates on basal peat. Quaternary Research 52, 350-359.

Giannini, A., Kushnir, Y., Cane, M.A., 2000. Interannual variability of Caribbean rainfall, ENSO, and the Atlantic Ocean. Journal of Climate 13, 297-311.

Gregory, 2016. The Influence of Morphology on Sinkhole Sedimentation at Little Salt Spring, Florida. Journal of Coastal Research.

Grimm, E.C., Jacobson, G.L., Watts, W.A., Hansen, B.C., Maasch, K.A., 1993. A 50,000-year record of climate oscillations from Florida and its temporal correlation with the Heinrich events. Science 261, 198-200.

Hastenrath, S., 1976. Variations in low-latitude circulation and extreme climatic events in the tropical Americas. Journal of Atmospheric Sciences 33, 202-215.

Hatcher, P.G., Simoneit, B.R., Mackenzie, F.T., Neumann, A.C., Thorstenson, D.C., Gerchakov, S.M., 1982. Organic geochemistry and pore water chemistry of sediments from Mangrove Lake, Bermuda. Organic Geochemistry 4, 93-112.

Haug, G.H., Hughen, K.A., Sigman, D.M., Peterson, L.C., Rohhl, U., 2001. Southward migration of the intertropical convergence zone through the Holocene. Science 293, 1304-1308.

Hayes, J., Freeman, K.H., Popp, B.N., Hoham, C.H., 1990. Compound-specific isotopic analyses: a novel tool for reconstruction of ancient biogeochemical processes. Organic Geochemistry 16, 1115-1128.

Heiri, O., Lotter, A.F., Lemcke, G., 2001. Loss on ignition as a method for estimating organic and carbonate content in sediments: reproducibility and comparability of results. Journal of paleolimnology 25, 101-110.

Herrera, D.A., Ault, T.R., Fasullo, J.T., Coats, S.J., Carrillo, C.M., Cook, B.I., Williams, A.P., 2018. Exacerbation of the 2013–2016 Pan-Caribbean Drought by Anthropogenic Warming. Geophysical research letters 45, 10,619-610,626.

Hodell, D.A., Curtis, J.H., Brenner, M., 1995. Possible role of climate in the collapse of Classic Maya civilization. Nature 375, 391-394.

Hodell, D.A., Curtis, J.H., Jones, G.A., Higuera-Gundy, A., Brenner, M., Binford, M.W., Dorsey, K.T., 1991. Reconstruction of Caribbean climate change over the past 10,500 years. Nature 352, 790.

Holmes, J., Street-Perrott, F., Darbyshire, D., Davies, N., Hales, P., 1995a. Chemical and isotopic composition of karstic lakes in Jamaica, West Indies. Hydrobiologia 312, 121-138.

Holmes, J.A., Street-Peffott, F.A., Ivanovich, M., Peffott, R.A., 1995b. A late Quaternary palaeolimnological record from Jamaica based on trace-element chemistry of ostracod shells. Chemical Geology 124, 143-160.

Jury, M., Malmgren, B.A., Winter, A., 2007. Subregional precipitation climate of the Caribbean and relationships with ENSO and NAO. Journal of Geophysical Research: Atmospheres 112.

Karnauskas, K.B., Schleussner, C.-F., Donnelly, J.P., Anchukaitis, K.J., 2018. Freshwater stress on small island developing states: population projections and aridity changes at 1.5 and 2 C. Regional environmental change 18, 2273-2282.

Kelly, P., Kravitz, B., Lu, J., Leung, L.R., 2018. Remote drying in the North Atlantic as a common response to precessional changes and CO2 increase over land. Geophysical Research Letters 45, 3615-3624.

Keyser, D., 1978. OSTRACODA (CRUSTACEA) FROM SOUTH-WEST FLORIDA. Aspects of ecology and zoogeography of recent and fossil Ostracoda, 207.

Keyser, D., Schöning, C., 2000. Holocene ostracoda (crustacea) from Bermuda. Senckenbergiana lethaea 80, 567-591.

Khan, N.S., Ashe, E., Horton, B.P., Dutton, A., Kopp, R.E., Brocard, G., Engelhart, S.E., Hill, D.F., Peltier, W., Vane, C.H., 2017. Drivers of Holocene sea-level change in the Caribbean. Quaternary Science Reviews 155, 13-36.

Kjellmark, E., 1996. Late Holocene climate change and human disturbance on Andros Island, Bahamas. Journal of Paleolimnology 15, 133-145.

Kovacs, S.E., van Hengstum, P.J., Reinhardt, E.G., Donnelly, J.P., Albury, N.A., 2013. Late Holocene sedimentation and hydrologic development in a shallow coastal sinkhole on Great Abaco Island, The Bahamas. Quaternary International 317, 118-132.

Lane, P., Donnelly, J.P., Woodruff, J.D., Hawkes, A.D., 2011. A decadally-resolved paleohurricane record archived in the late Holocene sediments of a Florida sinkhole. Marine Geology 287, 14-30.

Lee, H., Feakins, S.J., Lu, Z., Schimmelmann, A., Sessions, A.L., Tierney, J.E., Williams, T.J., 2017. Comparison of three methods for the methylation of aliphatic and aromatic compounds. Rapid Communications in Mass Spectrometry 31, 1633-1640.

Leng, M.J., Jones, M.D., Frogley, M.R., Eastwood, W.J., Kendrick, C.P., Roberts, C.N., 2010. Detrital carbonate influences on bulk oxygen and carbon isotope composition of lacustrine sediments from the Mediterranean. Global and Planetary Change 71, 175-182.

Li, L., Li, W., Kushnir, Y., 2012. Variation of the North Atlantic subtropical high western ridge and its implication to Southeastern US summer precipitation. Climate Dynamics 39, 1401-1412.

Li, W., Li, L., Fu, R., Deng, Y., Wang, H., 2011. Changes to the North Atlantic subtropical high and its role in the intensification of summer rainfall variability in the southeastern United States. Journal of Climate 24, 1499-1506.

Little, S.N., van Hengstum, P.J., 2019. Intertidal and subtidal benthic foraminifera in flooded caves: Implications for reconstructing coastal karst aquifers and cave paleoenvironments. Marine Micropaleontology 149, 19-34.

Magaña, V., 2005. Temporal evolution of summer convective activity over the Americas warm pools. Geophysical Research Letters 32.

Mantsis, D.F., Clement, A.C., Kirtman, B., Broccoli, A.J., Erb, M.P., 2013. Precessional cycles and their influence on the North Pacific and North Atlantic summer anticyclones. Journal of climate 26, 4596-4611.

Martin, E.R., Schumacher, C., 2011. The Caribbean low-level jet and its relationship with precipitation in IPCC AR4 models. Journal of Climate 24, 5935-5950.

Martin, J.B., Gulley, J., Spellman, P., 2012. Tidal pumping of water between Bahamian blue holes, aquifers, and the ocean. Journal of Hydrology 416-417, 28-38.

Martinez, C., Goddard, L., Kushnir, Y., Ting, M., 2019. Seasonal climatology and dynamical mechanisms of rainfall in the Caribbean. Climate dynamics 53, 825-846.

Milne, G.A., Peros, M., 2013. Data-model comparison of Holocene sea-level change in the circum-Caribbean region. Global and Planetary Change 107, 119-131.

Mylroie, J.E.C., James L.; Moore, Audra I. , 1995. Blue Holes: Definition and Genesis. Carbonates and Evaporites 10, 225-233.

Neumann, A.C., Land, L.S., 1975. Lime mud deposition and calcareous algae in the Bight of Abaco, Bahamas; a budget. Journal of Sedimentary Research 45, 763-786.

Park Boush, L.E., Myrbo, A., Michelson, A., 2014. A qualitative and quantitative model for climate-drive lake formation on carbonate platforms based on examples from the Bahamian archipelago. Carbonates and Evaporites 29, 409-418.

Pausata, F.S., Messori, G., Zhang, Q., 2016. Impacts of dust reduction on the northward expansion of the African monsoon during the Green Sahara period. Earth and Planetary Science Letters 434, 298-307.

Pausata, F.S., Zhang, Q., Muschitiello, F., Lu, Z., Chafik, L., Niedermeyer, E.M., Stager, J.C., Cobb, K.M., Liu, Z., 2017. Greening of the Sahara suppressed ENSO activity during the mid-Holocene. Nature communications 8, 1-12.

Pełechaty, M., Pukacz, A., Apolinarska, K., Pełechata, A., Siepak, M., 2013. The significance of Chara vegetation in the precipitation of lacustrine calcium carbonate. Sedimentology 60, 1017-1035.

Peros, M., Collins, S., G'Meiner, A.A., Reinhardt, E., Pupo, F.M., 2017. Multistage 8.2 kyr event revealed through high-resolution XRF core scanning of Cuban sinkhole sediments. Geophysical Research Letters 44, 7374-7381.

Rasmussen, K.A., Haddad, R.I., Neumann, A.C., 1990. Stable-isotope record of organic carbon from an evolving carbonate banktop, Bight of Abaco, Bahamas. Geology 18, 790-794.

Reeder, S.L., Rankey, E.C., 2009. Controls on morphology and sedimentology of carbonate tidal deltas, Abacos, Bahamas. Marine Geology 267, 141-155.

Reimer, P.J., Austin, W.E., Bard, E., Bayliss, A., Blackwell, P.G., Ramsey, C.B., Butzin, M., Cheng, H., Edwards, R.L., Friedrich, M., 2020. The IntCal20 Northern Hemisphere radiocarbon age calibration curve (0–55 cal kBP). Radiocarbon 62, 725-757.

Richards, D.A., Smart, P.L., Edwards, R.L., 1994. Maximum Sea Levels for the Last Glacial Period from U-Series Ages of Submerged Speleothems. Nature 367, 357-360.

Schneider, T., Bischoff, T., Haug, G.H., 2014. Migrations and dynamics of the intertropical convergence zone. Nature 513, 45-53.

Schnurrenberger, D., Russell, J., Kelts, K., 2003. Classification of lacustrine sediments based on sedimentary components. Journal of Paleolimnology 29, 141-154.

Sessions, A., TW, B., A, S., Hayes, J., 1999. Fractionation of hydrogen isotopes in lipid biosynthesis. Organic Geochemistry 30, 1193-1200.

Shanahan, T.M., McKay, N.P., Hughen, K.A., Overpeck, J.T., Otto-Bliesner, B., Heil, C.W., King, J., Scholz, C.A., Peck, J., 2015. The time-transgressive termination of the African Humid Period. Nature Geoscience 8, 140-144.

Shinn, E.A., Reich, C.D., Locker, S.D., Hine, A.C., 1996. A giant sediment trap in the Florida Keys. Journal of Coastal Research, 953-959.

Slayton, I.A., 2010. A vegetation history from Emerald Pond, Great Abaco Island, the Bahamas, based on pollen analysis.

Smart, P.L., Beddows, P.A., Coke, J., Doerr, S., Smith, S., Whitaker, F.F., 2006. Cave development on the caribbean coast of the Yucatan Peninsula, Quintana Roo, Mexico. SPECIAL PAPERS-GEOLOGICAL SOCIETY OF AMERICA 404, 105.

Spellman, P., Pritt, A., Salazar, N., 2021. Tracking changing water budgets across the bahamian archipelago. Journal of Hydrology, 126178.

Steadman, D.W., Albury, N.A., Maillis, P., Mead, J.I., Slapcinsky, J., Krysko, K.L., Singleton, H.M., Franklin, J., 2014. Late-Holocene faunal and landscape change in the Bahamas. The Holocene 24, 220-230.

Steadman, D.W., Franz, R., Morgan, G., Albury, N.A., Kakuk, B., Broad, K., Franz, S.E., Tinker, K., Pateman, M.P., Lott, T.A., Jarzen, D.M., Dilcher, D.L., 2007. Exceptionally well preserved late Quaternary plant and vertebrate fossils from a blue hole on Abaco, The Bahamas. Proceedings of the National Academy of the Sciences 104, 19897-19902.

Sternberg, L.d.S.L., 1988. D/H ratios of environmental water recorded by D/H ratios of plant lipids. Nature 333.

Street-Perrott, F., Hales, P., Perrott, R., Fontes, J.C., Switsur, V., Pearson, A., 1993. Late Quaternary palaeolimnology of a tropical marl lake: Wallywash Great Pond, Jamaica. Journal of Paleolimnology 9, 3-22.

Sullivan, R.M., van Hengstum, P.J., Donnelly, J.P., Winkler, T., Mark, S.E., Albury, N., 2020. Absolute and relative dating of human remains in a Bahamian sinkhole (Great Cistern, Abaco). Journal of Archaeological Science: Reports.

Surić, M., Juračić, M., Horvatinčić, N., Bronić, I.K., 2005. Late Pleistocene–Holocene sea-level rise and the pattern of coastal karst inundation: records from submerged speleothems along the Eastern Adriatic Coast (Croatia). Marine Geology 214, 163-175.

Tamalavage, A.E., van Hengstum, P.J., Louchouarn, P., Fall, P.L., Donnelly, J.P., Albury, N.A., Coats, S., Feakins, S.J., 2020. Plant wax evidence for precipitation and vegetation change from a coastal sinkhole lake in the Bahamas spanning the last 3000 years. Organic Geochemistry 150, 104120.

Tamalavage, A.E., van Hengstum, P.J., Louchouarn, P., Molodtsov, S., Kaiser, K., Donnelly, J.P., Albury, N.A., Fall, P.L., 2018. Organic matter sources and lateral sedimentation in a Bahamian karst basin (sinkhole) over the late Holocene: Influence of local vegetation and climate. Palaeogeography, Palaeoclimatology, Palaeoecology 506, 70-83.

Teeter, J.W., Year. Proceedings of Pleistocene and Holocene carbonate environments on San Salvador Island, Bahamas: International Geological Congress, 28th, Washington, Field Trip Guidebook T 175, pp. 35-40.

Tierney, J.E., Pausata, F.S.R., deMenocal, P.B., 2017. Rainfall regimes of the Green Sahara. Science Advances 3, e1601503.

Törnqvist, T.r.E., González, J.L., Newsom, L.A., Van der Borg, K., De Jong, A.F., Kurnik, C.W., 2004. Deciphering Holocene sea-level history on the US Gulf Coast: A high-resolution record from the Mississippi Delta. Geological Society of America Bulletin 116, 1026-1039.

Toscano, M.A., Macintyre, I.G., 2003. Corrected western Atlantic sea-level curve for the last 11,000 years based on calibrated 14 C dates from Acropora palmata framework and intertidal mangrove peat. Coral reefs 22, 257-270.

Trichet, J., Défarge, C., Tribble, J., Tribble, G., Sansone, F., 2001. Christmas Island lagoonal lakes, models for the deposition of carbonate–evaporite–organic laminated sediments. Sedimentary Geology 140, 177-189.

Tyson, R.V., Pearson, T.H., 1991. Modern and ancient continental shelf anoxia: an overview. Geological Society, London, Special Publications 58, 1-24.

Valero-Garcés, B., Morellón, M., Moreno, A., Corella, J.P., Martín-Puertas, C., Barreiro, F., Pérez, A., Giralt, S., Mata-Campo, M.P., 2014. Lacustrine carbonates of Iberian Karst Lakes: sources, processes and depositional environments. Sedimentary Geology 299, 1-29.

Van Hengstum, P., Reinhardt, E., Beddows, P., Huang, R., Gabriel, J., 2008. Thecamoebians (testate amoebae) and foraminifera from three anchialine cenotes in Mexico: Low salinity (1.5–4.5 psu) faunal transitions. The Journal of Foraminiferal Research 38, 305-317.

van Hengstum, P.J., Bernhard, J.M., 2016. A new species of benthic foraminifera from an inland Bahamian carbonate marsh. The Journal of Foraminiferal Research 46, 193-200.

van Hengstum, P.J., Donnelly, J.P., Fall, P.L., Toomey, M.R., Albury, N.A., Kakuk, B., 2016. The intertropical convergence zone modulates intense hurricane strikes on the western North Atlantic margin. Scientific Reports 6, 1-10.

van Hengstum, P.J., Maale, G., Donnelly, J.P., Albury, N.A., Onac, B.P., Sullivan, R.M., Winkler, T.S., Tamalavage, A.E., MacDonald, D., 2018. Drought in the northern Bahamas from 3300 to 2500 years ago. Quaternary Science Reviews 186, 169-185.

van Hengstum, P.J., Reinhardt, E.G., Beddows, P.A., Gabriel, J.J., 2010. Linkages between Holocene paleoclimate and paleohydrogeology preserved in a Yucatan underwater cave. Quaternary Science Reviews 29, 2788-2798.

van Hengstum, P.J., Scott, D.B., Gröcke, D.R., Charette, M.A., 2011. Sea level controls sedimentation and environments in coastal caves and sinkholes. Marine Geology 286, 35-50.

van Hengstum, P.J., Winkler, T.S., Tamalavage, A.E., Sullivan, R.M., Little, S.N., MacDonald, D., Donnelly, J.P., Albury, N.A., 2020. Holocene sedimentation in a blue hole surrounded by carbonate tidal flats in The Bahamas: Autogenic versus allogenic processes. Marine Geology 419, 106051.

Walker, L.N., Mylorie, J.E., Walker, A.D., Mylroie, J.R., 2008. The caves of Abaco Island, Bahamas: keys to geologic timescales. Journal of Cave and Karst Studies 70, 108-119.

Wallace, E., Donnelly, J., van Hengstum, P., Wiman, C., Sullivan, R., Winkler, T., d'Entremont, N., Toomey, M., Albury, N., 2019. Intense hurricane activity over the past 1500 years at South Andros Island, The Bahamas. Paleoceanography and Paleoclimatology.

Wang, C., Enfield, D.B., Lee, S.-k., Landsea, C.W., 2006. Influences of the Atlantic warm pool on Western Hemisphere summer rainfall and Atlantic hurricanes. Journal of climate 19, 3011-3028.

Whitaker, F.F., Smart, P.L., 1997. Hydrogeology of Bahamian archipelago, in: Vacher, H.L., Quinn, T.M. (Eds.), Geology and hydrogeology of carbonate islands: Developments in Sedimentology 54. Elsevier Science Publishers, pp. 183-216.

Winkler, T.S., van Hengstum, P.J., Donnelly, J.P., Wallace, E.J., Sullivan, R.M., MacDonald, D., Albury, N.A., 2020. Revising evidence of hurricane strikes on Abaco Island (The Bahamas) over the last 700 years. Scientific reports 10, 1-17.

Zarikian, C.A.A., Swart, P.K., Gifford, J.A., Blackwelder, P.L., 2005. Holocene paleohydrology of Little Salt Spring, Florida, based on ostracod assemblages and stable isotopes. Palaeogeography, Palaeoclimatology, Palaeoecology 225, 134-156.

4. BIOMARKER MOLECULAR AND STABLE ISOTOPIC SIGNATURES OF PARTICULATE ORGANIC MATTER IN DEPTH PROFILES OF TWO STRATIFIED COASTAL SINKHOLES IN THE NORTHERN BAHAMAS

4.1. Introduction

The sediment records in sinkhole lakes (i.e., blue holes and cenotes) on carbonate landscapes provide an opportunity to complement, expand, and potentially calibrate the regional environmental and climate histories that are preserved by speleothem geochemical records ((e.g., (Filley et al., 2001; Huang et al., 2006; Gregory, 2016; Peros et al., 2017; van Hengstum et al., 2020)). Sinkhole lakes are flooded by density stratified aquifers, vertically characterized by an upper meteoric lens, a mixing zone of variable thickness, and a saline groundwater mass at depth (that is often anoxic). These physical conditions promote primary productivity in the pelagic zone (Sánchez et al., 2002) and organic matter (OM) preservation in accumulated sediments (Hatcher et al., 1982). Previous work in density stratified sinkhole lakes has investigated: particulate organic matter transformation (POM) along physicochemical gradients, sharp changes in redox potential, evidence for chemosynthesis, and complex microbial assemblages that vary relative to density stratification and water layer mixing (Humphreys, 1999; Socki et al., 2002; Seymour et al., 2007; Gonzalez et al., 2011; Haas et al., 2018; Ritter et al., 2019; Björnerås et al., 2020; Yao et al., 2020). However, understanding the physical and biological processes that generate and alter organic-based sediment deposits, like algal sapropels dominated by POM produced *in situ*, is required to accurately interpret their

preserved proxy records of environmental change (e.g., isotopic variability, biomarker concentrations).

Bulk OM properties (%OM, $\delta^{13}C$, $\delta^{15}N$, C:N) are commonly used for reconstructions of source inputs and environmental changes in productivity and/or watershed vegetation or land use changes (Lamb et al., 2006; Lone et al., 2018; Van Hardenbroek et al., 2018). However, because both aquatic production and landscape erosion contribute to bulk OM properties (Tamalavage et al., 2018; van Hengstum et al., 2018), such properties may not clearly resolve the source (aquatic vs. terrestrial) of POM archived in the sediment record, or its degradation via biogeochemical processes in the water column (Hedges et al., 1997; Arndt et al., 2013; Kharbush et al., 2020). Thus, there is interest in i) further resolving biogeochemical processes that could impact the transformation of POM in sinkhole water columns, and ii) analyzing biomarkers to more specifically characterize both water column POM and OM deposited within these systems.

In addition, within sinkhole lakes, POM is not only deposited but it is also exported into the adjacent ocean. For example, there are few rivers in karstic landscapes, and freshwater flows underground to the coast via submarine groundwater discharge (SGD). SGD from carbonate platforms accounts for 12% of global discharge to the ocean (Beck et al., 2013). SGD is a pathway for OM export: satellite imagery shows a plume emerging from Drinkwater Sinkhole on Abaco Island (The Bahamas) to the adjacent coastal ocean after the passage of Hurricane Dorian in 2019 (category 5 hurricane Saffir-Simpson Scale; see comparison between **Fig. 4:1A** and **Fig. 4:1B**).

Improving understanding of POM transformation and sedimentation within sinkhole lakes can thus better inform the use of sinkhole lake sediment records within paleoenvironmental research, and regional carbon cycling.

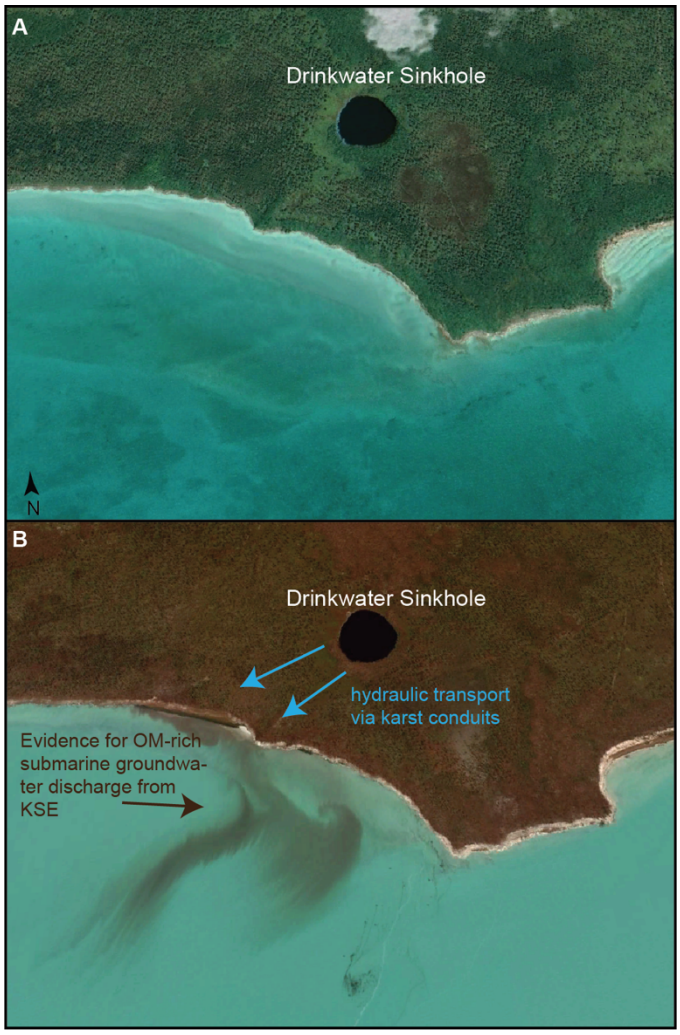

Figure 4:1: Sinkhole Export after Hurricane Dorian.
Satellite image (retrieved from Google Earth, 2021) of Drinkwater Sinkhole on Great Abaco (26.86°N, –77.62°W) Island on A) July, 13, 2019, and B) September, 6, 2019, after the landfall of Hurricane Dorian that remained at Category 5 while in place over the island from September 1–3, 2019.

In this study, we document the molecular, elemental, and isotopic signatures of POM in depth profiles of two density stratified sinkhole lakes (Blackwood and Drinkwater) on Great Abaco Island in The Bahamas, to investigate the biogeochemical processes impacting POM production and degradation in these systems. Specifically, we measured the carbon and nitrogen isotopic composition ($\delta^{13}C$ and $\delta^{15}N$, respectively), the atomic carbon to nitrogen ration (C:N), and the molecular abundances of glycerol diakyl glycerol tetraether lipids (GDGTs) in POM. We also measure the hydrogen ($\delta^{2}H$) and oxygen ($\delta^{18}O$) isotopic composition of water samples within the sinkhole. Finally, we compare the modern water column POM measurements to the preserved OM geochemical signatures within Blackwood Sinkhole, which has been the site of extensive previous research (van Hengstum et al., 2016; Tamalavage et al., 2018; Tamalavage et al., 2020; Fall et al., 2021).

4.2. Study Sites

The carbonate islands and shallow-water banks of The Bahamas cover 300,000 km^2 in the North Atlantic (Carew and Mylroie, 1997). The northern most carbonate platform is the Little Bahama Bank (26.79°N, 77.42°W) (**Fig. 4:2A**), which is made up of Grand Bahama and Great Abaco Island. Abaco is surrounded by the North Atlantic Ocean to the East, shallow waters separating it from Grand Bahama to the west (55 km), and the deep Northwest and Northeast Providence channels to the south (Carew and Mylroie, 1997; Walker et al., 2008). It is likely that the Bahamian carbonate bank began accumulating in the Late Jurassic, and the present positions of the banks and deep-water channels have been in place since the Late Cretaceous (Mullins and Lynts, 1977;

Sheridan et al., 1988; Carew and Mylroie, 1997). Banktop and periplatform carbonate sedimentation provides important analogs for marine carbonate deposition (Mullins and Neumann, 1979; Mullins et al., 1984; Burns and Neumann, 1987; Walker et al., 2008), and the thick, underlying carbonate deposits allow for exploration of sequence stratigraphy associated with glacioeustatic sea-level fluctuations (Walker, 2006). Subsurface dissolution and cave formation throughout Quaternary sea-level oscillations eventually caused surface collapse, and form sinkholes lakes which are now ubiquitous on the Bahamian karst landscape (Whitaker and Smart, 1997), and they provide accommodation space for subsequent sedimentation (Mylroie et al., 1995; Shinn et al., 1996). First-order water level variability within coastal sinkholes is directly tied to vertical migration of the coastal aquifer, which is ultimately driven by regional sea-level change (i.e., tides, glacioeustasy). Subtidal blue holes form when continued sea-level rise eventually submerges a coastal sinkhole (van Hengstum et al., 2011; Gregory, 2016).

Blackwood and Drinkwater are sinkhole lakes located on the subaerial landscape of Great Abaco Island on the eastern Little Bahama Bank (**Fig. 4:2**). Both sites are groundwater-fed basins with no fluvial inputs, and they both have proximal subsurface hydraulic connection to the adjacent coastal ocean (e.g., Drinkwater Sinkhole: Bight of Abaco, Blackwood Sinkhole: Abaco Sound). Blackwood is located 220 m from the windward shoreline, and it is bordered a wetland (e.g., mangroves, cattail) on its eastern periphery. It is 32 m in diameter with a water depth of 33 to 38 m below sea level (mbsl), and the local water level experiences ~1 m vertical fluctuation from tides

(Reeder and Rankey, 2009). In the subsurface, there is a secondary, cylindrical karst feature (water depth ~46–61 mbsl) that is connected to Blackwood Sinkhole through a cave tunnel at 32 mbsl, which currently has no subaerial expression (see Fig. 2 in (Tamalavage et al., 2018). Drinkwater Sinkhole is located 21 km north of Blackwood Sinkhole, and it is located ~500 m from the leeward shoreline within the Bight of Abaco. It has a diameter of 220 m, with a depth to the sediment-water interface of 60 m. In contrast to Blackwood Sinkhole, there are no wetlands on the epikarst surface adjacent to Drinkwater sinkhole, or anywhere nearby.

The stratigraphy preserved within Blackwood Sinkhole has greatly improved our interpretation of historical changes to Abaco climate and ecology over the last 3000 years. Coarse-grained overwash layers from hurricane strikes (van Hengstum et al., 2016), variable OM deposition (Tamalavage et al., 2018), proxies for hydroclimate (Tamalavage et al., 2020), and landscape shifts (Fall et al., 2021) have been analyzed from sediment cores collected in 2011 from the basin. Bulk OM geochemical proxies ($\delta^{13}C_{org}$, C:N) suggest that OM is primarily sourced from the surrounding terrestrial landscape from ~3000 to 1500 cal yr BP, with increasing contributions from water column primary productivity from 1500 to 1000 cal yr BP that are synchronous with more enriched $\delta^{2}H_{precip}$ values that are interpreted to represent drier conditions. Finally, evidence from bulk OM, compound specific biomarkers (leaf waxes), and pollen, indicate that inputs from the adjacent mangrove wetland dominate the preserved OM in Blackwood from ~1000 cal yr BP until present (Tamalavage et al., 2018; Tamalavage et al., 2020; Fall et al., 2021).

The paleoenvironmental history of Drinkwater Sinkhole is less known. However, a recent geophysical and sediment coring expedition to the sinkhole recovered >20 m of well preserved, laminated stratigraphy with high organic matter content. Preliminary results (van Hengstum et al., 2019) suggest that this sediment stratigraphy preserved within Drinkwater can provide a historical record of hydroclimate variability in the northern intra-American sea from the end of the last-Glacial period to present.

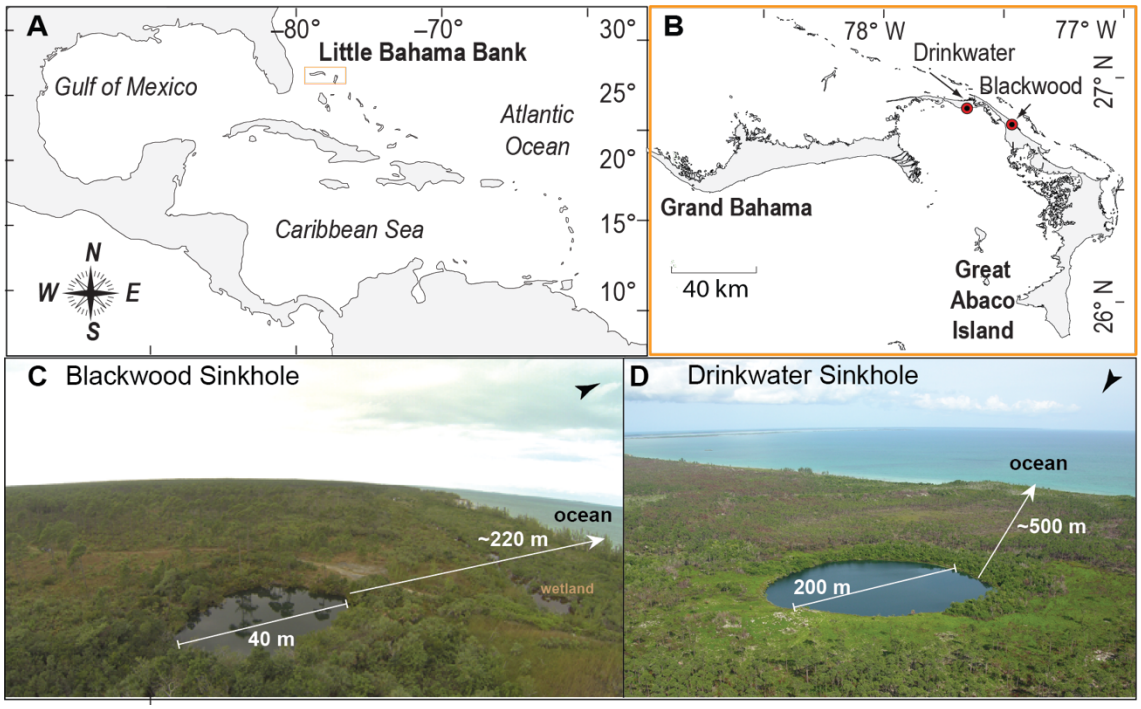

Figure 4:2: Map of Blackwood and Drinkwater.
A) Location of the Little Bahama Bank within the tropical North Atlantic, B) Inset of the Little Bahama Bank with Drinkwater and Blackwood Sinkholes on Great Abaco Island, C) aerial photo of Blackwood Sinkhole (photo credit: Pete van Hengstum), D) aerial photo of Drinkwater Sinkhole (photo credit: Nancy Albury).

4.3. Methods

4.3.1. Fieldwork and POM collection

Depth-wise hydrographic profiles were collected from both sites in multiple seasons spanning several years to better characterize water column variability (**Fig. 4:3**). Temperature (±0.01°C), salinity (±0.1 psu), pH (±0.1 pH units), dissolved oxygen (±0.1 mg L^{-1}), and depth (±0.004 m) were measured using a YSI EXO1 Multiparameter Sonde, with data collected at a sampling rate of two measurements per second. The multi-parameter probe was routinely calibrated before deployment, and the pH sensor was replaced nearly annually before fieldwork to promote accuracy in field measurements. Water samples were collected with a hand-deployed 5L Niskin bottle (General Oceanics) from the middle of both sinkholes (**Fig. 4:2**) using a portable raft on 25-27 November 2018 (Drinkwater) and 4 December 2018 (Blackwood). Collected water samples were to be evenly spaced within each stratified water mass (ca. ~3 m), with three samples taken within the meteoric lens (ML) and mixing zone (MZ), and five samples within the basal saline groundwater mass (SGW) (**Fig. 4:3**). Nine duplicate samples (four from Blackwood, and five from Drinkwater) were taken within each sinkhole for exploratory biomarker analysis. After deployment of the messenger, the Niskin bottle was brought aboard and collected into collapsible Nalgene 10 L carboy containers (previously acid rinsed), and then rinsed three times with the collected sample before storage. Re-used carboys were thoroughly rinsed with tap water, then sample water three times before re-use. After collection, water samples were kept in an insulated cooler, transported back to the field laboratory, and suspended particulate matter (SPM)

was collected via vacuum filtration within 12-24 hrs from collection. All equipment and was rinsed with tap water in the lab, then subsequently some of the sample water before filtration. Standard GF/F filters (Whatman, 42.5 mm diameter) were used to retain fine particles down to 0.7 μm. Before field deployment, filters were combusted at 450°C for 5.5 hours to remove any residual organics, weighed, and stored in plastic petri dishes for transport. Approximately 1 to 5 L of water was filtered onto the blank filter (or until filtration was no longer possible due clogged filter pores). SPM-laden filters were then immediately frozen, transported in insulated cool bags back to the home laboratory, and stored frozen upon arrival.

4.3.2. Water Isotopes

Samples for water isotopes were stored in 10 mL glass vials with a cone-shaped liner to restrict evaporation between sample and headspace and were stored at 4°C. Before analysis, samples were transferred into 2 mL glass autosampler vials using a glass pipette. Stable isotope analysis was performed using a Picarro L-2130i Cavity Ring Down Spectroscopy (CRDS) system, with vaporization module (A0211) coupled to a HTC-xt Leap Pal Technologies autosampler following standard methods (Walker et al., 2016). The vaporizer operated at 110°C. Five standards were used for analytical calibrations (two international, three internal lab). The two international standards used were Vienna Standard Mean Ocean Water (VSMOW certified $\delta^{18}O$ value = 0‰, $\delta^{2}H$ = 0‰), and Greenland Ice Sheet Precipitation (GISP certified $\delta^{18}O$ value = −24.96‰, $\delta^{2}H$ = −189.5‰) purchased from IAEA. The internal laboratory standards used were: tap water, Evian French Alps Spring Water and Arctic River Mix, calibrated internally

against the international standards. Each sample was injected 12 times, discarding the first three injections of each sample due to potential carry over. The data are reported in the standard delta notation in per mil (‰, deviation from VSMOW). Calibrations for $\delta^{18}O$ and $\delta^{2}H$ were determined using analyzed and known values for VSMOW and GISP. Each water column sample was analyzed in replicate, with the first three injections discarded during data processing. One of the five standards were analyzed between each sample for reproducibility. Uncertainty between analyzed standards and known calibrations was less than 1.6‰ for $\delta^{18}O$ and 5.4‰ for $\delta^{2}H$.

4.3.3. Stable Isotope Analysis of POM

Suspended particulate matter laden filters (e.g., unacidified filtered particulates) were immediately weighed while wet. The filter was then cut in half and one half was reserved for future biological analysis, while the remaining half was freeze-dried for stable isotope analysis (this study). The concentration of SPM in mg/L was calculated by taking the weight of the dried half, multiplying it by a factor of two (estimated as the whole filter), and subtracting the mass of the empty whole filter, and dividing the resultant mass (in mg) by the total volume of water filtered (L) at each depth. The half filters were then sent to the University of Alaska Fairbanks stable isotope facility for $\delta^{13}C$, $\delta^{15}N$, and C:N analysis on acidified SPM (hereafter referred to as POM) to address POM source origin (Peters et al., 1978; O'Leary, 1988; Meyers, 1994). Filters were exposed to concentrated hydrochloric acid within a desiccator for 4 hrs. Sample was scraped from filter, and using internal protocols, stable isotopic ratios were measured by Elemental Analyzer Isotope Ratio Mass Spectrometry (EA-IRMS) using a Thermo

Fisher Scientific Elemental Analyzer (Flash 2100) combined with a Thermo Fisher Scientist DeltaV^{Plus} isotope ratio mass spectrometer and a Conflo IV interface, and reported relative to international standards in standard isotopic notation (relative to Vienna Pee Dee Belemnite for carbon, and atmospheric nitrogen) as parts per mil (‰). Reproducibility of isotope analysis was within 0.3‰ for $\delta^{15}N$ and 0.1‰ for $\delta^{13}C$. Mass spectrometry was used to determine C and N content during combustion for atomic C:N ratio determination (each element normalized to their atomic weight). The fractions of %N and OC% on the acidified filters were estimated using the determined weight of both N and C (in µg) during combustion on the whole filter, over the estimated dry weight of the whole filter. The sample at 2 m in Blackwood had an elemental response of C and N that was higher in mass than the estimated mass of particulates on the whole filter, while the sample at 22 m in Drinkwater had an elemental response lower than the estimated mass of particulates on the whole filter. Estimates of OC% at Blackwood 2 m and Drinkwater 22 m are therefore not reported or used within normalization of biomarker concentration (discussed below), but isotopic values and biomarker ratios were likely not impacted by the mass error.

4.3.4. Biomarker Analyses of POM

POM samples from the water column in both Blackwood (n = 4) and Drinkwater (n = 5), and sediment samples from Blackwood (n = 6) and Drinkwater (n = *6*) were selected for analysis of glycerol dialkyl glycerol tetraethers (GDGTs), which are sourced from microbial membrane lipids. Lipids (full GF/F filter, or 1−2 g dry weight of sediment) were extracted with an Accelerated Solvent Extraction system (ASE 350®,

DIONEX) with 9:1 ratio of dichloromethane (DCM):methanol (MeOH) at 100˚C and 1500 psi (2 x 15-min). The extract was separated using column chromatography (5 cm x 40 mm Pasteur pipette, NH_2 Sepra brand bulk packing, 60 Å), eluting with 2:1 DCM:isopropanol, followed by 4% HCO_2H in diethyl ether, yielding neutral and acid fractions respectively. The neutral fraction was separated by column chromatography (5 cm x 40 mm Pasteur pipette, 5% water-deactivated silica gel, 100–200 mesh) with DCM and methanol to elute GDGTs. The GDGT fractions were filtered through a 0.45 µm polytetrafluoroethylene filter. GDGTs were injected into an Agilent 1260 High-Performance Liquid Chromatograph (HPLC) coupled to an Agilent 6120 mass spectrometer, and separated using two Ethylene Bridged Hybrid (BEH) Hydrophilic Interaction (HILIC) silica columns (2.1 mm X 150 mm, 1.7 µm; Waters). Isoprenoidal and branched GDGTs were detected in single ion monitoring mode and quantified to a C_{46} internal standard.

The number of cyclopentane and cyclohexane ring moieties within the lipid membranes of marine archaea (GDGTs) are responsive to sea water temperature (Schouten et al., 2002) using the ratio:

$$TEX_{86} = \frac{[GDGT-2]+[GDGT-3]+[Cren']}{[GDGT-1]+[GDGT-2]+[GDGT-3]+[Cren']} \quad (1)$$

Marine (isoprenoidal) GDGTs are primarily sourced from nitrifying *Thaumarchaetoa* (Damsté et al., 2002; Pester et al., 2011), and while GDGTs from *Thaumarchaeota* have also been used within lakes (Powers et al., 2004), the calibrations for both marine and

lacustrine environments are similar. Although terrestrial sinkholes are meromictic lake-like environments, they are marine influenced systems due to their coastal proximity, high porosity of antecedent carbonate, and hydraulic connectivity to the adjacent ocean. Thus, TEX_{86} is applied with the BAYSPAR calibration (Tierney and Tingley, 2015), using the standard mode SST model (bayspar_tex.m) with a prior standard deviation of 10°C (https://github.com/jesstierney/BAYSPAR). The standard mode BAYSPAR SST model assumes that oceanographic conditions are similar to today and uses mean SST observations (prior mean) either from the closest data point or within 500 km (whichever dataset is larger). Average SST calculated from gridded NOAA datasets at 29°N, 84°W-23°N, 75°W is 26.1°C (Sullivan, personal communication), which is similar to the prior mean annual SST output by bayspar_tex.m (27.7°C), and mean annual sinkhole surface temperatures in Blackwood and Drinkwater (25.9°C and 26.3°C, respectively).

The weighted average of ring numbers in the compound distribution can inform community-level producers, defined as the Ring Index (Zhang et al., 2016). Non-thermal impacts on GDGTs can bias TEX_{86} results, such as from GDGTs transported from soils or in situ sedimentary production, and result in RI > 0.3 (Zhang et al., 2016). The Ring Index (RI) can be calculated as:

$$\mathrm{RI} = 0\,[\mathrm{GDGT}-0] + 1\,[\mathrm{GDGT}-1] + 2\,[\mathrm{GDGT}-2] + 3\,[\mathrm{GDGT}-3] + 4\,[\mathrm{Cren}] + 4\,[\mathrm{Cren}'] \quad (2)$$

and assess deviation from the distributions in which the temperature proxy has been developed using (Zhang et al., 2016), in which:

$$\Delta RI = RI_{TEX} - RI_{Sample} \quad (3)$$

Methanogenic *Euryarchaeota* can also produce cyclic GDGTs and these can be expected in the anoxic saline groundwater mass of sinkholes. We therefore calculate the Methane Index (MI, range of 0 to 1) to quantify the contribution of methanotrophic *Euryarchaeota* to that of non-methanotrophic *Crenarchaeota.* MI values below ~0.3 generally indicate normal aerobic marine conditions, while values above ~0.3 can indicate environments impacted by anoxic methane oxidation (Zhang et al., 2011). The MI is calculated by:

$$MI = \frac{([GDGT-1]+[GDGT-2]+[GDGT-3])}{([GDGT-1]+[GDGT-2]+[GDGT-3]+[Cren]+[Cren')} \quad (4)$$

We also calculate abundance of branched GDGTs (brGDGTs) that can be found in terrestrial organic matter, including peat and soil, but can additionally be produced within lakes and/or rivers (Damsté et al., 2000; Hopmans et al., 2004; Weijers et al., 2006; Tierney and Russell, 2009). The branched and isoprenoidal tetraether (BIT) index was developed to measure an index of terrestrial to aquatic production, where non-isoprenoidal GDGTs (I,II,II) are derived from terrigenous organisms (Schouten et al., 2000; Hopmans et al., 2004). We determine the BIT index as:

$$BIT = \frac{([I]+[II]+[III])}{([I]+[II]+[III]+[IV])} \quad (6)$$

and report this, together with the summed brGDGTs (ΣbrGDGTs) and summed isoGDGTs (ΣisoGDGTs) to track changing terrestrial and aquatic production. BIT values of >0.4 could be representative of samples impacted by terrestrial inputs (Weijers et al., 2006). Summed ΣbrGDGTs and ΣisoGDGTs were normalized to organic carbon by dividing the concentration of GDGTs (µg/g) by the estimated weight percent of OC%. Water column biomarker samples were separate from the samples for stable isotopic analysis, so results for elemental analysis (and stable isotopes) of the equivalent sample depth were used as an estimate (excluding Blackwood 2 m and Drinkwater 22 m). Sedimentary GDGTs for Blackwood were normalized to OC% at equivalent core depths using values published within (Tamalavage et al., 2018).

Finally, we also calculate the Archaeol Caldarchaeol Ecometric (ACE) index, first proposed by (Turich and Freeman, 2011) to quantify the production of halophilic archaea and to that of *Euryarchaeota* and *Thaumarchaeota* where:

$$ACE = \frac{[archaeol]}{[archaeol+caldarchaeol]} \text{ x } 100 \quad (7)$$

The ACE proxy has been calibrated in the context of evaporation and salinity, and has been applied to the Messinian Salinity Crisis, where ACE values in SPM below 50 range from ~5 to 25 (Turich and Freeman, 2011). It has been tested in terrestrial lakes ranging

from freshwater to saline, performing best above 20 psu, in which higher ACE values were significantly correlated to higher salinity (Wang et al., 2013; He et al., 2020). For example, lake water salinities below 10 ppt have ACE values < 50, while salinities from 50-100 ppt have ACE values >70 (He et al., 2020). It has also been applied to reconstruct salinity variations recorded in the sediments of saline to hypersaline lakes (Feakins et al., 2019; Peaple et al., 2021). Here, the ACE Index is tested for its ability to document fresh to hypersaline conditions based on the POM collected from sinkhole water columns.

4.4. Results

4.4.1. Sinkhole Hydrography

The water column in both sinkholes is stratified into three layers from the local coastal aquifer: i) an upper meteoric lens (ML), ii) a transitional mixing zone (MZ) and iii) the basal saline groundwater mass (SGW) (**Fig. 4:3**). The MZ is often simplified as just a halocline in unconfined coastal karst aquifers between the ML and SGW. However, the MZ is more technically a physical layer of complex mixing between the isohaline or isothermal values of the ML and SGW and key area of biogeochemical interactions (Beddows et al., 2007), including the trapping and alteration of POM within the stratified system.

The ML at Blackwood is from 0 to 7 mbsl, and characterized by a low oligohaline salinity (mean: 2.0 ± 0.3 psu). Variability in the depth of the ML between casts may be related to differences in tidal position of the water table at the time of the

cast (not corrected for in **Fig: 4:3**), or may suggest time periods when the ML is thicker in response to local precipitation (e.g., January 2017). Boreal summer surface temperatures are 27.4 ± 2.0 °C, which is ~4°C warmer than winter temperatures (22.6 ± 0.6 °C), with lower dissolved oxygen by ~2 mg/L in the ML during the summer months (**Fig. 4:3**). There is a more distinctive thermocline in Blackwood from ~7 to 11 m in boreal winter, until isothermal temperatures (mean: 24.7 ± 0.1 °C) are reached in the SGW below 19 m. The pH of the ML is higher in the winter (January casts, 7.9 ± 0.2) versus the summer (July casts, 7.6 ± 0.5). We define the MZ in Blackwood from 7 to 19 m, wherein dissolved oxygen concentrations sharply decrease and decline with depth until anoxic conditions (<0.2 mg/L) are reached below ~18 mbsl. The pH also declines from >7.7 to ~7.2 in the MZ. Salinity is 35.1 ± 1.8 psu below 19 mbsl in the SGW, but salinity does not become completely isohaline within the SGW in Blackwood. Instead, salinity gradually increases with depth to the sediment-water interface.

The ML in Drinkwater is defined as the upper 10 m of the water column, which has a salinity of 10.5 ± 0.3 psu (brackish, mesohaline) and is stable seasonally (at constant depth). Boreal summer surface temperatures are 30.9 ± 0.7 °C, which is ~8°C warmer than winter temperatures (23.8 ± 0.8 °C). Surface dissolved oxygen concentrations have a seasonal range from 7.8 to 8.2 mg/L in the ML (**Fig. 4:3**). We define the MZ in Drinkwater MZ from 10 to 27 based on (i) temperature variability (non-isothermal) with increasing depth from 10 to ~27 m, and (ii) slight salinity variability (non-isohaline) below ~14 m. In summer, there is a thermocline (cooling) between 0 and 7 m, whereas in winter the thermocline inverts and there is a warming between 10−17 m. The pH

decreases from 8.3 ± 0.1 in the ML to ~7 at 22 m, with an increase back to ~7.7 at 20 m. Dissolved oxygen concentration sharply declines in the MZ, and becomes anoxic conditions occur below 21 mbsl in the SGW. The SGW at Drinkwater is isohaline (39.6 ± 0.3 psu) and isothermal (25.6 ± 0.2°C).

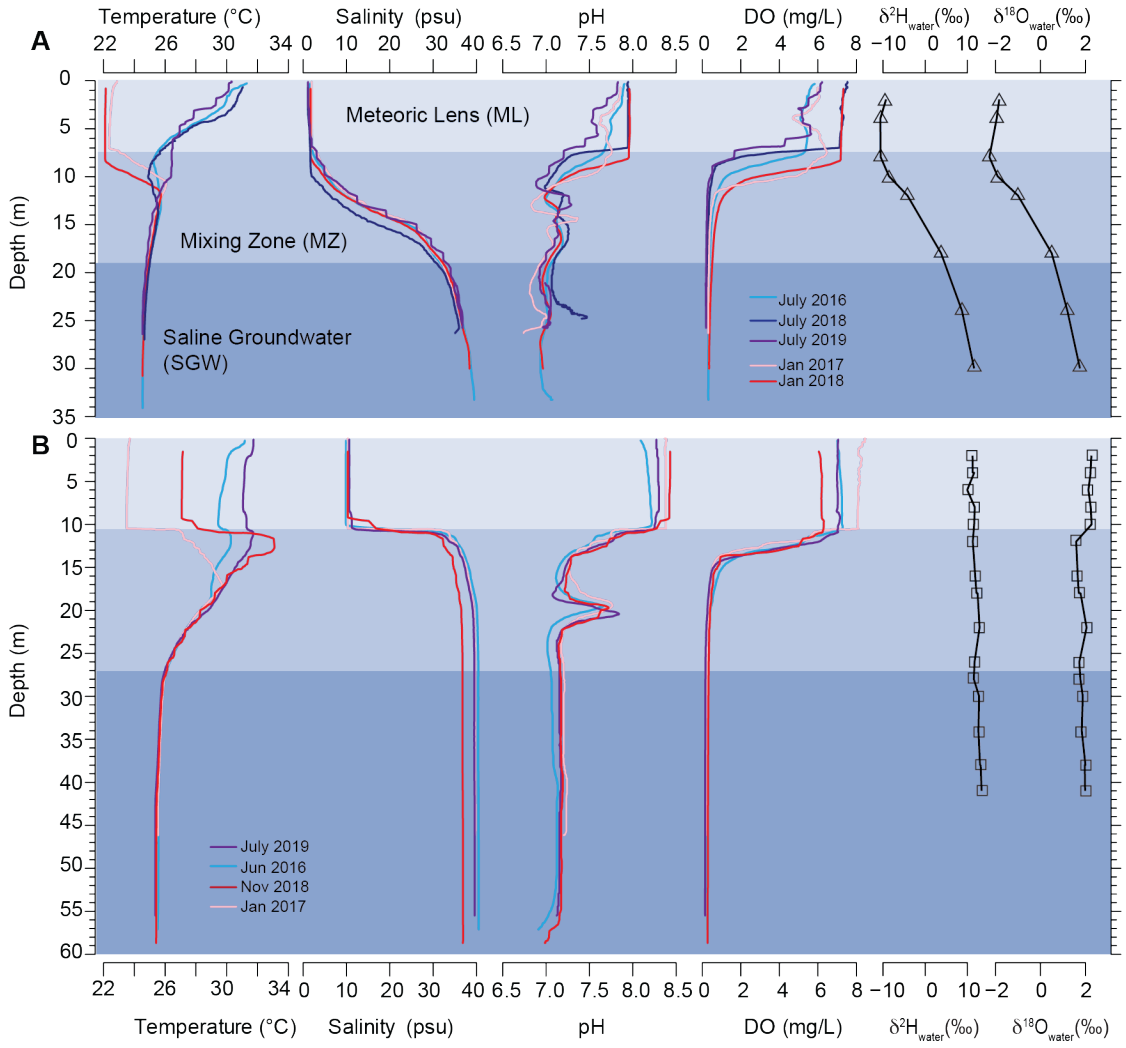

Figure 4:3: Seasonal water column profiles.
Panel A) Blackwood Sinkhole and Panel B) Drinkwater Sinkhole.
Water depths are reported relative to the water table at the time of the casts, and do not account for tidal variability in the local water table. Water samples retrieved by Niskin

bottle were measured for δ^2H_{water} and $\delta^{18}O_{water}$ (triangles: Blackwood, squares: Drinkwater).

In Blackwood, δ^2H_{water} and $\delta^{18}O_{water}$ values are most depleted in the freshwater or meteoric lens (**Fig. 4:3A**). The mean ML value is −2.0‰ for $\delta^{18}O_{water}$ and −10.3‰ for δ^2H_{water}, which approaches the isotopic composition of precipitation. For comparison, a precipitation isotope timeseries from the Cuba GNIP station yields weighted mean annual values ($\delta^{18}O_{precip}$= −2.4‰, δ^2H_{precip}= −11.8‰) (IAEA/WMO, 2019). The δ^2H (−4.0‰) and $\delta^{18}O$ (−2.1‰) value of a single sample of rain collected in November 2018 from Abaco is close to the Global Meteoric Water Line (GMWL) (Craig, 1961), and are isotopically similar to the composition of the Blackwood ML (**Fig. 4:4**). Below the ML, the isotopic compositions are more enriched with increased salinity towards that of seawater. δ^2H_{water} and $\delta^{18}O_{water}$ are at, or above 0‰ in the SGW (**Fig. 4:3A**). In contrast, the Drinkwater water column has a constant isotopic composition (**Fig. 4:4**) throughout the 0−40 m profile (mean $\delta^{18}O_{water}$ = −2.0‰ ± 0.3‰, and mean δ^2H_{water} = 11.5‰ ± 0.7‰). Drinkwater ML values are farthest from the GMWL (**Fig. 4:4**), which could be due to evaporation (Bowen et al., 2018). Evaporation on the ML at Drinkwater is also supported by the higher ML salinity in Drinkwater (~10 psu) versus Blackwood (~2 psu). Similar evaporative processes impacting $\delta^{18}O_{water}$ in a sinkhole lake were also observed in the northwest Yucatan (Hodell et al., 2005), but the sinkhole was also sensitive to large rainfall events (e.g., hurricanes) that depleted the $\delta^{18}O_{water}$ for months after impact (Hodell et al., 2005).

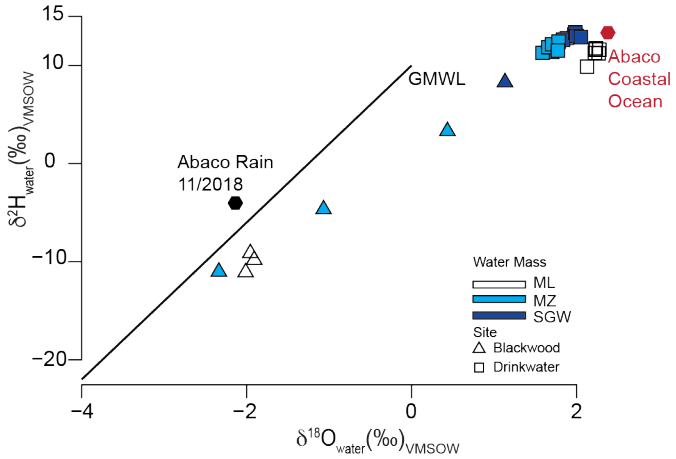

Figure 4:4: δ^2H and $\delta^{18}O$ of sinkhole water samples (Blackwood and Drinkwater). Coastal ocean (red), a singular rain event on Abaco (black), and the Global Meteoric Water Line (GMWL) included.

4.4.2. POM concentration and bulk geochemistry ($\delta^{13}C$, $\delta^{15}N$, C:N)

Simultaneous measurement of elemental C:N, $\delta^{13}C$, and $\delta^{15}N$ in organic matter is a common practice in ecological and geological studies. But, the acidification process can influence the $\delta^{15}N$ signal (Kennedy et al., 2005), and it can reduce the TN content (Lohse et al., 2000). Best practices include measuring TN and $\delta^{15}N$ on an untreated subsample, yet, acid type and strength and digestion method can reduce TN and $\delta^{15}N$ variability (Kennedy et al., 2005). Here, we include and interpret the N data as part of the multi-proxy dataset based on two factors: i) water column filters were treated via acid fumigation which has been observed to cause no significant variability in $\delta^{15}N$ between acidified and non-acidified samples (Kennedy et al., 2005), and ii) our analyzed values have consistently low (< 8) C:N ratios and estimates for N% that range from (0.1 to 2.5%), and perhaps are minimally affected by the small N loss that is possible during acidification.

In Blackwood, the MZ had the highest concentration of filtered suspended particulate matter (11.6 mg/L). OC% is highest (> 10%) at 4 m and 14 m, and in general, samples in the ML and MZ are more organic rich than the SGW (**Fig. 4:5A**). The color of filtered suspended particulate matter is tan in the ML and SGW, and pink to reddish brown across the MZ (**Fig. 4:5A**). There is a strong enrichment in $\delta^{13}C_{POM}$ values along the depth profile with the most depleted values within the ML (−36.5‰), and rapid shift to heavier values (−31‰) in the MZ, and a stabilization of heaviest values within the SGW (−29.3‰). C:N ratios are consistently below 9 across all water layers. $\delta^{15}N_{POM}$ values range between −0.9‰ and 3.3‰, and there is no clear pattern that aligns distinctly along physicochemical gradients across water layers.

In Drinkwater, the ML had the highest concentration of filtered suspended particulate matter (13.9 mg/L). The most organic rich sample (19.7% OC) is within the MZ at 18 m (**Fig. 4:5B**), and the ML and MZ have higher OC% than the SGW samples. Filtered suspended particulate matter is light tan within the ML and SGW, and is pink to dark purple around ~20 m in the MZ. In this water basin, the $\delta^{13}C_{POM}$ values also show a "step" enrichment with depth (occurring in the MZ and stabilizing in the SGW). The most depleted values of $\delta^{13}C_{POM}$ are within the ML (−27.8‰) and most enriched are within the SGW (−21.7‰) with the exception of a heavy signatures at 22 in the MZ (−20.5‰). C:N ratios within Drinkwater are below 9.5 except for the deepest surveyed samples (34, 38, and 41 m), which increase to 12.9 ± 0.9. There is a clear offset between more depleted $\delta^{15}N_{POM}$ values within the ML and upper MZ (mean: −2.1‰), in

comparison to the more enriched values of the lower MZ (>20 m) and SGW layer (mean: 2.1‰).

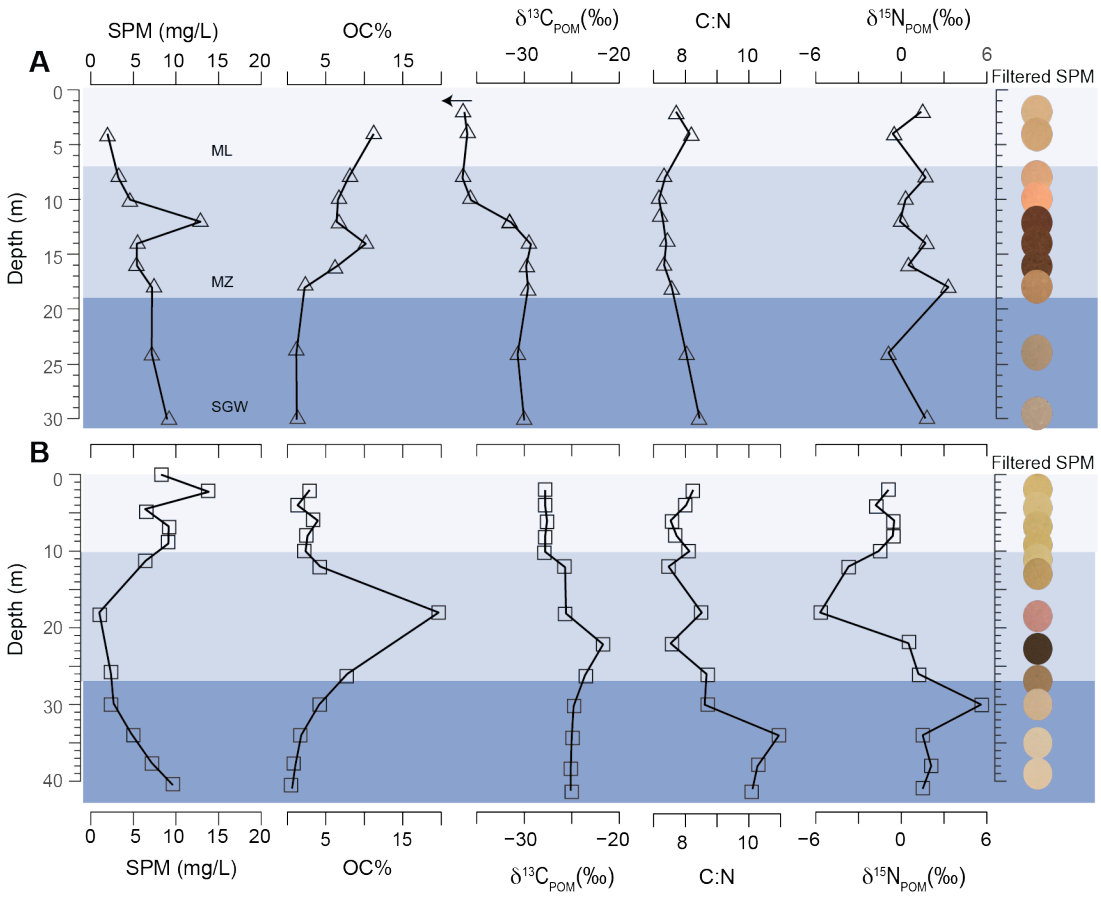

Figure 4:5: SPM/POM water column profiles from both basins.
Blackwood Sinkhole (triangles, A), and Drinkwater Sinkhole (squares, B) showing SPM concentration, OC%, $\delta^{13}C_{POM}$, C:N, $\delta^{15}N_{POM}$, and filtered SPM color based on photographs (unaltered color). Black arrow represents a value of POM initially surveyed from the upper 1 m of water in 2016 (−37.6‰). SPM: suspended particulate matter.

4.4.3. Biomarker GDGTs

ΣbrGDGTs within Blackwood POM range from 5.0 to 153.1 µg/gOC, and ΣisoGDGTs range from 4.6 to 60.9 µg/gOC. MI (0.3) and BIT (0.9) are lowest within the ML. The shallowest sample recording the ACE index is at the top of the MZ (33.1),

which correlates to lower salinity/contributions of archaeol (**Table 4.1**). MI, BIT and ACE increase with depth and salinity (0.5, 1, and >75, respectively). One sample at 4 m in Blackwood had low ΔRI and MI allowing for a viable calculation of sinkhole surface temperatures using TEX_{86}. The resulting predicted temperature of 26 ± 5°C falls within the range of measured winter (22.6 ± 0.6°C) and summer (27.4 ± 2.0 °C) temperatures of the ML from 0 to 7 m depth (**Fig. 4:3A**). Within the sediment core samples from Blackwood, ΣbrGDGTs range from 38.7 to 400.9 µg/gOC and ΣisoGDGTs range from 22 to 426.1 µg/gOC (**Table 4:2**). ACE values range from 5.9 to 23.3, getting higher into the saline water masses, representing greater influence from salinity-tolerant archaea (Wang et al., 2013; He et al., 2020). Four samples have low enough ΔRI, MI, and BIT to calculate TEX_{86}-based temperatures, which yield an estimate of 29 ± 1 (1σ, 4 samples) ± 6°C (calibration uncertainty), similar to summer ML values of 27.3 ± 2.0°C (**Fig. 4:3A**).

Table 4:1: Water column GDGTs.

Site	Depth (m)	MI	BIT	RI	ΔRI	ACE	ΣbrGDGTs µg/gOC	ΣisoGDGTs µg/gOC
Blackwood	4	0.3	0.9	2.4	0.3	--	65.9	9.6
Blackwood	8	0.5	0.9	1.1	0.6	33.1	57.4	33.4
Blackwood	12	0.4	0.9	0.5	--	85.8	5.0	4.6
Blackwood	24	0.5	1.0	0.6	1.77	74.9	153.1	60.9
Drinkwater	4	0.3	0.7	1.9	0.2	--	77.8	27.3
Drinkwater	16	0.3	0.8	1.0	--	--	0.5	5.8
Drinkwater	18	0.5	0.9	1.0	--	78.1	6.9	2.5
Drinkwater	22	0.7	0.9	0.4	--	87.6	--	--
Drinkwater	28	0.7	1.0	0.6	--	85.3	8.5	1.7
Drinkwater	38	0.6	1.0	0.5	1.4	79.5	54.4	2.1

GDGT concentrations in POM are generally lower in Drinkwater than Blackwood (**Table 4:1**). In Drinkwater, ΣbrGDGTs range from 0.5 to 54.4 µg/gOC, and

ΣisoGDGTs range from 1.7 to 60.9 µg/gOC. MI is lowest in the ML and records the same value (0.3) at 16 m (within the ML), whereas it increases to 0.7 at 28 m. ACE is lowest in the shallowest sample (18 m) in the MZ. BIT and ΔRI increase with depth along physicochemical gradients. In Drinkwater, only the sample at 4 m in the ML had GDGT distributions with low ΔRI, MI, and BIT that indicate that TEX_{86} could be used to estimate sinkhole surface temperatures. The reconstructed TEX_{86} temperature estimate was 15 ± 5°C, which is in the lower range of ML temperatures measured within the winter cast (23.6 ± 0.1°C) (**Fig. 4:3B**).

Table 4:2: Sedimentary GDGTs from Drinkwater Sinkhole

Site	Core	Total Depth (cm)	MI	BIT	RI	ΔRI	ACE	ΣbrGDGTs µg/gOC	ΣisoGDGTs µg/gOC
Blackwood	C2	4.5	0.2	0.8	1.6	1.3	15.6	178.1	89.4
Blackwood	C2	26.5	0.2	0.7	2.0	0.7	23.4	38.7	22.0
Blackwood	C2	36.5	0.3	0.5	2.9	0.1	0.9	264.8	289.6
Blackwood	C2	48.5	0.3	0.4	2.9	0.1	5.9	236.0	426.1
Blackwood	C2	95.5	0.2	0.6	2.8	0.1	15.6	82.6	67.0
Blackwood	C2	107.5	0.2	0.5	3.1	0.2	12.1	400.9	340.4
Drinkwater	C11	0.5	0.2	0.6	2.1	0.7	11.1	--	--
Drinkwater	C11	177.5	0.2	0.8	1.4	1.3	28.9	--	--
Drinkwater	C11	653.5	0.8	1	0.2	2.6	7.3	--	--
Drinkwater	C11	887.5	0.8	1	0.2	1.3	9.2	--	--
Drinkwater	C11	1167.5	0.3	0.9	1.3	1.4	18.8	--	--
Drinkwater	C11	1327.5	0.5	0.9	0.9	0.7	11.1	--	--

As there is currently no available sedimentary OC% for Drinkwater, ΣbrGDGTs and ΣisoGDGTs not normalized to OC. However, ΣbrGDGTs range from 5.4 to 26.6 µg/g and ΣisoGDGTs range from 2.6 to 38.3 µg/g. ΔRI from preserved sediments were all above 0.7, which likely reflects GDGT contributions from other sources (e.g., soils)

(Zhang et al., 2016). As a result, the GDGTs recovered from Drinkwater were not suitable for temperature estimates based on TEX_{86}. There are high BIT (> 0.8) and ΣbrGDGTs (mean 18.0 ± 9 µg/g) and variable MI (0.2 to 0.8), which provides biomarker evidence for mixed terrestrial and *in situ* POM (including influence from methanotrophic *Euryarchaeota*) in the preserved sedimentary OM (**Table 3**).

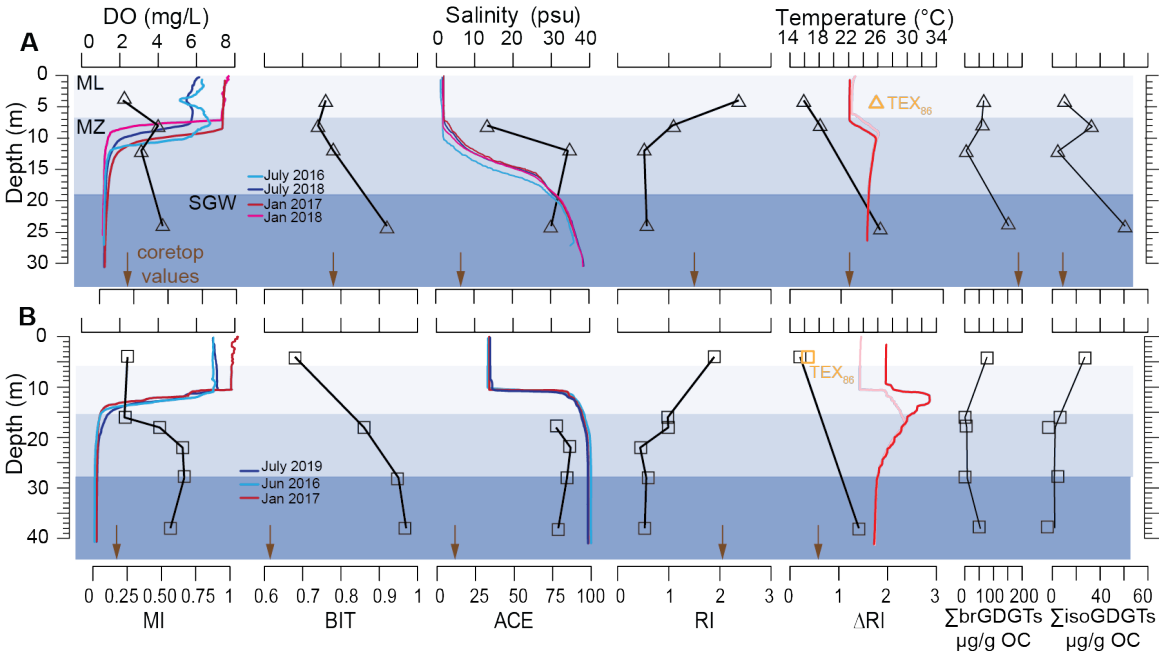

Figure 4:6: GDGT POM profiles.
Within A) Blackwood sinkhole (triangles) and B) Drinkwater sinkhole (squares) showing GDGT indices: MI=Methane Index, BIT=Branched and Isoprenoid Tetraether index, ACE= Archaeol Caldarchaeol Ecometric, RI=Ring Index, ΔRI=deviation from modern, global TEX_{86}-RI relationship, ΣbrGDGTs and ΣisoGDGTs. Yellow shapes represent TEX_{86} values viable for temperature reconstructions, and brown arrows are available core top values. For comparison, we show the measured DO (dissolved oxygen) with MI, salinity with ACE, and temperature with ΔRI from hydrographic casts within **Fig. 3**.

4.5. Discussion

4.5.1. Sinkhole Hydrographic Characteristics

Shifts in salinity and water isotopic composition point to density stratification at each site, but also show that site-specific hydrological processes are present in each system. Blackwood (on the windward coastline) shows more influence from coastal processes on the adjacent shoreline (e.g., additional physical mixing in the subsurface). Its ML appears to be actively discharging water replenished by regional rainfall, and the MZ and SGW experience more active physical mixing and destabilization from coastal processes at the adjacent shoreline (e.g. wave hydrodynamic and/or tidal "pumping"). In contrast, the Drinkwater ML is more evaporated (~10 psu) in the ML, whereas the SGW presents more physical stability from less mixing. For example, the water stable isotopic composition of the Blackwood ML resembles both collected island rainfall and the GNIP compiled value, while water from the SGW plots between the rain and coastal ocean value (**Fig. 4:4**), reflecting connectivity to the stratified coastal aquifer. In Drinkwater, the similarity of $\delta^{2}H_{water}$ and $\delta^{18}O_{water}$ values in the MZ and SGW to measured coastal ocean values provides evidence that it is indeed connected to the coastal ocean. This connectivity is further confirmed by satellite imagery showing POM export to the coast post Hurricane Dorian (**Fig. 4:1**). While Drinkwater could still be sensitive to aquifer recharge from precipitation due to the high porosity and permeability of the antecedent carbonate, it is seven times larger in diameter than Blackwood. This increased surface area may expose the ML to evaporative processes that perhaps dominate the isotopic signal. However, additional seasonal monitoring would be needed to fully resolve water balance between the atmosphere and sinkhole surface (Gibson et al., 2016), especially in a humid climate (Hua et al., 2019).

4.5.2. Sinkhole water column POM

$\delta^{13}C_{POM}$ and C:N in both sinkholes suggest that suspended POM is mainly sourced from *in-situ* production in the ML, with degraded POM in the MZ and SGW (**Fig. 4:5**). The $\delta^{13}C$ signature imparted to organic matter during either chemosynthesis or photosynthesis depends on the isotopic composition of assimilated carbon and the magnitude of the $\delta^{13}C$ shift (ε) that occurs during fixation (Degens, 1969; O'Leary, 1988). $\delta^{13}C$ values for marine or freshwater algae typically range from −33 to −16‰ with C:N ~5 to 10 (Lamb et al., 2006) (**Fig. 4:7A**), but freshwater phytoplankton in lacustrine lakes have been found to typically range from −35 to −23‰ and can be depleted up to −40‰ (France, 1995). Mean $\delta^{13}C_{POM}$ values and C:N ratios in Drinkwater ($\delta^{13}C_{POM}$: −25.8 ± 1.9‰; C:N: 7.9 ± 1.9) and Blackwood ($\delta^{13}C_{POM}$: −32.5 ± 3.1‰; C:N: 6.3 ± 0.7) are both consistent with expected signatures for algal-produced organic matter. However, the ~7‰ offset in $\delta^{13}C_{POM}$ values between the two sites point to site-specific processes which are impacting the POM produced *in situ*. The $\delta^{13}C$ values of POM can be influenced by multiple processes, such as surface water CO_2 concentrations and isotopic signatures (Hollander and McKenzie, 1991; Fogel et al., 1992), seasonal growth rate (Cifuentes et al., 1988; Lehmann et al., 2004; Gu et al., 2011), and biosynthesis fractionations by different producers (Wong and Sackett, 1978).

In both sinkhole lakes, there is a shift to more enriched $\delta^{13}C_{POM}$ in the MZ, which could represent decomposition of labile POM, mediated by the microbial community. This is similar to patterns of $\delta^{13}C_{POM}$ isotopic enrichment (−25‰ to −22‰) observed from the surface to the sulfidic zone within the Black Sea (Fry et al., 1991). In the Black

Sea, the shift to more enriched isotopic compositions are more similar to sinking phytoplankton and green sulfur bacteria, in comparison to depleted $\delta^{13}C$ values associated with chemosynthesis (Fry et al., 1991). Perhaps preferential degradation of specific isotopically light compounds is enriching stable isotopic compositions of suspended POM (Benner et al., 1991; Hedges et al., 1997; Kharbush et al., 2020). Within the ocean, POM is dominated by the bacterial community (Kaiser and Benner, 2008), with $\delta^{13}C$ compositions of bacteria typically ranging from −27‰ to −16‰, and C:N values ~5 to 7 (Lamb et al., 2006). These bacterial values are comparable to mean values found below the ML of both sinkholes, particularly in Drinkwater (−24.9 ± 2.3‰).

The dark purple/brown color of SPM found within the mixing zone of Drinkwater could provide evidence for sulfur oxidation and photosynthetic production below the ML. Similar colors were found on particulates filtered from the halocline of nearby Sawmill Sink during boreal summer (July) (Gonzalez et al., 2011). The bacteria found within the particulates from Sawmill Sink were dominated by the photoautotrophs *Chlorobi* that can oxide reduced sulfur compounds (Gonzalez et al., 2011). pH variability within Drinkwater and Blackwood is also comparable to values within Xcolac Cenote, Yucatan (Socki et al., 2002), in which a survey of sulfur species suggests a zone of sulfide oxidation (below the freshwater interface) and sulfate reduction zone along the stratified water column. The similar POM colors and pH variability to other surveyed sites would suggest that there is *in-situ* production even beyond the ML within Drinkwater and Blackwood. Although there are likely some sinking compounds that are not included within this suspended POM snapshot (Middelburg and Nieuwenhuize,

1998), the $\delta^{13}C$ and C:N signatures measured here are likely reflecting a combination of altered POM (sourced from POM produced *in situ* and terrestrial organic matter) and bacterial biomass.

The $\delta^{15}N$ values also suggest that in situ production of POM occurs in the ML, and that POM becomes increasingly degraded with depth. Light $\delta^{15}N_{POM}$ values in the ML of Drinkwater shift to more positive, heavier values along the depth profile. As phytoplankton assimilate lighter ^{14}N (through nitrogen fixation) during photosynthesis, more depleted $\delta^{15}N_{POM}$ values could be representative of primary production, while more enriched values could be indicative of selective mineralization processes during POM degradation (Altabet, 1988; Fogel and Cifuentes, 1993; Gu et al., 2006). Enriched $\delta^{15}N$ of organic matter has been documented in other aquatic basins (Fry et al., 1991; Lehmann et al., 2004), and could be attributed to denitrification (Saino and Hattori, 1987; Owens, 1988; Gu, 2009). Yet, determining N sources (e.g., through measuring NO_3^-, NO_2^-, NH_4^+) (Hadas et al., 2009) and measuring both suspended and sinking POM fractions (Altabet, 1988) would be necessary to resolve what N-cycle processes are impacting $\delta^{15}N_{POM,}$ Perhaps the see-saw variability of $\delta^{15}N_{POM}$ within Blackwood could be attributed to N flux across small scale gradients within the 30 m water column.

Water column GDGTs provide biomarker evidence for mixed source contributions from *in situ* productivity from different organisms in different water masses, inputs of terrestrially derived OM, and OM transformation (**Fig. 4:6**). While both sinkholes are surrounded by subtropical forests (Blackwood and Drinkwater), only Blackwood has wetlands with thick peat accumulations on its periphery. The higher

abundance of isoprenoidal GDGTs, which are from aquatic lipids produced *in situ,* in both sinkhole lakes suggests higher algal OM in the upper water column, versus decreased lower isoprenoidal GDGTs in the MZ and SGW. This interpretation is consistent with that inferred from stable isotopic signatures of POM in the surface and deep-water masses of each system. Branched GDGTs are also highest in the ML in comparison to the MZ and SGW, but BIT increases with depth, which suggests that isoprenoidal GDGTs from *in situ* aquatic lipids are no longer dominating. High BIT could indicate dominant terrestrial inputs to sinkhole POM. But, it remains difficult to distinguish the source of brGDGTs, as they can be sourced from the terrestrial environments, lake producers, or microbes (Damsté et al., 2018). As enriched $\delta^{13}C_{POM}$, $\delta^{15}N_{POM}$, and lower C:N values in the MZ suggest POM degradation by the microbial community, perhaps the increased BIT also reflects this process. Increased MI into the dysoxic to anoxic MZ and SGW suggest the influence from methanotrophic *Euryarchaeota* (Zhang et al., 2011). Evidence for the anaerobic oxidation of methane (AOM) have been similarly found in anoxic layers of the Black Sea and Cariaco Basin (Liu et al., 2014). ACE values are higher within the MZ and SGW within both basins, providing evidence of more hypersaline-tolerant archaeol in the higher-salinity SGW (Turich and Freeman, 2011). Lower BIT, low ΔRI (falling along the global calibration of TEX_{86}) (Zhang et al., 2016), and low MI (not dominated by methanotrophic *Euryarchaeota*) (Zhang et al., 2011) in one of the ML samples of both basins (4 m) were used for a sinkhole surface wintertime temperature reconstruction from TEX_{86}. Both fall within 7°C of instrumental values obtained during previous hydrographic surveys,

suggesting that TEX_{86} temperature reconstructions are viable within these systems. However, to fully assess the utility of TEX_{86} within these systems, additional samples and a survey of adjacent soils is required.

4.5.3. Sinkhole sediment core paleoenvironmental reconstructions

The characterization of water column POM provides an opportunity to re-evaluate bulk geochemical measurements archived in sedimentary OM within Blackwood Sinkhole spanning the last ~3000 years (van Hengstum et al., 2016; Tamalavage et al., 2018) (**Fig. 4:8).** $\delta^{13}C_{org}$ and C:N values of bulk OM values from ~3000 to 850 cal yr BP (mean $\delta^{13}C_{org}$: −30.3 ± 1.6‰) (**Fig. 4:8A**) were originally interpreted as sourced from a mix of OM from the landscape and *in situ* primary production (Tamalavage et al., 2018). However, these paleo values are actually closer to degraded $\delta^{13}C_{POM}$ values from the MZ or SGW of the water column (**Fig. 4:7B**), and reflect OM that has been transformed in the MZ. Sedimentary $\delta^{13}C_{org}$ values from ~1500 to 1000 cal yr BP are more similar to depleted $\delta^{13}C_{POM}$ values within the ML (**Fig. 4:7B**), which is consistent with an earlier assessment for increased contributions of OM from primary productivity during this interval (Tamalavage et al., 2018). Throughout the 3000-year sedimentary record from Blackwood Sinkhole the C:N ratios of OM are much higher (> 18) (Tamalavage et al., 2018), and $\delta^{15}N$ values are more enriched in comparison to POM values within the SGW. Offsets between water column POM and sedimentary OM values likely reflect the additional contributions of the sinking, terrestrially-derived particles not included in the suspended fraction that we

have collected for the present study (Middelburg and Nieuwenhuize, 1998), or perhaps diagenesis of OM after burial (Benner et al., 1991; Gonneea et al., 2004). For example, each 1-cm sediment sample analyzed for $\delta^{13}C_{org}$ values and C:N ratio represents a time averaged sample (~10 years of inputs), versus the snapshot of the water column measurements documented here. Given that the wetland was established during the last 1000 years (Tamalavage et al., 2020; Fall et al., 2021), large fluxes of $\delta^{13}C$-enriched OM occurring on multi-centennial timescales from the terrestrial surface may have a greater quantitative influence on the archived sediment record, versus the long-term background flux from *in situ* production, which could have a more negative value.

GDGT analysis provides molecular evidence that OM produced within the ML can be eventually preserved within the sediments. To explore the incorporation of a single class of compounds within the suspended POM to the sediments, we focus on comparing sedimentary GDGT ratios from ~3000 to 1000 cal yr BP to water column POM values, as the last ~1000 years were affected by increased inputs from the proximal wetland, as detected by bulk $\delta^{13}C_{org}$ (Tamalavage et al., 2018) and here confirmed by the increased BIT ratio (> 0.7, **Fig. 4:8**) and lower ΣisoGDGTs. Reconstructed temperatures from sedimentary TEX_{86} values from ~3000 to 1000 cal yr BP are 29 ± 1°C, falling within 2°C of ML temperatures recorded during previous summertime hydrographic surveys (mean: 27.3 ± 2.0°C). Along with $\delta^{13}C_{org}$ values deposited during this time, calculated GDGT ratios from ~1500 to 1000 cal yr BP in Blackwood sediments most closely resemble GDGT values within the ML providing compound specific evidence for POM produced *in situ* accumulating within the archived

sediment. Reconstructed temperatures closely resemble summertime sinkhole surface temperatures, so perhaps there is increased *in situ* POM being exported to the sediments during the summertime.

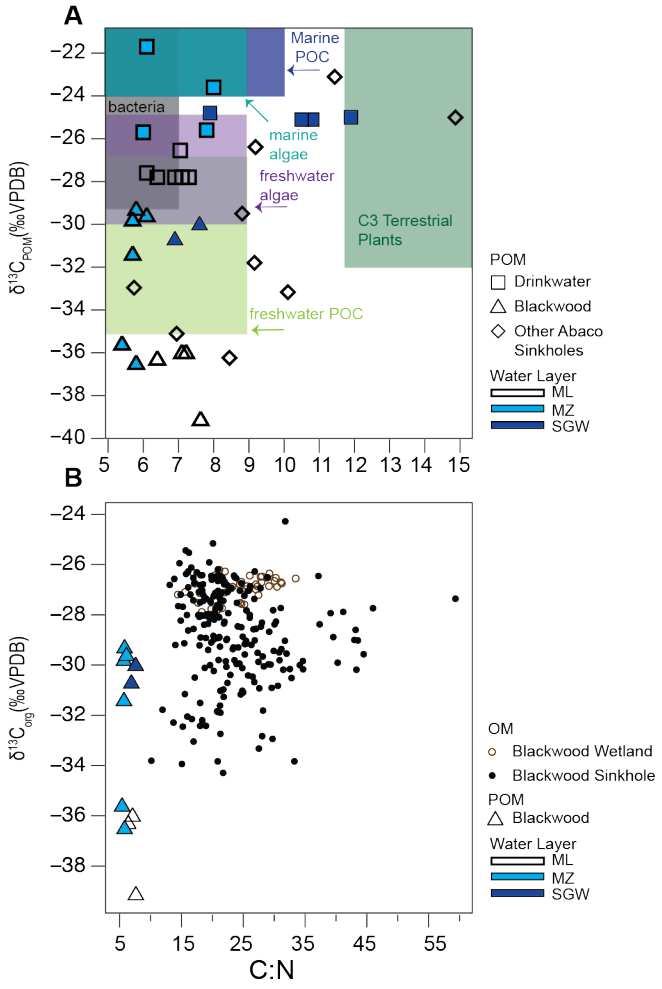

Figure 4:7: Comparison between water column (POM) and sediments (OM).
A) Cross plot of $\delta^{13}C$ and C:N with water column POM samples in shades of blue with compiled typical literature values adapted from (Lamb et al., 2006), B) measurements for Blackwood OM are from sinkhole sediments (black) and wetland sediments (brown outline) analyzed within (Tamalavage et al., 2018), plus water column POM values (triangles).

To increase POM export from the ML to the sediment water interface, variability in biogeochemical processes would have been changing the Blackwood water column. From ~1500 to 1000 cal yr BP, proxy evidence for reconstructed δ^2H_{precip} from leaf waxes (alkanoic acids) suggests a drier Abaco (**Fig. 4:8A**), potentially impacting physical stratification/mixing within the water column. These hydrologic changes could perhaps promote increased production in the ML, and a change in the nitrogen source used during assimilation (e.g., $NH4^+$), leading to enriched bulk $\delta^{15}N_{org}$ in the sediments (Hadas et al., 2009). As seasonally variability of N cycling has been observed within other lake systems impacting stable isotopic composition of POM and OM (Lehmann et al., 2004; Hadas et al., 2009), it is possible that there is seasonal N cycling within Blackwood (along with inputs from the adjacent landscape), which could explain similar GDGT, $\delta^{15}N_{org}$, and $\delta^{13}C_{org}$ signatures depositing from ~3000 to 2000 cal yr BP. Additional GDGT measurements from ~2000 to 1700 cal yr BP would help to draw comparisons to an time period interpreted as wetter on Abaco, perhaps influencing biogeochemical cycling within a differently structured water column (resulting in a more negative $\delta^{15}N_{org}$, and more enriched $\delta^{13}C_{org}$ within the sediments). Alternatively, the higher concentrations within the sediments (**Table 4:2**) in comparison to the water column (**Table 4:1**) may be evidence for selective preservation of these compounds within sinkhole systems, making them a viable target for future work. Additional water column measurements (e.g., seasonal sampling of suspended/sinking particles, dissolved components, compound specific analysis) coupled to similar analysis in sedimentary OM could identify new ways to interpret geochemical proxies archived within a globally

distributed coastal sinkholes, informing robust reconstruction of paleoenvironmental and biogeochemical dynamics.

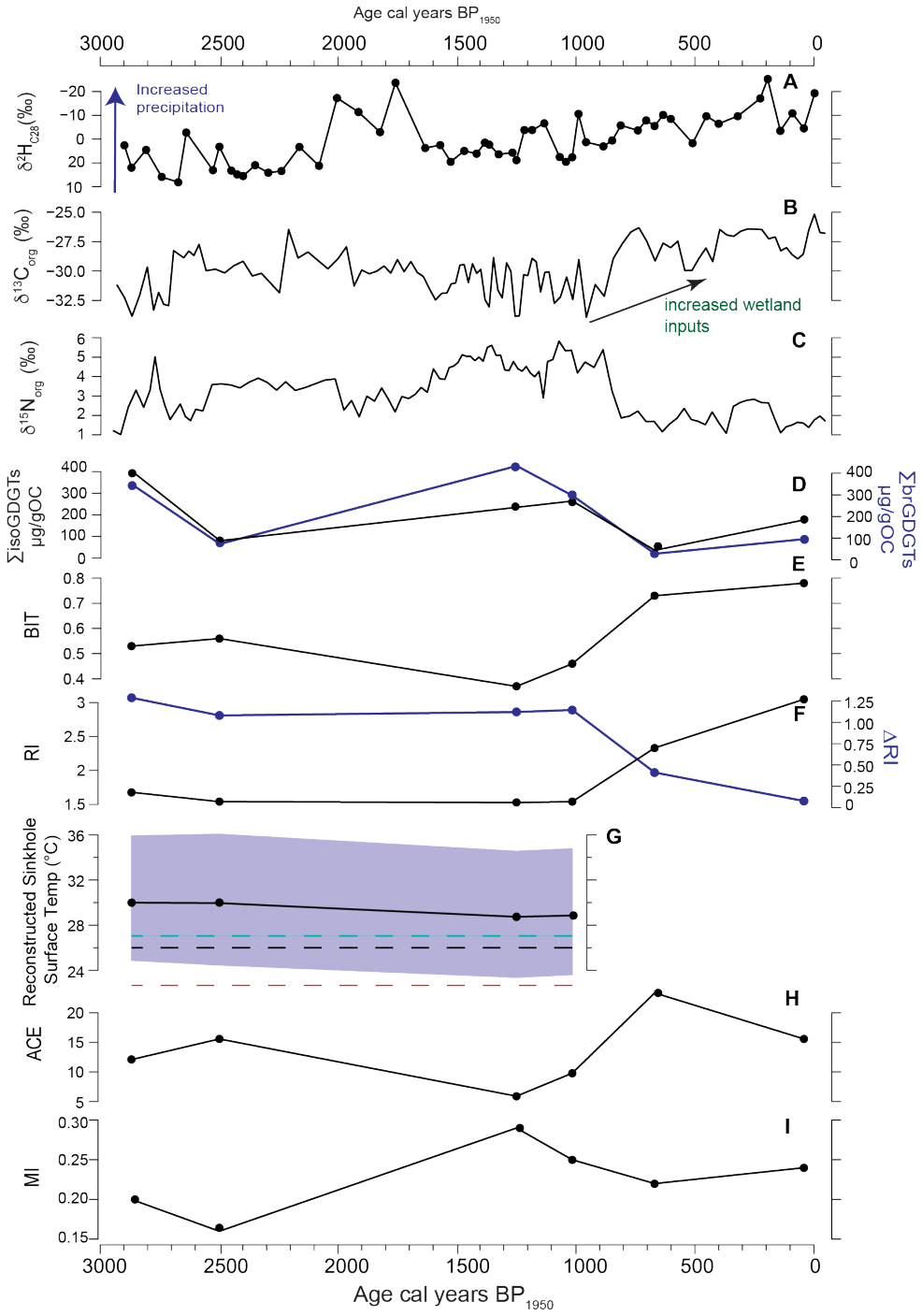

Figure 4:8: Comparison of previously published data from the Blackwood Sinkhole with water column data.

BLWD-C2 core (A-C) δ^2H_{precip} reconstructions from plant wax (Tamalavage et al., 2020), bulk $\delta^{13}C_{org}$ and $\delta^{15}N_{org}$ of (Tamalavage et al., 2018) with (D-I) the GDGT results from this study (abbreviations as in Figure 6). Within (G), the black dots are the

reconstructed sinkhole surface temperature output from BAYSPAR, with 90% uncertainty (shaded). The black dashed line is modeled sea surface temperature for the latitude/longitude of Blackwood sinkhole, and the with mean (measured) sinkhole surface temperatures in the summer (dashed blue) and winter (dashed red) as lines.

4.6. Conclusions

- Hydrographic profiles reveal density stratification along depth transects within two coastal sinkholes on Great Abaco Island, The Bahamas that can be characterized into three layers i) a meteoric lens (ML), ii) a mixing zone (MZ), and iii) anoxic saline groundwater (SGW). Variability in physicochemical gradients and $\delta^{2}H_{water}$ and $\delta^{18}O_{water}$ composition of the ML suggests site specific influences to hydrology at each site (e.g., evaporation in the larger, more aerially exposed basin).
- $\delta^{13}C_{POM}$, $\delta^{15}N_{POM}$, and C:N from SPM collected during boreal winter across these physicochemical gradients suggest *in situ* productivity in the ML and POM degradation in the MZ and SGW layers.
- Compound specific GDGTs provide biomarker evidence for mixed terrestrial and aquatic (produced *in situ*) POM throughout the water column, with higher aquatic inputs in the upper ML. Two ML samples were viable for TEX_{86} reconstructions of sinkhole surface temperature falling within ~7°C of hydrographically surveyed winter time temperatures. Below the ML, GDGTs indices are influenced by methanotrophic *Euryarchaeota* and brGDGTs (from terrestrial or bacterial sources).

- $\delta^{13}C_{POM}$, $\delta^{15}N_{POM}$, C:N, colors of filtered SPM and GDGTs suggest that nitrogen fixation, denitrification, sulfide oxidation, sulfate reduction, and AOM (by archaea) are occurring throughout the water column and impacting the POM pool, potentially impacting the POM export via SGD to the coastal ocean.
- Comparison of $\delta^{13}C_{POM}$, $\delta^{15}N_{POM}$, C:N, and GDGTs from SPM to sedimentary OM archived within Blackwood sinkhole provides evidence that POM produced *in situ* within the upper ML is indeed being incorporated into the sedimentary OM matrix. Reconstructed sinkhole surface temperatures that are within 2°C of previously surveyed summertime temperatures would suggest that export from the ML to the sediment water interface occurs during boreal summer.

4.7. References

Altabet, M., 1988. Variations in nitrogen isotopic composition between sinking and suspended particles: Implications for nitrogen cycling and particle transformation in the open ocean. Deep Sea Research Part A. Oceanographic Research Papers 35, 535-554.

Arndt, S., Jørgensen, B.B., LaRowe, D.E., Middelburg, J., Pancost, R., Regnier, P., 2013. Quantifying the degradation of organic matter in marine sediments: A review and synthesis. Earth-science reviews 123, 53-86.

Beck, A.J., Charette, M.A., Cochran, J.K., Gonneea, M.E., Peucker-Ehrenbrink, B., 2013. Dissolved strontium in the subterranean estuary–implications for the marine strontium isotope budget. Geochimica et Cosmochimica Acta 117, 33-52.

Beddows, P.A., Smart, P.L., Whitaker, F.F., Smith, S.L., 2007. Decoupled fresh–saline groundwater circulation of a coastal carbonate aquifer: spatial patterns of temperature and specific electrical conductivity. Journal of Hydrology 346, 18-32.

Benner, R., Fogel, M.L., Sprague, E.K., 1991. Diagenesis of belowground biomass of Spartina alterniflora in salt-marsh sediments. Limnology and Oceanography 36, 1358-1374.

Björnerås, C., Škerlep, M., Gollnisch, R., Herzog, S.D., Ugge, G.E., Hegg, A., Hu, N., Johansson, E., Lee, M., Pärssinen, V., 2020. Inland blue holes of The Bahamas–chemistry and biology in a unique aquatic environment. Fundamental and Applied Limnology 194, 95-106.

Bowen, G.J., Putman, A., Brooks, J.R., Bowling, D.R., Oerter, E.J., Good, S.P., 2018. Inferring the source of evaporated waters using stable H and O isotopes. Oecologia 187, 1025-1039.

Burns, S.J., Neumann, A.C., 1987. Pelagic sedimentation on an inactive gullied slope, Northwest Providence Channel, Bahamas. Marine geology 77, 277-286.

Carew, J.L., Mylroie, J.E., 1997. Geology of the Bahamas, in: Vacher, L., Quinn, T. (Eds.), Geology and Hydrogeology of Carbonate Islands, Developments in Sedimentology. Elsevier Science Publishers, Amsterdam, pp. 91-139.

Cifuentes, L., Sharp, J., Fogel, M.L., 1988. Stable carbon and nitrogen isotope biogeochemistry in the Delaware estuary. Limnology and oceanography 33, 1102-1115.

Craig, H., 1961. Isotopic Variations in Meteoric Waters. Science 133, 1702-1703.

Damsté, J.S.S., Hopmans, E.C., Pancost, R.D., Schouten, S., Geenevasen, J.A., 2000. Newly discovered non-isoprenoid glycerol dialkyl glycerol tetraether lipids in sediments. Chemical Communications, 1683-1684.

Damsté, J.S.S., Rijpstra, W.I.C., Foesel, B.U., Huber, K.J., Overmann, J., Nakagawa, S., Kim, J.J., Dunfield, P.F., Dedysh, S.N., Villanueva, L., 2018. An overview of the occurrence of ether-and ester-linked iso-diabolic acid membrane lipids in microbial cultures of the Acidobacteria: Implications for brGDGT paleoproxies for temperature and pH. Organic Geochemistry 124, 63-76.

Damsté, J.S.S., Schouten, S., Hopmans, E.C., Van Duin, A.C., Geenevasen, J.A., 2002. Crenarchaeol. Journal of lipid research 43, 1641-1651.

Degens, E., 1969. Biogeochemistry of stable carbon isotopes. Organic geochemistry, 304-329.

Fall, P.L., van Hengstum, P.J., Lavold-Foote, L., Donnelly, J.P., Albury, N.A., Tamalavage, A.E., 2021. Human arrival and landscape dynamics in the northern Bahamas. Proceedings of the National Academy of Sciences 118.

Feakins, S.J., Wu, M.S., Ponton, C., Tierney, J.E., 2019. Biomarkers reveal abrupt switches in hydroclimate during the last glacial in southern California. Earth and Planetary Science Letters 515, 164-172.

Filley, T.R., Freeman, K.H., Bianchi, T.S., Baskaran, M., Colarusso, L.A., Hatcher, P.G., 2001. An isotopic biogeochemical assessment of shifts in organic matter input to Holocene sediments from Mud Lake, Florida. Organic Geochemistry 32, 1153-1167.

Fogel, M.L., Cifuentes, L.A., 1993. Isotope Fractionation during Primary Production, in: Engel, M.H., Macko, S.A. (Eds.), Organic Geochemistry, Principles and Applications. Springer Science+Business, New York, USA, pp. 73-94.

Fogel, M.L., Cifuentes, L.A., Velinsky, D.J., Sharp, J.H., 1992. Relationship of carbon availability in estuarine phytoplankton to isotopic composition. Marine Ecology Progress Series, 291-300.

France, R., 1995. Carbon-13 enrichment in benthic compared to planktonic algae: foodweb implications. Marine ecology progress series 124, 307-312.

Fry, B., Jannasch, H.W., Molyneaux, S.J., Wirsen, C.O., Muramoto, J.A., King, S., 1991. Stable isotope studies of the carbon, nitrogen and sulfur cycles in the Black Sea and the Cariaco Trench. Deep Sea Research Part A. Oceanographic Research Papers 38, S1003-S1019.

Gibson, J., Birks, S., Yi, Y., 2016. Stable isotope mass balance of lakes: a contemporary perspective. Quaternary Science Reviews 131, 316-328.

Gonneea, M.E., Paytan, A., Herrera-Silveira, J.A., 2004. Tracing organic matter sources and carbon burial in mangrove sediments over the past 160 years. Estuarine, Coastal and Shelf Science 61, 211-227.

Gonzalez, B.C., Iliffe, T.M., Macalady, J.L., Schaperdoth, I., Kakuk, B., 2011. Microbial hotspots in anchialine blue holes: initial discoveries from the Bahamas. Hydrobiologia 677, 149-156.

Gregory, 2016. The Influence of Morphology on Sinkhole Sedimentation at Little Salt Spring, Florida. Journal of Coastal Research.

Gu, B., 2009. Variations and controls of nitrogen stable isotopes in particulate organic matter of lakes. Oecologia 160, 421-431.

Gu, B., Chapman, A.D., Schelske, C.L., 2006. Factors controlling seasonal variations in stable isotope composition of particulate organic matter in a softwater eutrophic lake. Limnology and Oceanography 51, 2837-2848.

Gu, B., Schelske, C.L., Waters, M.N., 2011. Patterns and controls of seasonal variability of carbon stable isotopes of particulate organic matter in lakes. Oecologia 165, 1083-1094.

Haas, S., De Beer, D., Klatt, J.M., Fink, A., Rench, R.M., Hamilton, T.L., Meyer, V., Kakuk, B., Macalady, J.L., 2018. Low-light anoxygenic photosynthesis and Fe-S-biogeochemistry in a microbial mat. Frontiers in Microbiology 9, 858.

Hadas, O., Altabet, M.A., Agnihotri, R., 2009. Seasonally varying nitrogen isotope biogeochemistry of particulate organic matter in Lake Kinneret, Israel. Limnology and Oceanography 54, 75-85.

Hatcher, P.G., Simoneit, B.R., Mackenzie, F.T., Neumann, A.C., Thorstenson, D.C., Gerchakov, S.M., 1982. Organic geochemistry and pore water chemistry of sediments from Mangrove Lake, Bermuda. Organic Geochemistry 4, 93-112.

He, Y., Wang, H., Meng, B., Liu, H., Zhou, A., Song, M., Kolpakova, M., Krivonogov, S., Liu, W., Liu, Z., 2020. Appraisal of alkenone-and archaeal ether-based salinity indicators in mid-latitude Asian lakes. Earth and Planetary Science Letters 538, 116236.

Hedges, J.I., Keil, R.G., Benner, R., 1997. What happens to terrestrial organic matter in the ocean? Organic Geochemistry 27, 195-212.

Hodell, D.A., Brenner, M., Curtis, J.H., Medina-Gonzalez, R., Can, E.I.-C., Albornaz-Pat, A., Guilderson, T.P., 2005. Climate change on the Yucatan Peninsula during the little ice age. Quaternary Research 63, 109-121.

Hollander, D.J., McKenzie, J.A., 1991. CO2 control on carbon-isotope fractionation during aqueous photosynthesis: A paleo-pCO2 barometer. Geology 19, 929-932.

Hopmans, E.C., Weijers, J.W., Schefuß, E., Herfort, L., Damsté, J.S.S., Schouten, S., 2004. A novel proxy for terrestrial organic matter in sediments based on branched and isoprenoid tetraether lipids. Earth and Planetary Science Letters 224, 107-116.

Hua, M., Zhang, X., Yao, T., Luo, Z., Zhou, H., Rao, Z., He, X., 2019. Dual effects of precipitation and evaporation on lake water stable isotope composition in the monsoon region. Hydrological Processes 33, 2192-2205.

Huang, Y., Shuman, B., Wang, Y., Webb III, T., Grimm, E.C., Jacobson Jr, G.L., 2006. Climatic and environmental controls on the variation of C3 and C4 plant abundances in central Florida for the past 62,000 years. Palaeogeography, Palaeoclimatology, Palaeoecology 237, 428-435.

Humphreys, W., 1999. Physico-chemical profile and energy fixation in Bundera Sinkhole, an anchialine remiped habitat in north-western Australia. Journal of the Royal Society of Western Australia 82, 89.

IAEA/WMO, 2019. Global Network of Isotopes in Precipitation. The GNIP Database.

Kaiser, K., Benner, R., 2008. Major bacterial contribution to the ocean reservoir of detrital organic carbon and nitrogen. Limnology and Oceanography 53, 99-112.

Kennedy, P., Kennedy, H., Papadimitriou, S., 2005. The effect of acidification on the determination of organic carbon, total nitrogen and their stable isotopic composition in algae and marine sediment. Rapid Communications in Mass Spectrometry: An International Journal Devoted to the Rapid Dissemination of Up-to-the-Minute Research in Mass Spectrometry 19, 1063-1068.

Kharbush, J., Close, H., van Mooy, B., Arnosti, C., Smittenberg, R., Le Moigne, F., Mollenhauer, G., Scholz-Böttcher, B., Obreht, I., Koch, B., 2020. Particulate organic

carbon deconstructed: Molecular and chemical composition of particulate organic carbon in the ocean. Frontiers in Marine Science 7.

Lamb, A.L., Wilson, G.P., Leng, M.J., 2006. A review of coastal palaeoclimate and relative sea-level reconstructions using δ13C and C/N ratios in organic material. Earth-Science Reviews 75, 29-57.

Lehmann, M.F., Bernasconi, S.M., McKenzie, J.A., Barbieri, A., Simona, M., Veronesi, M., 2004. Seasonal variation of the δC and δN of particulate and dissolved carbon and nitrogen in Lake Lugano: Constraints on biogeochemical cycling in a eutrophic lake. Limnology and Oceanography 49, 415-429.

Liu, X.-L., Zhu, C., Wakeham, S.G., Hinrichs, K.-U., 2014. In situ production of branched glycerol dialkyl glycerol tetraethers in anoxic marine water columns. Marine Chemistry 166, 1-8.

Lohse, L., Kloosterhuis, R.T., de Stigter, H.C., Helder, W., van Raaphorst, W., van Weering, T.C., 2000. Carbonate removal by acidification causes loss of nitrogenous compounds in continental margin sediments. Marine Chemistry 69, 193-201.

Lone, A., Fousiya, A., Shah, R., Achyuthan, H., 2018. Reconstruction of paleoclimate and environmental fluctuations since the early Holocene period using organic matter and C: N proxy records: A review. Journal of the Geological Society of India 91, 209-214.

Meyers, P.A., 1994. Preservation of elemental and isotopic source identification of sedimentary organic matter. Chemical Geology 114, 289-302.

Middelburg, J.J., Nieuwenhuize, J., 1998. Carbon and nitrogen stable isotopes in suspended matter and sediments from the Schelde Estuary. Marine Chemistry 60, 217-225.

Mullins, H.T., Heath, K.C., Van Buren, H.M., Newton, C.R., 1984. Anatomy of a modern open-ocean carbonate slope: northern Little Bahama Bank. Sedimentology 31, 141-168.

Mullins, H.T., Lynts, G.W., 1977. Origin of the northwestern Bahama Platform: Review and reinterpretation. Geological Society of America Bulletin 88, 1447-1461.

Mullins, H.T., Neumann, A.C., 1979. Deep carbonate bank margin structure and sedimentation in the northern Bahamas.

Mylroie, J.E., Carew, J.L., Vacher, H., 1995. Karst development in the Bahamas and Bermuda. Geological Society of America Special Papers 300, 251-267.

O'Leary, M.H., 1988. Carbon isotopes in photosynthesis. BioScience 38, 328-336.

Owens, N., 1988. Natural variations in 15N in the marine environment. Advances in marine biology 24, 389-451.

Peaple, M.D., Tierney, J.E., McGee, D., Lowenstein, T.K., Bhattacharya, T., Feakins, S.J., 2021. Identifying plant wax inputs in lake sediments using machine learning. Organic Geochemistry, 104222.

Peros, M., Collins, S., G'Meiner, A.A., Reinhardt, E., Pupo, F.M., 2017. Multistage 8.2 kyr event revealed through high-resolution XRF core scanning of Cuban sinkhole sediments. Geophysical Research Letters 44, 7374-7381.

Pester, M., Schleper, C., Wagner, M., 2011. The Thaumarchaeota: an emerging view of their phylogeny and ecophysiology. Current opinion in microbiology 14, 300-306.

Peters, K.E., Sweeney, R.E., Kaplan, I.R., 1978. Correlation of carbon and nitrogen stable isotope ratios in sedimentary organic matter. Association for the Sciences of LImnology and Oceanography 23, 598-604.

Powers, L.A., Werne, J.P., Johnson, T.C., Hopmans, E.C., Damsté, J.S.S., Schouten, S., 2004. Crenarchaeotal membrane lipids in lake sediments: a new paleotemperature proxy for continental paleoclimate reconstruction? Geology 32, 613-616.

Reeder, S.L., Rankey, E.C., 2009. Controls on morphology and sedimentology of carbonate tidal deltas, Abacos, Bahamas. Marine Geology 267, 141-155.

Ritter, S.M., Isenbeck-Schröter, M., Scholz, C., Keppler, F., Gescher, J., Klose, L., Schorndorf, N., Avilés Olguín, J., González-González, A., Stinnesbeck, W., 2019. Subaqueous speleothems (Hells Bells) formed by the interplay of pelagic redoxcline

biogeochemistry and specific hydraulic conditions in the El Zapote sinkhole, Yucatán Peninsula, Mexico. Biogeosciences 16, 2285-2305.

Saino, T., Hattori, A., 1987. Geographical variation of the water column distrubution of suspended particulate organic nitrogen and its 15N natural abundance in the Pacific and its marginal seas. Deep Sea Research Part A. Oceanographic Research Papers 34, 807-827.

Sánchez, M., Alcocer, J., Escobar, E., Lugo, A., 2002. Phytoplankton of cenotes and anchialine caves along a distance gradient from the northeastern coast of Quintana Roo, Yucatan Peninsula. Hydrobiologia 467, 79-89.

Schouten, S., Hopmans, E.C., Pancost, R.D., Damsté, J.S.S., 2000. Widespread occurrence of structurally diverse tetraether membrane lipids: evidence for the ubiquitous presence of low-temperature relatives of hyperthermophiles. Proceedings of the National Academy of Sciences 97, 14421-14426.

Schouten, S., Hopmans, E.C., Schefuß, E., Damste, J.S.S., 2002. Distributional variations in marine crenarchaeotal membrane lipids: a new tool for reconstructing ancient sea water temperatures? Earth and Planetary Science Letters 204, 265-274.

Seymour, J., Humphreys, W., Mitchell, J., 2007. Stratification of the microbial community inhabiting an anchialine sinkhole. Aquatic Microbial Ecology 50, 11-24.

Sheridan, R., Mullins, H., Austin Jr, J., Ball, M., Ladd, J., 1988. Geology and geophysics of the Bahamas. The Geology of North America 1, 2.

Shinn, E.A., Reich, C.D., Locker, S.D., Hine, A.C., 1996. A giant sediment trap in the Florida Keys. Journal of Coastal Research, 953-959.

Socki, R.A., Perry, E.J.C., Romanek, C.S., 2002. Stable isotope systematics of two cenotes from the northern Yucatan Peninsula, Mexico. Limnology and Oceanography 47, 1808-1818.

Tamalavage, A.E., van Hengstum, P.J., Louchouarn, P., Fall, P.L., Donnelly, J.P., Albury, N.A., Coats, S., Feakins, S.J., 2020. Plant wax evidence for precipitation and

vegetation change from a coastal sinkhole lake in the Bahamas spanning the last 3000 years. Organic Geochemistry 150, 104120.

Tamalavage, A.E., van Hengstum, P.J., Louchouarn, P., Molodtsov, S., Kaiser, K., Donnelly, J.P., Albury, N.A., Fall, P.L., 2018. Organic matter sources and lateral sedimentation in a Bahamian karst basin (sinkhole) over the late Holocene: Influence of local vegetation and climate. Palaeogeography, Palaeoclimatology, Palaeoecology 506, 70-83.

Tierney, J.E., Russell, J.M., 2009. Distributions of branched GDGTs in a tropical lake system: implications for lacustrine application of the MBT/CBT paleoproxy. Organic Geochemistry 40, 1032-1036.

Tierney, J.E., Tingley, M.P., 2015. A TEX 86 surface sediment database and extended Bayesian calibration. Scientific data 2, 1-10.

Turich, C., Freeman, K.H., 2011. Archaeal lipids record paleosalinity in hypersaline systems. Organic Geochemistry 42, 1147-1157.

Van Hardenbroek, M., Chakraborty, A., Davies, K., Harding, P., Heiri, O., Henderson, A., Holmes, J., Lasher, G., Leng, M., Panizzo, V., 2018. The stable isotope composition of organic and inorganic fossils in lake sediment records: Current understanding, challenges, and future directions. Quaternary Science Reviews 196, 154-176.

van Hengstum, P.J., Albury, N.A., Beddows, P.A., D'Entremont, N.E., Feakins, S.J., Donnelly, J.P., Little, S.N., McKeon, K., Ma, X., Mendez, J., Year. Proceedings of AGU Fall Meeting Abstracts 2019, pp. GC51I-0942.

van Hengstum, P.J., Donnelly, J.P., Fall, P.L., Toomey, M.R., Albury, N.A., Kakuk, B., 2016. The intertropical convergence zone modulates intense hurricane strikes on the western North Atlantic margin. Scientific Reports 6, 1-10.

van Hengstum, P.J., Maale, G., Donnelly, J.P., Albury, N.A., Onac, B.P., Sullivan, R.M., Winkler, T.S., Tamalavage, A.E., MacDonald, D., 2018. Drought in the northern Bahamas from 3300 to 2500 years ago. Quaternary Science Reviews 186, 169-185.

van Hengstum, P.J., Scott, D.B., Gröcke, D.R., Charette, M.A., 2011. Sea level controls sedimentation and environments in coastal caves and sinkholes. Marine Geology 286, 35-50.

van Hengstum, P.J., Winkler, T.S., Tamalavage, A.E., Sullivan, R.M., Little, S.N., MacDonald, D., Donnelly, J.P., Albury, N.A., 2020. Holocene sedimentation in a blue hole surrounded by carbonate tidal flats in The Bahamas: Autogenic versus allogenic processes. Marine Geology 419, 106051.

Walker, L.N., 2006. The caves, karst, and geology of Abaco Island, Bahamas. Mississippi State University.

Walker, L.N., Mylorie, J.E., Walker, A.D., Mylroie, J.R., 2008. The caves of Abaco Island, Bahamas: keys to geologic timescales. Journal of Cave and Karst Studies 70, 108-119.

Walker, S., Azetsu-Scott, K., Normandeau, C., Kelley, D., Friedrich, R., Newton, R., Schlosser, P., McKay, J., Abdi, W., Kerrigan, E., 2016. Oxygen isotope measurements of seawater (18O/16O): A comparison of cavity ring-down spectroscopy (CRDS) and isotope ratio mass spectrometry (IRMS). Limnology and Oceanography: Methods 14, 31-38.

Wang, H., Liu, W., Zhang, C.L., Jiang, H., Dong, H., Lu, H., Wang, J., 2013. Assessing the ratio of archaeol to caldarchaeol as a salinity proxy in highland lakes on the northeastern Qinghai–Tibetan Plateau. Organic geochemistry 54, 69-77.

Weijers, J.W., Schouten, S., Spaargaren, O.C., Damsté, J.S.S., 2006. Occurrence and distribution of tetraether membrane lipids in soils: Implications for the use of the TEX86 proxy and the BIT index. Organic Geochemistry 37, 1680-1693.

Whitaker, F.F., Smart, P.L., 1997. Groundwater circulation and geochemistry of a karstified bank–marginal fracture system, South Andros Island, Bahamas. Journal of Hydrology 197, 293-315.

Wong, W.W., Sackett, W.M., 1978. Fractionation of stable carbon isotopes by marine phytoplankton. Geochimica et Cosmochimica Acta 42, 1809-1815.

Yao, P., Wang, X., Bianchi, T., Yang, Z., Fu, L., Zhang, X., Chen, L., Zhao, B., Morrison, E., Shields, M., 2020. Carbon cycling in the world's deepest blue hole. Journal of Geophysical Research: Biogeosciences 125, e2019JG005307.

Zhang, Y.G., Pagani, M., Wang, Z., 2016. Ring Index: A new strategy to evaluate the integrity of TEX86 paleothermometry. Paleoceanography 31, 220-232.

Zhang, Y.G., Zhang, C.L., Liu, X.-L., Li, L., Hinrichs, K.-U., Noakes, J.E., 2011. Methane Index: A tetraether archaeal lipid biomarker indicator for detecting the instability of marine gas hydrates. Earth and Planetary Science Letters 307, 525-534.

5. CONCLUSIONS

This dissertation posed the following three overarching questions:

- Can δ^2H signatures of leaf wax biomarkers (*n*-alkanoic acids) be reliably used to reconstruct late Holocene rainfall patterns on a near shoreline sinkhole lake, or a mid-Holocene inland sinkhole lake from the tropics?
    - What technical, geomorphologic, or ecologic limitations are there to the approach (e.g., changes in sedimentation rate and source, local terrestrial vegetation shifts and the presence of salt tolerant mangrove communities)?
- How do current water column conditions impact the suspended particulate organic matter (POM), and bulk/biomarker organic matter (OM) preservation in coastal sinkholes?

Leaf wax records were successfully extracted and analyzed to reconstruct past changes in δ^2H from the mid-Holocene until present (Chapter II and III). Within Chapter II, it was found that when pollen indicates a stable terrestrial plant community (~3000 to 850 cal yrs BP), variations of δ^2H values measured on the plant wax C_{28} *n*-alkanoic acid are interpreted in terms of precipitation isotope (δ^2H_{precip}) changes. But, when δ^2H values decrease (−50‰) concurrent with increased *Laguncularia racemosa* (white mangrove) and *Conocarpus erectus* (buttonwood mangrove), and the mangrove-derived biomarker, taraxerol at ~850 cal yr BP, ^2H-depletion tracks vegetation changes on the landscape, versus a δ^2H shift. However, a pollen-based correction for mangrove inputs was developed, yielding reconstructed precipitation isotope estimates ($\delta^2H_{precip\text{-}corr}$) of

$\delta^2H_{precip\text{-}corr}$ from –33 to +25‰ throughout the last 2950 years, with uncertainties on the order of 10-20‰. In Chapter III, long-chained terrestrial leaf waxes (e.g., C_{28}) deposited in a homogenous unit of lacustrine marl from ~8300 to 1700 cal yr BP are in lesser abundance after ~4800 cal yr BP, suggesting increased algal contributions to accumulating sedimentary OM. Concentrations of leaf waxes deposited after ~4700 cal yr BP are below 1 µg/g, making it difficult to recover a δ^2H signal on terrestrially based C_{28} that falls within an ideal voltage to check against H_2 linearity. However, we interpret variability in δ^2H_{C28} from ~3000 to 850 within Blackwood, and ~8000 to 4800 within Emerald pond, plus pollen corrected δ^2H_{C28} values within Blackwood over the last ~850 as regional shifts in hydroclimate.

Holocene hydroclimate shifts are recorded within both Blackwood (Chapter III) and Emerald Pond (Chapter IV). More enriched δ^2H values archived within Blackwood from 3050 to 2100 cal yrs BP correspond to evidence for aridity across the Caribbean between ~3300 and 2500 cal yrs BP (Berman and Pearsall, 2000; Fensterer et al., 2013; Gregory et al., 2015), and generally high $\delta^2H_{precip\text{-}corr}$ at ~1230 cal yr BP could align with the onset of the "Terminal Classic Drought" that impacted communities in Mexico (Curtis et al., 1998; Hodell et al., 2005; Douglas et al., 2015), Costa Rica (Taylor et al., 2020), and Hispaniola (Lane et al., 2014). More depleted δ^2H values recorded in Emerald Pond from ~6000 to 4800 cal yr BP would suggest wetter conditions that is consistent with previous regional work in nearby Haiti and Cuba (Hodell et al., 1991). In the northern IAS, NASH variability is the dominant regulator of regional rainfall (Li et al., 2012). iCESM simulations (Chapter II) suggest that regional-to-large scale climate

dynamics drive local variability in δ^2H at Abaco (Tamalavage et al., 2020). In the composite of ^2H-depleted years, the NASH is weak (i.e. lower central pressure) and contracted (i.e. western boundary displaced further to the East), and there are wetter conditions across the Caribbean. In contrast, more enriched δ^2H values are associated with an intense and expanded NASH, which could suppress convection (supporting dry conditions). Variability in reconstructed δ^2H_{precip} suggests shifts in NASH strength over the Holocene.

In chapter IV, $\delta^{13}C_{POM}$, $\delta^{15}N_{POM}$, and C:N collected from SPM during boreal winter across physicochemical gradients within Blackwood and Drinkwater Sinkhole suggest *in situ* productivity in the meteoric lens and POM degradation in the MZ and SGW layers. Variability in physicochemical gradients and δ^2H_{water} and $\delta^{18}O_{water}$ composition of the meteoric lens suggests site specific influences to hydrology at each site (e.g., evaporation in the larger, more aerially exposed basin). Compound specific GDGTs provide biomarker evidence for mixed terrestrial and aquatic (produced *in situ*) POM throughout the water column, with higher aquatic inputs in the upper meteoric lens and methanotrophic *Euryarchaeota* influence in the mixing zone and saline groundwater. Meteoric lens samples are viable for TEX_{86} reconstructions of sinkhole surface temperature that fall within ~7°C of hydrographically surveyed boreal wintertime temperatures. Comparison of $\delta^{13}C_{POM}$, $\delta^{15}N_{POM}$, C:N, and GDGTs from POM to sedimentary OM archived within Blackwood sinkhole provides evidence that POM produced *in situ* within the upper ML is indeed being incorporated into the sedimentary OM matrix. Reconstructed sedimentary sinkhole surface temperatures from TEX_{86} fall

within 2°C of previously surveyed summertime temperatures, suggesting that there is increased export from the ML to the sediment water interface that occurs during the summertime.

The findings of this dissertation suggest that terrestrially derived organic matter inputs preserved within sinkhole records can reconstruct paleohydrology on Holocene timescales. However, caution is advised if the site is surrounded by a mangrove, or if the sinkhole has consistently and homogenously accumulated lacustrine marl for a prolonged period of time (suggesting shallow lake-like conditions with abundant submerged vegetation likely impacting the terrestrial signal). Bulk isotopic and GDGT signatures of microbial-derived lipids were discovered (stable isotopes and biomarkers) throughout the water the water column of two stratified sinkhole basins. These geochemical findings suggest production within the upper meteoric lens, and degradation of POM, mediated by the microbial community, in the lower mixing zone and saline groundwater. It is likely that site-specific hydrology impacts water column POM production, degradation, and eventual OM signatures preserved, yet those impacts are not fully resolved. But, additional seasonal monitoring, including analysis of dissolved ions and measurement of sinking POM (e.g., sediment traps) can address the drivers and impacts of biogeochemical processes within sinkhole basins. Comparison of water column bulk stable isotopic compositions and molecular-specific GDGTs to sedimentary OM signatures suggest export of *in situ* POM to the sediment, making algal-derived signatures a viable target for future paleoenvironmental reconstructions from coastal sinkholes and blue holes.

5.1. References

Berman, M.J., Pearsall, D.M., 2000. Plants, people, and culture in the prehistoric central Bahamas: A view from the Three Dog Site, an early Lucayan settlement on San Salvador Island, Bahamas. Latin American Antiquity 11, 219-239.

Curtis, J.H., Brenner, M., Hodell, D.A., Balser, R.A., Islebe, G.A., Hooghiemstra, H., 1998. A multi-proxy study of Holocene environmental change in the Maya Lowlands of Peten, Guatemala. Journal of Paleolimnology 19, 139-159.

Douglas, P.M., Pagani, M., Canuto, M.A., Brenner, M., Hodell, D.A., Eglinton, T.I., Curtis, J.H., 2015. Drought, agricultural adaptation, and sociopolitical collapse in the Maya Lowlands. Proceedings of the National Academy of Sciences 112, 5607-5612.

Fensterer, C., Scholz, D., Hoffmann, D.L., Spötl, C., Schröder-Ritzrau, A., Horn, C., Pajón, J.M., Mangini, A., 2013. Millennial-scale climate variability during the last 12.5ka recorded in a Caribbean speleothem. Earth and Planetary Science Letters 361, 143-151.

Gregory, B.R.B., Peros, M., Reinhardt, E.G., Donnelly, J.P., 2015. Middle-late Holocene Caribbean aridity inferred from foraminifera and elemental data in sediment cores from two Cuban lagoons. Palaeogeography, Palaeoclimatology, Palaeoecology 426, 229-241.

Hodell, D.A., Brenner, M., Curtis, J.H., 2005. Terminal Classic drought in the northern Maya lowlands inferred from multiple sediment cores in Lake Chichancanab (Mexico). Quaternary Science Reviews 24, 1413-1427.

Hodell, D.A., Curtis, J.H., Jones, G.A., Higuera-Gundy, A., Brenner, M., Binford, M.W., Dorsey, K.T., 1991. Reconstruction of Caribbean climate change over the past 10,500 years. Nature 352, 790.

Lane, C.S., Horn, S.P., Kerr, M.T., 2014. Beyond the Mayan lowlands: impacts of the terminal classic drought in the Caribbean Antilles. Quaternary Science Reviews 86, 89-98.

Li, L., Li, W., Kushnir, Y., 2012. Variation of the North Atlantic subtropical high western ridge and its implication to Southeastern US summer precipitation. Climate Dynamics 39, 1401-1412.

Tamalavage, A.E., van Hengstum, P.J., Louchouarn, P., Fall, P.L., Donnelly, J.P., Albury, N.A., Coats, S., Feakins, S.J., 2020. Plant wax evidence for precipitation and vegetation change from a coastal sinkhole lake in the Bahamas spanning the last 3000 years. Organic Geochemistry 150, 104120.

Taylor, Z.P., Lane, C.S., Horn, S.P., 2020. A 3600-year record of drought in southern Pacific Costa Rica. Quaternary Research, 1-13.

APPENDIX A

SUPPLEMENTARY FIGURES

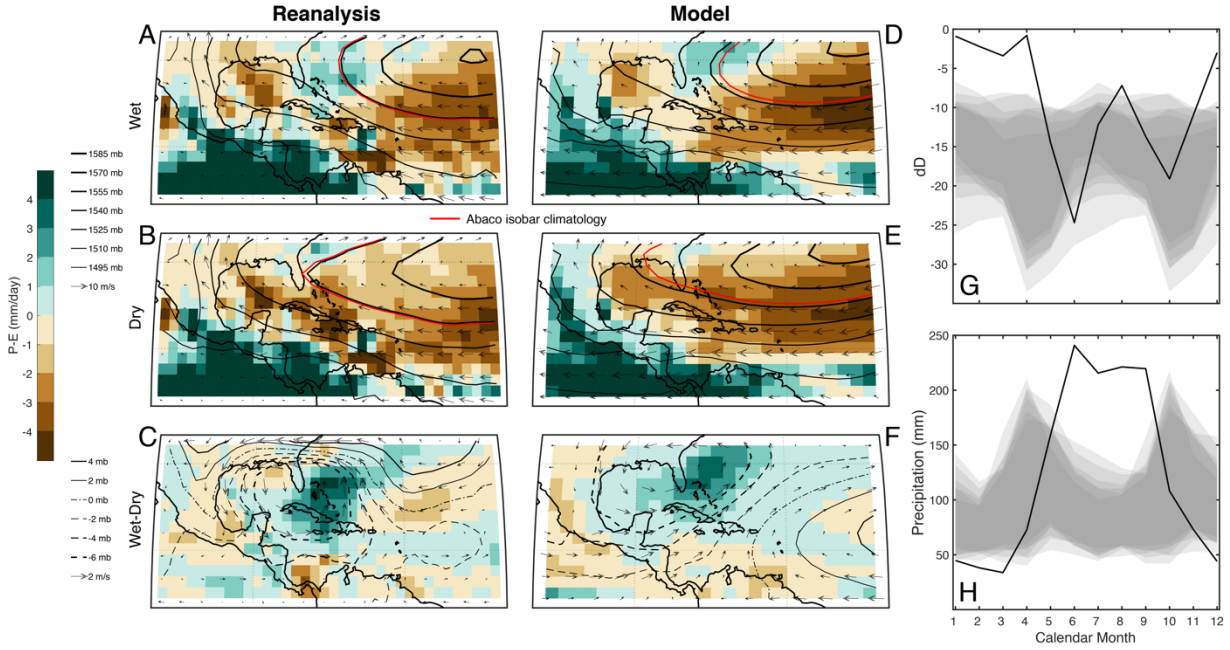

Figure 5:1: Additional Comparison of May-October precipitation minus evaporation.
(P-E, color), 850 mb wind (vectors), and 850 mb geopotential height (contours) highlighting the climatological isobar that sits over Abaco (red line) for the 2.5% (75 years total) wettest (a and d) and driest (b and e) years and the difference (c and f) at Abaco in the National Oceanic and Atmospheric Administration 20th Century Reanalysis (Compo et al. 2011) and the iCESM

simulations, respectively. The wettest and driest years were calculated for the average of all spatial grid points within 300km of Abaco (26.79°N, 282.58°E). g) and h) show the seasonal cycle of precipitation and δ^2H from the Havana, Cuba GNIP

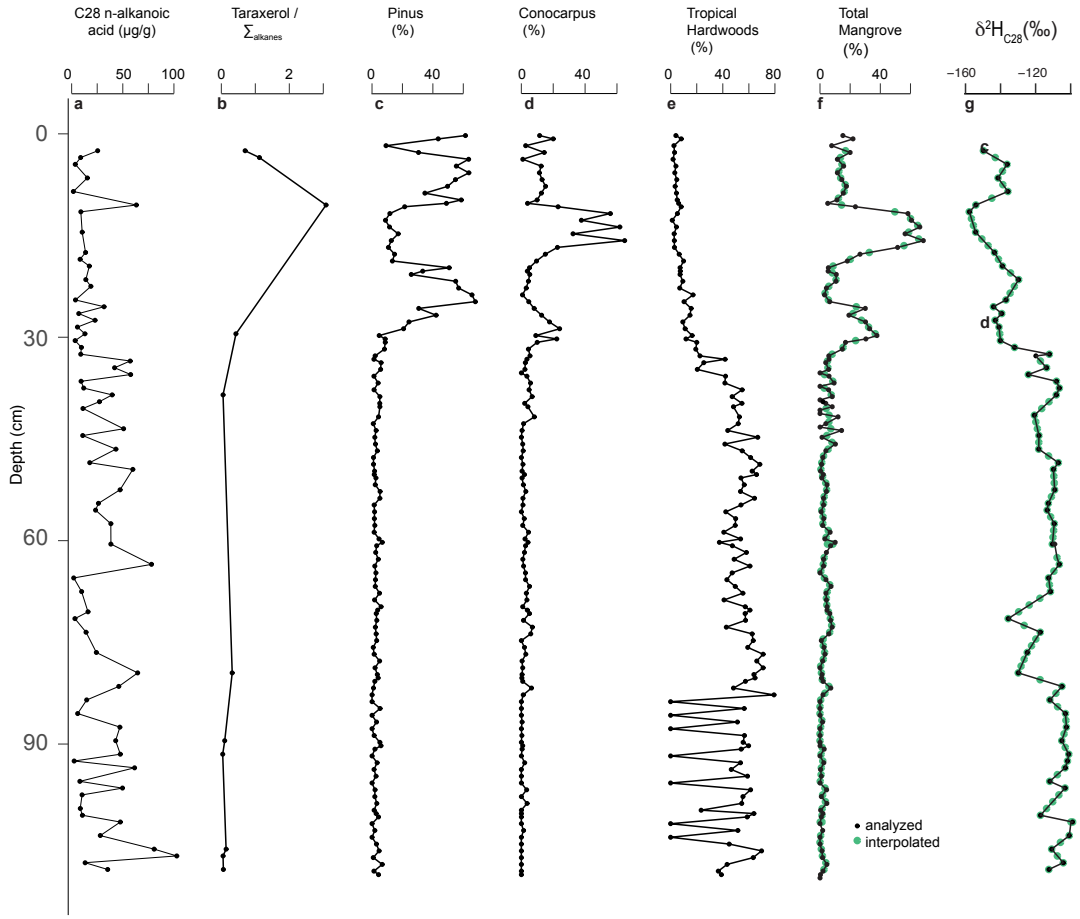

Figure 5:2: Downcore sampling design for biomarker and pollen data.

Data highlights C_{28} *n*-alkanoic acid abundance (a), and taraxerol/$\Sigma_{alkanes}$, key pollen species (c-f) including summed total mangrove pollen. Interpolated values for total pollen (%) and δ^2H_{28} used in defining the linear relationship between pollen (%) and δ^2H are colored in green (f-g).

Table 5:1: Conventional Radiocarbon dates for EMLD C1, C2, C4, and RP5.

Accession number	Core	Section	Core section depth (cm)	Total core depth (cm)	$F^{14}C$	Conventional ^{14}C age	Conventional Age Error
OS-152150	EMLD C1	1:3	10.5	10.5	0.9158 ± 0.0021	705	20
OS-152151	EMLD C1	1:3	49	49	0.7548 ± 0.0015	2260	15
OS-152152	EMLD C1	2:3	5.5	97.5	0.725 ± 0.0016	2580	15
OS-152153	EMLD C1	2:3	111.5	203.5	0.6455 ± 0.0017	3520	20
OS-152214	EMLD C1	3:3	101.25	317.75	0.5692 ± 0.0015	4530	20
OS-153819	EMLD C2	1:5	31.75	31.75	0.68 ± 0.0020	3100	25
OS-153820	EMLD C2	1:5	77	77	0.6445 ± 0.0018	3530	25
OS-153792	EMLD C2	2:5	69.25	192.25	0.5955 ± 0.0114	4160	150
OS-153821	EMLD C2	5:5	20.25	445.25	0.4388 ± 0.0019	6620	35
OS-153793	EMLD C2	5:5	119.75	544.75	0.406 ± 0.01	7240	200
OS-152215	EMLD C4	1:7	14.5	14.5	0.729 ± 0.0016	2540	20
OS-152216	EMLD C4	1:7	49.5	49.5	0.7014 ± 0.0018	2850	20
OS-137772	EMLD C4	2:7	2	125	0.6328 ± 0.0016	3680	20
OS-137773	EMLD C4	2:7	37.5	160.5	0.6259 ±0.0016	3760	20
OS-133773	EMLD C4	2:7	71.5	194.5	0.5948 ± 0.0019	4170	25
OS-133774	EMLD C4	3:7	59.5	276.5	0.5666 ± 0.0018	4560	25
OS-133775	EMLD C4	4:7	126.5	410.5	0.4908 ± 0.0018	5720	30
OS-133776	EMLD C4	5:7	117.5	542.5	0.4451 ± 0.0018	6500	35
OS-133772	EMLD C4	6:7	83.5	646	0.3491 ± 0.0017	8450	40
OS-137774	EMLD C4	7:7	2	653	0.4031 ± 0.0015	7300	30
OS-153822	EMLD C4	7:7	49.5	700.5	0.3984 ± 0.0018	7390	35
OS-133791	EMLD C4	7:7	64	715	0.3953 ± 0.002	7460	40
OS-155904	EMLD RP5	1:1	5	5	0.8658 ± 0.0018	1160	15

OS-148463	EMLD RP5	1:1	8.25	8.25	0.7429 ± 0.0016	2390	15
OS-148464	EMLD RP5	1:1	22.5	22.5	0.8231 ± 0.0016	1560	15
OS-148465	EMLD RP5	1:1	29.5	29.5	0.8156 ± 0.0017	1640	15
OS-148466	EMLD RP5	1:1	49.5	49.5	0.7981 ± 0.0016	1810	15
OS-148467	EMLD RP5	1:1	58.75	58.75	0.7898 ± 0.0017	1900	15
OS-155905	EMLD RP5	1:1	61.5	61.5	0.7782 ± 0.0016	2020	15
OS-155906	EMLD RP5	1:1	54.5	54.5	0.4243 ± 0.0014	6890	25